Probe based multimodal and multi frequency methods for material characterization at nanoscale

A DISSERTATION
SUBMITTED TO THE FACULTY OF THE GRADUATE SCHOOL
OF THE UNIVERSITY OF MINNESOTA
BY

Govind Saraswat

IN PARTIAL FULFILLMENT OF THE REQUIREMENTS
FOR THE DEGREE OF
Doctor of Philosophy

Prof. Murti V. Salapaka

February, 2014

Acknowledgements

During the early years of undergrad, I never imagined myself committing to academic research for six or more years. Things changed in the later part of my third year when I was involved in a research project with my close friend Pradeep Agarwal (Solah) and my future B.Tech advisor Prof Jagadesh Mamidala. Solah was brilliant and his ability to make me believe that I am actually capable of doing independent research gave me the inspiration to think about pursuing a PhD for the first time and I really thank him for that. I would also like to thank Prof Mamidala for advising me on my first research project and guiding me to my first journal paper.

My stay of more than six years working on PhD in the Nano Dynamics Systems Lab (NDSL) has changed me in many different ways. It has made me grow into a confident researcher who is not afraid to work and contribute towards unfamiliar technologies. I would like to thank my PhD advisor Prof Murti Salapaka for giving me the opportunity to work on many different projects and providing me with a wider outlook on research. He always knew how to push me in the right direction and get the best out of me. Knowing him on both personal and professional level, I am heavily inspired by his dedication, motivation, intelligence and above all his uprightness. I also have to thank his wife Durga and his kids Siddhartha and Pranav who were an integral part of all the lab treats and social gatherings. I will miss Durga's delicious food and the late night after party discussions at their house which typically went on till 2 AM!

I got the opportunity to collaborate with many professors at the U on various projects during my stay here. I would like to specifically mention Dr Greg Haugstad, who I worked with for the study of material properties using AFM. I thank him for giving many incisive insights into an instrument I used to think I know everything about. I would also like to thank Prof Mihailo Jovanovic and Prof Mo Li for being on my

committee, and also Prof Tryphon Georgiou for the many thought provoking courses he taught me.

During my stay in the NDSL lab, I got the chance to interact with a number of amazing people. My seniors Pranav, Hullas and Tanuj were like a family to me. I would forever be indebted to them for making my stay here extremely eventful, may it be those long runs/work outs with Hullas, late night discussions/experimental sessions with Pranav or bike trips all around the twin cities with Tanuj. Later, Subhrajit, Sayan and Shreyas became my colleagues in the NDSL lab and good friends. I have to especially thank Subhrajit for his plethora of advises on so many work as well as non-work related matters.

PhD is a long journey and apart from lab-mates, I met a number of amazing people. I would like to thank Rajat and Pushkar who were my first roommates. We discovered Minneapolis together and I had a wonderful time with them. I also lived with Manoj Paul, Abhijit, Aman and Ajay. I was lucky to get such splendid people as roommates and I had a terrific time with all of them. I made a lot of friends during these past six years who made life after work so much fun. I would like to thank Kalpesh, Saurabh, Anand, Apurva, Pulkit, Suma, Raghu, Aruna, Palak, Pavani, Jikku, Jyothy and many more with whom I have shared so many happy memories in these past six years.

I have to acknowledge my college friends Mili, Sahare and Bhanu who were always a phone call away to talk things through whenever I needed them. I would also like to thank Chakki for being there during the final years of my PhD which would have been so much more stressful if not for her. She is a constant source of support, love and care, an amazing cook and also proof reads all the articles I write!

Family was one constant I could always lean on during this long and arduous journey. My parents were always supportive, and made me believe in myself. I have always admired my sister Nirmal and her PhD in Psychology was a big inspiration for me to pursue a doctorate. I know that my brothers Rajendra and Nagendra are proud of me even though they always tease me about my inability to make inverters for them in spite of being an electrical engineer. I could not have done any of this without their support.

Dedication

To my parents, Pushpa and Bhuwanendra, and my sister Nirmal for their unwavering support and faith in me

Abstract

This thesis aims to provide a methodology and paradigm to aid emerging research studying and manipulating different mechanical properties (like topography, etc) of material. This material research is immensely enhanced by different probe based microscopy enabling design and discovery at the atomic scale. The Atomic Force Microscope (AFM) is one of the foremost technique for such interrogation of material. AFM is a micro-cantilever based device capable of achieving sub Angstrom resolution. Recently, probe researchers have shifted the focus to interrogate physical properties other than topography, namely stiffness and dissipation. Current AFM methods to determine these properties are not suitable for soft samples. Thus there is a scarcity of real-time techniques to quantify the mechanical properties of soft-matter, that include polymers and bio-matter.

A method is reported (REEP algorithm) which is able to provide estimates of sample stiffness and dissipation during intermittent contact mode operation of AFM. A systems approach is first applied to relate the material properties to the parameters of a time-varying linear system. Then a RLS algorithm is used to estimate these paramters. The method is verified using the averaging theory and shown to accurately provide the dissipation estimates when applied on different polymer samples. A FPGA based hardware implementing the REEP algorithm is developed to make use of the real-time capability of the algorithm. The REEP module is then used to study stiffness and dissipation properties of PBMA-PLMA polymer blend. A magnetic excitation hardware is also built to accurately resonate the cantilever in liquid. A clean ac response of the cantilever is thus achieved. REEP module is then used to delineate material properties of microtubules in buffer solution. It is shown that REEP module is able to accurately estimate the stiffness and dissipation properties of the bio-sample during under liquid operation of AFM.

Higher eigenmodes of cantilever dynamics often come into play when AFM is operated in liquid (low Q operation). To obtain better estimation of the contribution of these modes, a receding horizon Kalman Filter is reported. Estimates are shown to have an order of magnitude improvement compared to current methods. A high bandwidth

detection algorithm is also reported which is useful if just the presence of the higher modes is to be detected. Finally, a a new mode of imaging using the equivalent parameters of the time-varying system as a feedback is proposed. Simulation and experimental results show higher resolution for low Q operation.

This thesis separately explores a new hypothesis to understand directed transport in cells. Motor proteins which are the work-horse of intracellular transport, walk on microtubules (tubulin polymers) to transfer cellular cargo from one place to another inside a cell. Almost absolute directed transport is achieved while transport takes place over a random arrangement of microtubules. It is shown via simulation and analytical results that if the motors have an ability to switch between different microtubules, a little bias in the microtubule network can lead to directed transport. This renders useless any kind of recognition factor to be needed for motors to know which microtubule is target ended.

Contents

Acknowledgements i

Dedication iii

Abstract iv

List of Figures ix

1 Introduction 1

1.1 Materials and Methods 7

1.1.1 Numerical Simulation 7

1.1.2 Sample 7

1.1.3 Atomic Force Microscopy 8

1.2 Organization of the Thesis 9

2 Equivalent Cantilever Concept: Averaging Theory 11

2.1 Introduction 11

2.2 Theoretical Considerations 14

2.2.1 Arriving at the Equivalent Cantilever model 14

2.2.2 Deriving Sample Properties from Equivalent Cantilever Parameters 18

2.2.3 Formulation of Equivalent Cantilever parameters estimation as system identification 18

2.2.4 Multitone Excitation 19

2.3 Multimode Approximations 23

2.3.1 Challenges and Approach 23

2.3.2 Energy Dissipation in each mode 26
2.3.3 Tool to analyze Resonance Conditions: 27
2.3.4 Simulation results and Conclusion 28
2.4 Recursive Estimation of Equivalent Parameters 29
2.5 Off-line Experimental Results 31
2.5.1 Conclusion 33

3 Real-time Hardware Implementation of REEP Module 35
3.1 Digital Design Cycle 36
3.2 Individual Blocks 38
3.2.1 Building the Individual Modules 39
3.2.2 Top Level Integration 41
3.2.3 Experiments and Results 41
3.3 Conclusion 45

4 On contribution and detection of higher eigenmodes during dynamic Atomic Force Microscopy 47
4.1 Introduction 48
4.2 Multimode Observer 51
4.3 Faster Detection of higher modes 56

5 Real-time study of mechanical/physical properties of soft-matter in liquid environment under dynamic mode AFM 59
5.1 Introduction 59
5.2 Methods 60
5.3 Frequency Response 61
5.4 Parameter Estimation 63
5.5 REEP Imaging 65
5.6 Conclusion and Discussion 67

6 Topography Imaging Based on Equivalent Frequency Regulation 68
6.1 Introduction 68
6.2 Amplitude and f_e Sensitivities 69

6.3 Topography Imaging 72

7 Directed Transport of Motor Proteins over Random Networks of Microtubules 75

7.1 Introduction 75
7.2 Understanding the intracellular transport over biased random networks 76
7.3 Directed transport over a random network with bias achieved by regulation of switching tracks: an alternative hypothesis 78
7.4 Mathematical Formulation 79
7.4.1 Biased Random Walk 80
7.4.2 Simulation and Results 83
7.5 Transport in two dimension 85
7.5.1 Simulation Model 85

8 Summary and Discussion 88

References 90

List of Figures

1.1 Atomic Force Microscope (AFM): The main probe in an AFM is a micro-cantilever with a sharp tip that forms a force sensor. The deflection of the cantilever is registered by a laser incident on the cantilever that reflects onto a split photodiode. In most setups, a piezo scanner positions the sample relative to the sample in the lateral and the vertical direction. 2

1.2 Nonlinear Tip-Sample interaction force modeled as gradient of Lennard Jones potential. This has contributions from long range Van Der-Waals forces and short range chemical forces. Positive gradient implying attractive force has blue color where as negative gradient implying repulsive force had red color. 3

1.3 In the dynamic mode AFM, the cantilever is externally excited at the first resonant frequency of the cantilever flexure. The amplitude and phase at the forcing frequency (a and θ in the figure) are monitored to infer sample topography. A controller can be used to position the cantilever tip with respect to the sample in the z direction to regulate a setpoint amplitude a_0 in which case the control signal provides the image. 5

2.1 (a) Lennard Jones model for the non-linear tip-sample interaction showing tip trajectories for continuous contact (small deflections) and intermittent contact mode (large deflections). (b) Model of the cantilever-sample when deflections of cantilever are small and non-linear interaction can be linearized. (c) Model of cantilever-sample system with the piece-wise linear model of non-linear cantilever-sample interaction force. 12

2.2 Figure shows that using averaging theory, the cantilever being forced by $\tilde{g}(t)$ and the tip-sample separation dependent force $\tilde{\phi}$ with the tip deflection $p(t)$ can be viewed as an equivalent cantilever with changed resonant frequency f_e and quality factor Q_e being forced by $\tilde{g}(t)$ resulting in the deflection $p(t)$ (with no sample force $\tilde{\phi}$.) 15
2.3 Shows the amplitude of the first harmonic. In the approach phase (from time 0.04 to 0.05) the amplitude reduces from $21.5nm$ to $20.2nm$ and in the retract phase the amplitude recovers to 21.5nm. The amplitude as obtained by the averaged dynamics closely follows the original amplitude shown; the inset shows the error to be within $\pm 0.1nm$ 17
2.4 Simulation results for difference in steady state trajectories of actual simulation with monotone averaged equations and averaged equations with multitone excitation for a step input of $1nm$. Clearly multitone averaging is able to better approximate the trajectories 22
2.5 An Euler-Bernoulli beam 23
2.6 Simulation results for the two-mode approximation of the cantilever dynamics compared with the averaged equations. (a) shows the amplitudes of the resonant frequency of the first mode, and (b) shows the amplitudes of the resonant frequency of the second mode. 27
2.7 Schematic of REEP setup using a sum of three sinusoids as the drive signal to the cantilever. Two side frequencies are chosen such that the orbit of the cantilever deflection does not differ much from the tapping mode operation. 29
2.8 Modeling cantilever-sample interaction in tapping mode operation as a $G - \Phi$ interconnection where $G(i\omega)$ is the second order cantilever beam model and Φ is the nonlinear tip-sample force. $g(t)$, $z(t)$, ϑ and $p(t)$ are the dither forcing, the sample height profile, the measurement noise and measured cantilever deflection respectively. BCEWRLS algorithm takes $g(t)$ and $p(t)$ as input and provides the estimates of the equivalent resonant frequency, f_e, and quality factor, Q_e (which can be used to calculate k_e and c_e directly), of the cantilever in real time. 30

2.9 (Experimental Data; offline) (a) Comparison of power dissipated as determined by $\overline{\Phi}_D$ from REEP and via an analytical method described in [1] for two polymers PLMA and PBMA at two different locations for each polymer. It is known that PBMA is less dissipative than PLMA as confirmed with results shown. (b) the phase image (c) $\overline{\Phi}_c$ image (d) $\overline{\Phi}_d$ image of a SIBS block copolymer. The image size is $\approx 0.05\mu \times 1\mu$, stretched in y-axis by a factor of 2 to increase clarity. Note that high contrast that differentiates the domains of styrene (about $10nm$ in width) on isobutylene is high in the phase image. The contrast in $\overline{\Phi}_c$ image that characterizes the conservative (reactive) power is high; however, the contrast is minimal in the dissipative power characterized by $\overline{\Phi}_d$. Thus isobutylene and styrene have similar dissipative characteristics but different stiffness. . 32

3.1 Digital Design Cycle 36

3.2 Top Level Block Diagram of the architecture 38

3.3 Figure shows a) equivalent resonant frequency and b) equivalent Quality factor vs amplitude 'approach-retract' curve on PLMA polymer as calculated from Matlab (Off-line, green curve) and FPGA module (real-time, blue curve). Both curves match each other verifying the estimates determined by real-time module. 42

3.4 Figure compares the estimates of a) equivalent resonant frequency and b) equivalent quality factor obtained via the real-time module with the off-line estimates of MATLAB during a line scan of imaging a $20\mu m \times 20\mu m$ image of a PBMA-PLMA polymer blend. The small difference in the estimates is due to the analog noise present in the analog FPGA signal. 42

3.5 Figures (a) and (b) shows $20\mu m \times 20\mu m$ images of equivalent resonant frequency (f_e) and equivalent Quality factor (Q_e) of PBMA/PLMA polymer blend respectively. f_e, Q_e and amplitude image (shown in Figure 3.7 (b)) were used to determine $\overline{\Phi}_c$ (in N) and $\overline{\Phi}_D$ (in Joules). They are depicted in the figure (c) and (d) respectively. 43

3.6 Figure shows mean a) $-\overline{\Phi}_c$ and b) $\overline{\Phi}_D$ of PBMA and PLMA polymers. 1st data point is for PBMA domains and 2nd and 3rd data points are for intermediate size and large size PLMA domains respectively. It is clear that both types of PLMA domains have lower stiffness and higher dissipation as compared to the smaller PBMA domains 44

3.7 Figure shows a) Height (in nm) b) Amplitude (in nm) and c) Phase (in degrees) images of $20\mu m \times 20\mu m$ scan of PBMA/PLMA polymer blend respectively. These images were obtained simultaneously with the equivalent resonant frequency and equivalent quality factor images. . . 45

4.1 Simulation results showing cantilever 2^{nd}-mode power spectrum before and after interaction with a sample of height 30nm. Free-air curve is shifted right by 5kHz to highlight the difference in peaks. 51

4.2 Simulation results showing cantilever 2^{nd}-mode response for a step change in sample height. (a) Rms of error between Actual and estimated 2^{nd}-mode trajectories, by both amplitude-phase demodulation using lock-in amp (green) and RHK observer (blue). Sample height is changed from no-interaction (shown with negative value) to an interaction of 30nm at the time instant of 5s. The RHK observer is able to track the 2^{nd}-mode trajectory in less than 0.01ms after every tip-sample interaction, and thus has a tracking bandwidth of more than 100kHz. (b) 2^{nd}-mode amplitude demodulated from y_2 (without any measurement noise, blue), RHK observer estimate $\hat{y}_2$ (red) and y (combined cantilever deflection, green). Amplitude demodulated from RHK observer overlaps with the actual contribution. Rise time of actual amplitude is ≈ 0.12ms whereas the rise time of lock-in amplitude is ≈ 0.18ms. (c) Power spectrum for the noisy measurement of the 2^{nd}-mode contribution and its estimate. . 53

4.3 Experimental result for a 10 nm step change in sample height. (a) 2^{nd} mode trajectory estimated via Kalman observer compared with that evaluated by Lock-In amplifiers. (b) 2^{nd} mode amplitudes demodulated from trajectory estimated via Kalman observer (RHK) compared with that evaluated by demodulation of the cantilever deflection (Lock-in). Rise time of RHK amplitude is $\approx$ 0.05ms whereas the rise time of lock-in amplitude is $\approx$ 0.1ms which is of similar order to as observe in simulation. 55

4.4 Experimental result for higher mode detection. A square pulse of 20nm and 1kHz frequency was given to the sample height. (a) shows sample height overlaid on the 1st mode amplitude (blue) and the detected 'hits'. Green curve peaks are the local maxima of v_1 identifying the time of impact and also quantifying the effect of impact on the 1^{st}-mode. (b) shows the local maxima of v_2 with second mode amplitude overlaid. . . 57

5.1 Schematic showing the solenoid and the operational amplifiers. HV opamp amplifier has a gain of 10, where as the first amplifier is a summer circuit with appropriate gains. 60

5.2 (a) shows a diagram of solenoid plate with the sample and cantilever on top of it. As magnetic field is inversely proportional to the square of the distance between cantilever and solenoid, solenoid is placed directly below to maximize the magnetic force. (b) is an actual image of the developed hardware. Left is the power opamp with proper heat sinking and left is the upside down sample plate with the solenoid in the middle. . . 62

5.3 (a) plots the normalized amplitude for both magnetic and acoustic excitation compared with the normalized SHO fit to the thermal response of the cantilever in air. (c) plots the same for the case of in water operation. These are all off-sample. (b) and (d) plots the phase for two excitations (acoustic and magnetic) in both cases, in air and in water operations. 63

5.4 Figure shows the (a) equivalent resonant frequency and (b) equivalent quality factor during an approach retract cycle of dynamic AFM on a Mica sample in air. (c) plots the energy dissipated calculated using both REEP and the analytical means. For both approach and retract, REEP estimates are able to accurately measure the energy dissipated. 64

5.5 Figure shows the (a) equivalent resonant frequency and (b) equivalent quality factor during an approach retract cycle on a MT sample in buffer solution. (c) plots the energy dissipated calculated using both REEP and the analytical means. Even under liquid operation, REEP estimates are able to accurately measure the energy dissipated. 65

5.6 Results of a $3\mu m \times 3\mu m$ scan of the MT sample (a) plots the equivalent resonant frequency in Hz and (b) plots the equivalent quality factor. (c) plots the stiffness ($-\phi_c$) estimate of the sample while (d) plots the energy dissipated by the tip-sample interaction. 66

6.1 Sensitivity of steady state amplitude, equivalent resonant frequency and equivalent damping with respect to Z-Piezo position (sample height) during simulated approach-retract curves. Amplitude sensitivity is one irrespective of the cantilever's quality factor. Sensitivity of equivalent resonant frequency and damping increases with reducing quality factor. . . . 70

6.2 Sensitivity of steady state amplitude, equivalent resonant frequency and equivalent damping with respect to Z-Piezo position (sample height) during experimental force curves. Amplitude sensitivity is one irrespective of the cantilever's quality factor. Sensitivity of equivalent resonant frequency and damping increases with reducing quality factor similar to simulated trends. 71

6.3 Figure shows simulations results of amplitude and equivalent resonant frequency SNR when cantilever encounters a step size of $1nm$ while free air amplitude is $50nm$ 72

6.4 (simulation results) Shows that equivalent frequency (as estimated by the REEP algorithm) regulated based image a 1 nm variations in topography under high damping conditions is considerably better than the one obtained by regulating amplitude. 73

7.1 Schematic showing dynein and kinesin motor proteins attached to a cargo walking on microtubule. 76

7.2 (A) Microtubule distribution at the ring canals leading into the oocyte. Near the ring canals (arrow), the number and organization of microtubules increases. Bar, 5 μm. (B) Microtubule distribution within the oocyte as revealed with UAS-α-tubulin-GFP. Note the meshwork appearance of the microtubule array indicating a random nature. A higher concentration of microtubules is present at the anterior cortex, compared with the posterior cortex. Bar, 10 μ m. 77

7.3 (a) Statistic of motors reaching target end is plotted with the switching probability on a semilog scale for both Monte Carlo simulations and analytical expression. Standard deviation is shown as the bars in the Monte Carlo curve, both curves overlap. Here bias in the MT network is 0.6 towards the target end. Clearly phase change like behavior is visible at around $\alpha = 0.4$ with the change in slope. (b) Statistic for different values of bias is plotted. Higher bias leads to directed transport even for low values of α. 83

7.4 (a) Probability of switching (α) required to achieve at least 95% transport is plotted with the bias in the MT network. As bias increases, α required decreases drastically. (b) Average time required to reach the target end is plotted with the probability of switching for different values of the bias (p). Curves are from Monte Carlo simulation and the x marks are from the analytical expression. Clearly as α increases, mean time increases thus a trade-off exist between fast transport and directed transport. . . 84

7.5 One instance of network with 40 microtubules, 20 linear and 20 quadratic with $L = R = 100$. Here the blue and red thick outline on the left and right half plane donates the boundaries of the non-target and target end respectively. Intersections are marked with $\times$. 85

7.6 Results of Monte Carlo simulation for two-dimensional transport over microtubules are plotted here. Number of MTs is on the x-axis, and mean percentage of the motors reaching the target end is on the y-axis. Bars are standard deviation across different instance of network for same no. of MTs. Its a semilog plot and the change of slope clearly shows phase-change kind of behavior (at around 500 MTs). Also as the no. of MTs in increasing, standard deviation is decreasing drastically. 86

Chapter 1

Introduction

Emergent functionality and novel properties of material can result from the physical proximity and geometric arrangement of atoms/molecules enabled by control of matter at the atomic scale. Current needs of emerging fields, such as massive data storage and energy storage, include light weight and flexible materials with durability and stiffness that can be met with the design of material at the nanoscale. Such efforts of materials design and discovery at the atomic scale have to be accompanied by interrogation methods which have high spatial and temporal resolution to determine material properties at the nanoscale.

An important means of interrogating material at the nanoscale is based on the principles of Atomic Force Microscopy. Ever since the invention of the probe based method of atomic force microscopes (AFMs) by Binnig et. al. in 1986 [2], cantilever beams with a sharp tip at one end have been used to interrogate various material properties such as topography, mechanical, electrical, thermal and optical.

The main idea of atomic force microscopy is to use a micro-cantilever with a sharp tip at its one end similar to the operation of a gramophone stylus. The tip interacts with the sample and is raster scanned over a sample.Tip-sample interaction causes deflection in the cantilever which is recorded through an optical beam-bounce method and serves as a measure of sample topography (see Figure 1.1). In the beam-bounce method, a laser beam is focused at the back of the cantilever tip, which reflects it into a split photodiode. The ratio of the intensity of light in the two halves indicates the motion of the cantilever tip. A typical cantilever is $100 - 200\mu m$ long, $5 - 10\mu m$ wide and the

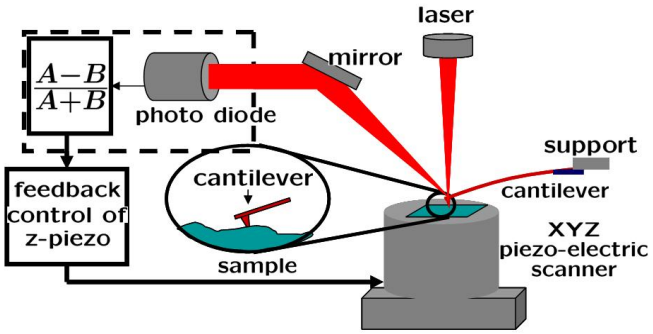

Figure 1.1: Atomic Force Microscope (AFM): The main probe in an AFM is a micro-cantilever with a sharp tip that forms a force sensor. The deflection of the cantilever is registered by a laser incident on the cantilever that reflects onto a split photodiode. In most setups, a piezo scanner positions the sample relative to the sample in the lateral and the vertical direction.

diameter of the tip is around $5nm$. Most of the cantilever are fabricated from silicon, silicon oxide or silicon nitride. The typical vertical resolution of the detection hardware is of the order of $1A^o$.

The cantilever can be modeled as a spring with a spring constant k. Thus $F = kp$, where F is the spring force on the cantilever, k is the spring constant and p is the measured cantilever deflection. This relation is used to infer the force from the measured deflection. This equation also indicates that for achieving large deflection for small interaction force, one would require softer cantilevers. A controller is used to regulate the cantilever deflection by moving the sample up and down thus maintaining constant force on the sample (see Figure 1.1). A piezoelectric transducer is used for positioning the sample stage. This mode of operation of AFM is called contact mode operation.

The tip-sample interaction forces can be modeled as the gradient of Lennard Jones interaction potential where the long range Van Der-Waals forces act in addition to the short range chemical forces to result in a interaction potential as shown in Figure 1.2. In the contact mode operation, the tip traverses a very small part of this non-linear interaction force thus we are able to make linear approximations. These approximations make the analysis of contact mode easier but there are some drawbacks of contact mode operation. This mode is harsh on both the tip and the sample because of high lateral and frictional forces and leads to faster wear and tear of both tip and sample. This

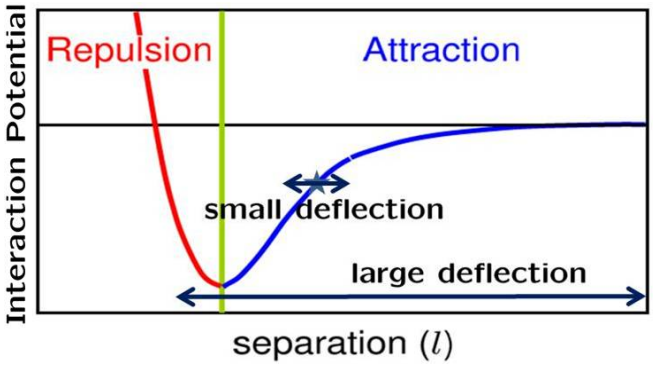

Figure 1.2: Nonlinear Tip-Sample interaction force modeled as gradient of Lennard Jones potential. This has contributions from long range Van Der-Waals forces and short range chemical forces. Positive gradient implying attractive force has blue color where as negative gradient implying repulsive force had red color.

mode also suffers from low signal to noise ratio since the sample information is located near the DC in the spectrum which is effected by the 1/f measurement noise.

The other mode of operation of AFM is called dynamic mode imaging, first proposed in 1987 [3]. In this mode, a piezoelectric transducer is used to excite the cantilever at or near its resonant frequency. Here, cantilever can be modeled as a fixed-free beam whose solution is given by a superposition of infinite modes [4]. Each mode is a second order spring-mass-damper system. Typically, a first mode approximation of the cantilever beam suffices to predict the deflection trajectories. Dynamic mode is further divided into two different modes, namely non-contact mode and intermittent contact mode. In non-contact (NC) mode, the cantilever is oscillated with a very small amplitude (typically less that $5nm$) close to the sample, in the attractive regime (see Figure 1.2) of the tip-sample interaction. Here, the dynamics of the cantilever-sample system is given by,

$$m\ddot{p} + c\dot{p} + kp \quad = \quad g(t) + \phi(p, \dot{p}) \tag{1.1}$$

where $p(t)$ is the instantaneous cantilever position, m is the mass, k is the spring constant and c is the damping coefficient of the first modal approximation of cantilever; $g(t)$ is the external sinusoidal excitation and $\phi(p, \dot{p})$ is the force due to nonlinear tip-sample interaction. Also the quality factor (Q) of the cantilever is defined as $Q = \frac{\sqrt{km}}{c}$.

In the NC mode, the amplitude of cantilever oscillation is small, so we can linearize $\phi(p, \dot{p})$ about a nominal operating point. Let the cantilever deflection be $p = \bar{p} + \tilde{p}$ where $\bar{p}$ is some nominal position and $\tilde{p}$ is the deflection around that nominal position. Then $\dot{p} = \dot{\tilde{p}}$ and the force $\phi(p, \dot{p})$ can be approximated by,

$$\phi(p, \dot{p}) = \phi(\bar{p}, 0) + \left.\frac{\partial \phi(p, \dot{p})}{\partial p}\right|_{\bar{p}} \tilde{p} + \left.\frac{\partial \phi(p, \dot{p})}{\partial \dot{p}}\right|_{0} \dot{\tilde{p}}. \tag{1.2}$$

Then the dynamics of the cantilever around the nominal position is given by,

$$m\ddot{\tilde{p}} + c_e\dot{\tilde{p}} + k_e\tilde{p} = g(t) \tag{1.3}$$

where $k_e = k - \left.\frac{\partial \phi(p,\dot{p})}{\partial p}\right|_{\bar{p}}$ and $c_e = c - \left.\frac{\partial \phi(p,\dot{p})}{\partial \dot{p}}\right|_{0}$. Thus the equivalent stiffness (k_e) and equivalent damping (c_e) of the cantilever change due to interaction with the sample. The sample stiffness k_s and damping c_s are define as $k_s = -\left.\frac{\partial \phi(p,\dot{p})}{\partial p}\right|_{\bar{p}}$ and $c_s = -\left.\frac{\partial \phi(p,\dot{p})}{\partial \dot{p}}\right|_{0}$.

Since $\left.\frac{\partial \phi(p,\dot{p})}{\partial p}\right|_{\bar{p}} > 0$ for an attractive force (see Figure 1.2), $k_e < k$, so the equivalent stiffness decreases. Similarly as $\left.\frac{\partial \phi(p,\dot{p})}{\partial p}\right|_{\bar{p}} < 0$ for a repulsive force, $k_e > k$, so the equivalent stiffness increases. Also since $\omega^2 = \frac{k}{m}$ for a spring-mass damper system, the equivalent resonant frequency ($\omega_e^2 = \frac{k_e}{m}$) of the first mode of the cantilever will increase for a repulsive force and decrease for an attractive force. Here, it can be seen that the change in stiffness is caused due to the conservative part of the force whereas change in damping is caused due to the dissipative part of the interaction force.

In this mode, instead of regulating the deflection of the cantilever, the instantaneous resonant frequency (ω_e) of the cantilever is regulated across a setpoint. This mode is also called Frequency Modulation AFM (FM-AFM) as the frequency is modulated. As the change in equivalent resonant frequency flips sign depending on the integrated interaction gradient (attractive or repulsive, integrated over the tip-sample interaction surface), feedback can only work if the deflection of the cantilever is restricted to one part of the interaction curve (Figure 1.2), namely attraction regime (as it extends to the infinite separation). To stabilize the tip in the attractive regime, cantilever with high stiffness are used to overcome the attraction. Also, the operation is sometimes performed in very low temperatures (few Kelvins) to reduce the thermal noise. In this mode, the information is around the resonance of the first mode of the cantilever and is away from DC, thus leading to a better SNR compared to contact mode. Here,

$1/f$ measurement noise is negligible and the operation is thermal noise limited. The minimum shift detectable in the resonant frequency decreases as the quality factor of the cantilever increases. Thus for achieving phenomenal resolution of $1A^o$, very high Q (typically 10000-15000) of cantilever is required. Also the environment and the temperature needs to be controlled precisely to stabilize the tip in the attractive regime of the tip-sample force. That is why, this mode is predominantly used in low temperature and ultra high vacuum conditions. Thermal vibrations are reduced in low temperature thus increasing the stability as well as the SNR. Also the quality factor of the cantilever is further increased in ultra high vacuum conditions. FM-AFM mode, though capable of true atomic resolution is not easily stabilizable for under-fluid operations. Since there is a large spectrum of samples that require to be imaged in their native conditions viz. biological species in their native buffers, this mode is rendered useless for such applications. Here, FM-AFM is mostly limited to force-spectroscopy apart from recent imaging results by Sader and Jarvis [5].

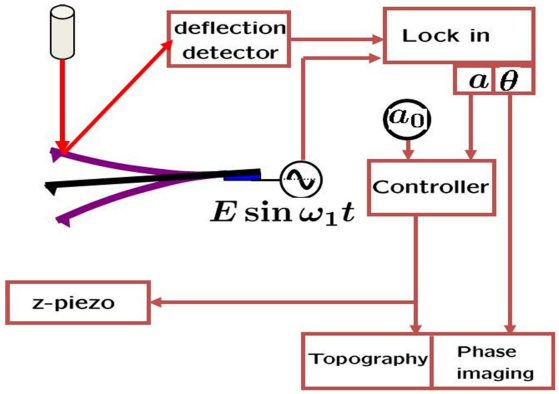

Figure 1.3: In the dynamic mode AFM, the cantilever is externally excited at the first resonant frequency of the cantilever flexure. The amplitude and phase at the forcing frequency (a and θ in the figure) are monitored to infer sample topography. A controller can be used to position the cantilever tip with respect to the sample in the z direction to regulate a setpoint amplitude a_0 in which case the control signal provides the image.

The intermittent contact mode (also known as Tapping Mode) is a prevalent means of investigating properties of soft-matter. In the intermittent contact mode operation of AFM, the cantilever is oscillated with large amplitudes by a sinusoidal dither forcing at the base of the cantilever. Typical operational amplitudes can vary from few nm to

100 nm.Here the cantilever-tip interacts with the sample intermittently every oscillation cycle thus exerting extremely low lateral and frictional forces on the sample. The intermittent contact mode is gentler and less invasive but it poses new challenges. Fig 1.2, highlights how interaction forces felt by the cantilever differ in the intermittent and non contact modes. In this mode, linearization of tip-sample interaction is not applicable as the tip traverses the entire non-linear interaction curve (Fig 1.2). Nevertheless, the notion of *net* attractive and *net* repulsive interaction force can be introduced. It can thus be argued that net affect of the interaction force can either decrease (*net* attractive) or increase (*net* repulsive) the equivalent stiffness of the cantilever-sample system depending on the relative strength of attractive and repulsive forces [6]. Here, as the sample is raster-scanned in relation to the oscillatory cantilever, the amplitude and the phase of the first harmonic component (of the forcing frequency) of the cantilever trajectory are used to probe properties of the sample (see Figure 1.3) including the topography. In existing studies, the phase of the first harmonic component of cantilever oscillation with respect to the dither forcing is heavily relied upon to gauge material properties particularly the dissipation properties of the material. However, it is known that the phase can lead to ambiguous interpretations of the dissipation properties of material [7, 8]. Thus during the intermittent contact mode operation, there is a need for developing observable quantities that are a direct measure of sample properties. In this thesis, we report a method for simultaneously determining the topography, stiffness and dissipative properties of materials at the nanoscale in a probe based dynamic mode operation. The method provides recursive estimates of equivalent parameters (REEP) which are shown to relate to the stiffness and dissipation properties of the material. The method is particularly suited for investigating soft matter such as polymers and bio-matter. We use perturbation analysis tools for mapping dissipative and stiffness properties of material, into parameters of an equivalent linear-time-invariant model. It is also shown that this model can be extended to the case when multiple modes of the cantilever participate in the nonlinear interaction with the sample forces. Parameters of the equivalent model are adaptively estimated, where, for robust estimation a multi frequency excitation of the probe is introduced. We demonstrate that the reported method of simultaneously determining multiple material properties can be implemented in real-time on existing probe based instruments. We further demonstrate the effectiveness of the method by

investigating properties of a polymer blend.

The intermittent mode of AFM operation is very well suited to image biological samples in there native buffer. To achieve a clean resonance of cantilever in liquid, a solenoid based magnetic excitation hardware is developed. We have applied REEP method to image the mechanical properties of bio samples in liquid. This is the first time that a real-time study of material properties in liquid is reported.

Most of the analysis of the dynamic mode operation is based on the single-mode approximation of the cantilever beam. However, recently, newer modalities of operation are employing higher modes of the cantilever flexure beam [9] and are also using novel means of excitation [10, 11]. Moreover a number of soft-matter investigations are conducted in a fluid environment where the quality factors of various modes of cantilever's deflection are significantly lower. The lowered quality factors can enhance [12] the participation of the higher modes in forming the cantilever deflection. In this thesis, a comprehensive framework based on a modified Kalman Filter, to extract the contribution of different modes is also developed. It is shown that it can be implemented to provide the estimates of these contribution in real-time. A paradigm to further provide a high-bandwidth method to detect only the presence of higher modes is also studied.

1.1 Materials and Methods

1.1.1 Numerical Simulation

All equations and models were simulated using custom codes in MATLAB. Standard ordinary differential equation (ODE) solvers of MATLAB were used. All the off-line data was captured through National Instrument's (NI) data acquisition card using LabView.

1.1.2 Sample

Two polymer systems were primarily used; a blend of poly(butyl methacrylate) and poly(lauryl methacrylate) (PBMA-PLMA) and a triblock copolymer of poly(styrene-block-isobutylene-block-styrene) (PS-PIB-PS or SIBS). For PBMA-PLMA case, the solution was 15mg/mL of total polymers in tetrahydrofuran. The relative polymer concentration was 75-25 for PBMA-PLMA. The polymer was spin-coated onto a silicon

wafer from the solution, under ambient conditions, to produce a film thickness of $\approx 1\mu m$, followed by ambient drying. The relative polymer concentration for SIBS was 17:83 for PS:PIB with Mw=103,000. The polymer was again spun under ambient condition onto silicon wafer from 20% toluene solution, to produce a film thickness of $\approx 1\mu m$, and dried in vacuum at 110°C for 2 hours. The SIBS film was additionally annealed overnight in the solvent vapor (small beaker of solvent under inverted larger beaker) to produce more pronounced phase segregation into cylindrical PS domains that lie predominantly parallel or perpendicular to the surface.

Microtubule sample for all the bio experiments is provided by Dr Melissa's lab (MCB department).

1.1.3 Atomic Force Microscopy

All experiments were performed on commercially available AFM, MFP-3D from Asylum Research. Two Olympus cantilevers, AC240 (typical spring constant of 2 N/m and resonant frequency of 70kHZ) and AC160 (typical spring constant of 42 N/m and resonant frequency of 300kHZ) were used. Both cantilevers were rectangular shaped, had silicon tetrahedral tip with typical radius of $7nm$ and aluminum coating on the reflex side. For imaging, a close loop x-y nano-positioning system was used to raster scan the sample. A z-piezo was used to position the cantilever tip vertically with respect to the sample to regulate a set-point amplitude. Same z-piezo was also used to generate 'approach-retract cycle' [6] curves where cantilever was first moved closer to sample in the approach phase and then away from sample in the retract phase.

Magnetic cantilevers from Agilent are used for magnetic excitation experiments. MAC lever Type I and Type II (typical spring constant of 2.8 N/m and resonant frequency of 75kHZ) are used specifically. Type I chip had three levers with typical spring constants of 0.95 N/m, 1.75 N/m and 0.6 N/m and typical resonant frequencies of 110kHz, 90kHz and 130kHz respectively.

An outline of the thesis is provided next.

1.2 Organization of the Thesis

This thesis used various systems concepts to develop a paradigm for interrogation of different material properties. A separate work on explaining Intracellular transport on Microtubules is also presented.

- Chapter 2 introduces the concept of equivalent cantilever model in dynamic mode operation. A recursive least square algorithm is verified which is able to estimate the parameters of this equivalent cantilever model by exciting the cantilever with a sum of three sinusoids. Averaging theory is then used to rigorously establish the equivalent cantilever concept for this richer excitation of cantilever. An approach to obtain the equivalent cantilever model for higher eigenmodes is also presented. Approach-retract curves on a polymer sample were performed and stiffness and dissipation properties were obtained.

- Chapter 3 presents a real-time implementation for the above mentioned algorithm using a FPGA based hardware. Developed hardware is used to obtain real-time images of stiffness and dissipation properties of a polymer blend during the intermittent contact mode operation of the AFM.

- Chapter 4 introduces a new framework to quantify the contribution of different flexure modes of the cantilever in dynamic mode operation of the AFM using a receding horizon Kalman filter. Simulation and experimental results are presented that support an order of improvement over current techniques. Further, a detection method is also developed to provide high-bandwidth detection of higher modes in the case when only presence of higher mode is to be detected.

- In Chapter 5, REEP algorithm is extended to the under fluid operation of dynamic mode AFM. A magnetic actuation hardware is developed to obtain clean resonance of cantilever under liquid. The developed hardware is then used to quantify the mechanical properties of microtubules in their native buffer.

- Chapter 6 introduces a new mode of topography imaging based on equivalent frequency regulation. It is shown that for low quality factor operations (like in fluid), equivalent frequency is much more sensitive to changes in topography then the

amplitude. Simulations using feedback based on maintaining a setpoint equivalent resonant frequency shows the higher sensitivity of the mode.

- In Chapter 7, a separate work on studying the directed transport of Motor Proteins over random networks on Microtubules is presented. Analytical and Monte Carlo simulation results are obtained for a 1D model of transport with a little bias in the directionality of the tracks. Results suggest that almost 100% directed transport is achieved if the motor has the ability to switch tracks over the intersections. Monte Carlo simulations for a 2D model further corroborates the hypothesis.

- Chapter 8 summarizes the work accomplished during the course of the thesis.

Chapter 2

Equivalent Cantilever Concept: Averaging Theory

2.1 Introduction

A recent focus of probe researchers has been the quantitative imaging of material properties, particularly of properties other than topography, such as the stiffness and dissipation attributes at the nanoscale. This focus has the potential to substantially further the impact of probe based methods on science and technology. Of particular importance is the design and interrogation of soft-matter, that include polymers and bio-matter, which are increasingly being used in novel applications such as drug delivery, flexible electronics and as energy harvesting and storage material.

Current AFM methods [13, 14] to determine material properties are predominantly *continuous contact* methods, where the cantilever is continuously interacting with the sample. In the continuous contact mode, the deflection remains small and the net tip-sample interaction is either attractive or repulsive (see Fig 2.1(a)). Under the assumption of small cantilever deflection, the sample behavior can be linearized. Here, the combined cantilever-sample system can be visualized as an equivalent spring-mass-damper (*equivalent cantilever*) with an equivalent stiffness and equivalent damping (see Fig 2.1(b) and Equation 1.3). There is an open question on the simplest excitation of the cantilever that can lead to a real time estimation of the equivalent cantilever parameters.

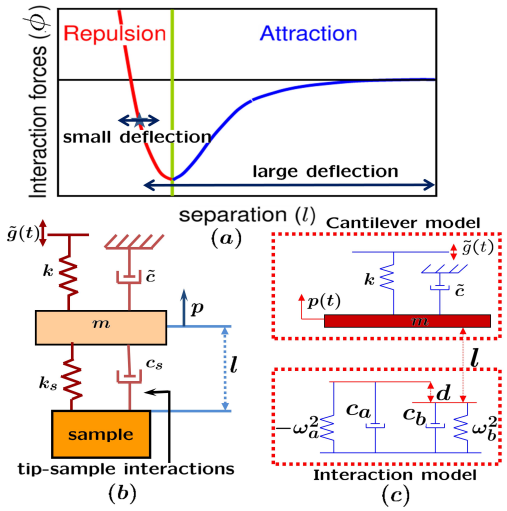

Figure 2.1: (a) Lennard Jones model for the non-linear tip-sample interaction showing tip trajectories for continuous contact (small deflections) and intermittent contact mode (large deflections). (b) Model of the cantilever-sample when deflections of cantilever are small and non-linear interaction can be linearized. (c) Model of cantilever-sample system with the piece-wise linear model of non-linear cantilever-sample interaction force.

Recently, a continuous contact method called Band Excitation (BE) was reported to determine material properties at the nanoscale. The BE method has found widespread application [15, 16]. Here, the cantilever is excited with a continuous band of frequencies near resonance, while keeping the cantilever deflection small. A second order model is fit to the measured response which provides the parameters of the equivalent cantilever that represent the cantilever-sample system. The spatial resolution is dictated by the size and the distance between the pixels while the temporal resolution is limited by the large time spent at each pixel. In this method, the cantilever response to the input excitation has large amplitude variation which makes it difficult to obtain equivalent cantilever model parameters at one particular interaction level which can be required to characterize the parameters with respect to the extent of interaction. Another recent continuous contact method [14] which offers substantial improvement in terms of bandwidth over BE uses dual AC tracking (DART [17]) to estimate the equivalent parameters in the contact resonance mode of AFM. In this method, tip-sample contact is excited simultaneously at two frequencies on either side of the contact resonance (resonance in the case of small amplitude cantilever oscillation). These methods being contact mode

are relatively harsh on sample and are not ideally suited for soft-matter investigation. To date there are no methods which provide real-time simultaneous estimates of dissipation and stiffness of material and are amenable to the *intermittent contact* (dynamic) mode operation of AFM [11].

Among various methods of material property interrogation using probe based techniques, there is a paucity of high bandwidth methods for soft-matter investigation. In this chapter, we report a method that simultaneously obtains estimates of stiffness of the material and the energy lost to the sample in the *intermittent contact* mode operation of AFM, which is among the least invasive mode of probe based interrogation. The temporal resolution of the method is better than that of typical imaging speeds of dynamic mode AFM and therefore, the estimates of the sample properties can be considered real-time.

Systems based principles have resulted in unparalleled results for the advancements in Atomic Force Microscopy [18, 19, 20, 21]. In this chapter, these principles are used to develop a method for determining dissipation losses to the sample and stiffness of the material. This chapter builds on the recent work (see [10]), where a method called recursive estimation of equivalent parameters (REEP) was reported. In [10], the cantilever with a single sinusoid excitation (with large amplitude oscillation in the range 24-200nm) under the nonlinear interaction with the sample is modeled as an equivalent cantilever (see [22, 23]). However, the equivalent cantilever parameters are estimated using a multi-tone excitation employing a recursive least square method. The sensitivity of the equivalent parameters to topography was the main focus of that study. Here we demonstrate that the equivalent parameter model under a multi-tone excitation remains valid. Toward this goal, we extend existing knowhow on averaging theory for periodically forced cantilever, in a dynamic mode AFM operation, to a multi-tone excitation where the forcing is no longer periodic and thus periodic averaging theory is no longer applicable. Furthermore, we demonstrate that the estimates of the sample stiffness and dissipation can be obtained in real-time. A framework to extend the equivalent cantilever model for higher modes of the cantilever is also presented.

Before proceeding further, we note that the dissipation determined using above methods, including the one to be presented here, can not be taken as a direct measure of the intensive dissipation property of the material. Even if the viscoelastic dissipation

properties (rate-dependent mechanical response) do not differ much between two samples, non-mechanical differences like, molecular freedom at the surface and Hamaker constant of tip-sample interaction (which relates to the mutual polarizability of pairs of interacting atoms), can affect the total dissipation, which also contribute to adhesion hysteresis [6]. Thus probe based methods determine *total* dissipation occurring due to overall tip-sample interaction, having both internal and interfacial sources of dissipation.

2.2 Theoretical Considerations

2.2.1 Arriving at the Equivalent Cantilever model

A first mode approximation of the cantilever dynamics results in a spring-mass-damper model of the cantilever where the sample forces are felt by the mass. For small deflection of the mass, the sample's influence can be modeled as a spring (with stiffness k_s) and a damper (with damping c_s), where the stiffness of the spring is given by the local slope of the curve that relates the interaction force and the cantilever-sample separation (see Figure 2.1(b)). Here the cantilever-sample system can be envisioned to be an equivalent cantilever (another spring-mass-damper system) with changed parameters, such as stiffness changing from k to $k+k_s$ (see Equation 1.3).

In the case where the cantilever oscillations are large, the cantilever tip explores a considerable portion of the tip-sample non-linearity that does not allow for a linearized approximation of the tip-sample interaction. However, under sinusoidal forcing it is still possible to arrive at an equivalent cantilever model of the combined cantilever-sample system by appealing to averaging theory (see Figure 2.2 and [7]). Here, the second order dynamics of the cantilever-sample system is given by

$$m\ddot{p} + \tilde{c}\dot{p} + kp = \tilde{\phi}(p, \dot{p}) + m\tilde{g}(t) \tag{2.1}$$

where $p(t)$ is the instantaneous cantilever position, m is the mass, k is the spring constant and $\tilde{c}$ is the damping coefficient of the first modal approximation of cantilever; $\tilde{g}(t)$ is the dither excitation and $\tilde{\phi}(p, \dot{p})$ is the force due to nonlinear tip-sample interaction. Let $\omega^2 := k/m$ be the resonant frequency. Assuming that the damping $\tilde{c}$, forcing $\tilde{g}$, and the tip-sample interaction $\tilde{\phi}$ are small we define $\tilde{c} = \epsilon c$, $\tilde{g} = \epsilon g$, and $\tilde{\phi} = \epsilon\phi$, where, ϵ is

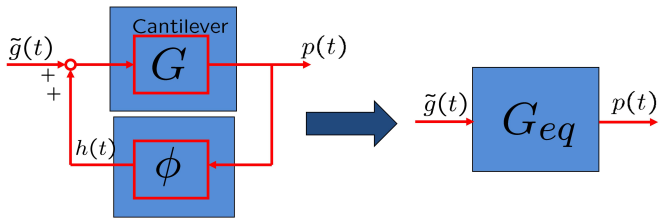

Figure 2.2: Figure shows that using averaging theory, the cantilever being forced by $\tilde{g}(t)$ and the tip-sample separation dependent force $\tilde{\phi}$ with the tip deflection $p(t)$ can be viewed as an equivalent cantilever with changed resonant frequency f_e and quality factor Q_e being forced by $\tilde{g}(t)$ resulting in the deflection $p(t)$ (with no sample force $\tilde{\phi}$.)

a small parameter. It follows from Eq.2.1 that

$$\ddot{p} + \omega^2 p = (\epsilon/m)\phi(p, \dot{p}) + (\epsilon/m)g(t) - (\epsilon/m)c\dot{p} \tag{2.2}$$

Defining a change of coordinates from $(p, \dot{p}) \to (a, \theta)$ via

$$p = a\cos(\omega t + \theta);\ \ \dot{p} = -a\omega\sin(\omega t + \theta), \tag{2.3}$$

and differentiating the relations in Eq.2.3 with respect to time, the dynamics in the changed coordinates is given by

$$\begin{aligned} \dot{a} = \ & -\frac{\epsilon}{\omega m}\left[\phi(a\cos(\omega t + \theta), -a\omega\sin(\omega t + \theta)) + \right. \\ & \left. c(a\omega\sin(\omega t + \theta)) + g(t)\right]\sin(\omega t + \theta) \\ \dot{\theta} = \ & -\frac{\epsilon}{\omega m}[\phi(a\cos(\omega t + \theta), -a\omega\sin(\omega t + \theta)) \\ & +c(a\omega\sin(\omega t + \theta)) + g(t)]\cos(\omega t + \theta). \end{aligned} \tag{2.4}$$

Evidently dynamics in Eq.2.4 is time varying and nonlinear.

In the case of single frequency excitation ($\tilde{g}(t) = E\sin\omega t$), the dynamics of Eq.2.4 is periodic with period $(2\pi/\omega)$. The first order periodic averaging [24] theorem states that

Theorem 2.2.1 (First order periodic averaging). *Consider*

$$\begin{aligned} \dot{x} &= \epsilon f(t, x); \qquad x(0) = x_0; \ \textit{and} \\ \dot{x}_{av} &= \epsilon f_{av}(x_{av}); \quad x_{av}(0) = x_0 \end{aligned} \tag{2.5}$$

where $f(t, x)$ is T periodic function in the variable t and $f_{av}(x) := \frac{1}{T}\int_0^T f(\tau, x)d\tau$. Then with mild assumptions on f, there exist constants L and M such that $sup_{t\in[0,\frac{L}{\epsilon}]}|x(t) - x_{av}(t)| \leq M\epsilon$.

Application of Theorem 2.2.1 to the nonlinear time varying dynamics of Eq.2.4 results in the averaged time-invariant dynamics as described below (where with some abuse of notation the averaged amplitude and phase are also represented by a and θ):

$$\begin{aligned} \dot{a} &= -\frac{c_e(a)}{2m}a - \frac{\epsilon}{2m\omega}E\sin\theta, \\ \dot{\theta} &= \omega_e(a) - \omega - \frac{\epsilon}{2ma\omega}E\cos\theta, \end{aligned} \tag{2.6}$$

where

$$\begin{aligned} \omega_e^2(a) &= \omega^2 - \frac{2}{am}\overline{\Phi}_c, \\ \frac{c_e(a)}{2m} &= \frac{\tilde{c}}{2m} + \frac{1}{am\omega}\overline{\Phi}_d, \end{aligned} \tag{2.7}$$

with

$$\begin{aligned} \overline{\Phi}_c &= (1/2\pi)\int_0^{2\pi}\tilde{\phi}(a\cos\psi, -a\omega\sin\psi)\cos\psi d\psi \\ \overline{\Phi}_d &= (1/2\pi)\int_0^{2\pi}\tilde{\phi}(a\cos\psi, -a\omega\sin\psi)\sin\psi d\psi. \end{aligned} \tag{2.8}$$

By reverting the averaged dynamics (Eq.2.6) in the (a, θ) coordinates to the original $(p, \dot{p})$ coordinates, the following equation can be shown to hold

$$\ddot{p} + \frac{c_e(a)}{m}\dot{p} + \omega_e(a)^2 p = \frac{1}{m}\tilde{g}(t). \tag{2.9}$$

The above dynamics describes an *equivalent cantilever* with changed resonant frequency ω_e and damping c_e (depending on the slowly varying parameter a) with no nonlinear tip-sample interaction (Figure 2.2). The equivalent stiffness is defined as $k_e := m\omega_e^2$ and equivalent quality factor as $Q_e := \left(\sqrt{k_e m}/c_e\right)$. It follows from Eq.2.7, that the change in the stiffness and damping coefficient are given by $-(2/a)\,\overline{\Phi}_c$ and $(2/a\omega)\,\overline{\Phi}_d$ respectively.

To verify the *equivalent cantilever* model (Eq.2.9), simulations using a piece-wise linear model[23, 25] of tip-sample interaction and cantilever modeled as a second order system with $f_0 = 70kHz$ and $Q = 200$ were performed. The model of the intermittent contact mode dynamics with the piece-wise linear model is described in Figure 2.1(c). The negative spring accounts for the long range attractive forces and the positive spring accounts for the short range repulsive forces. The dampers account for the energy dissipation in the sample and the variable l characterizes the tip-sample separation. It

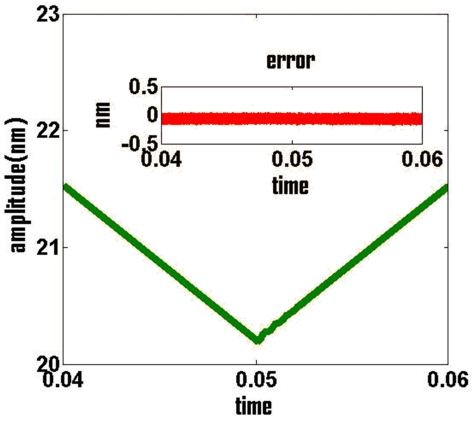

Figure 2.3: Shows the amplitude of the first harmonic. In the approach phase (from time 0.04 to 0.05) the amplitude reduces from $21.5nm$ to $20.2nm$ and in the retract phase the amplitude recovers to 21.5nm. The amplitude as obtained by the averaged dynamics closely follows the original amplitude shown; the inset shows the error to be within $\pm 0.1nm$

can be summarized as,

$$\tilde{\phi}(p,\dot{p}) = \begin{cases} 0 & \text{if } p \geq -(l-d) \\ -\omega_a^2(p+l-d) + c_a\dot{p} & \text{if } -l \leq p < -(l-d) \\ \omega_b^2(p+l) - \omega_a^2(p+l-d) + c_a\dot{p} + c_b\dot{p} & \text{if } p < -l. \end{cases} \tag{2.10}$$

For these simulations, *free air amplitude* (amplitude of the cantilever deflection when cantilever is not interacting with the sample) was chosen to be 24nm, and the mean tip-sample separation (l) was varied from 24nm to 20nm (approach phase) and back to 24nm (retract phase) linearly with time. Such measurement of the different aspects of the cantilever trajectory while linearly decreasing and then increasing the tip-sample separation is called a 'force curve' or 'approach-retract cycle'. Figure 2.3 shows simulation results that provide strong corroboration that the amplitude trajectories of the averaged dynamics (Eq.2.6) provide a good approximation to that of the original dynamics of Eq.2.4.

2.2.2 Deriving Sample Properties from Equivalent Cantilever Parameters

It is evident that from the knowledge of the nominal parameters (k, $\tilde{c}$ and ω), the equivalent cantilever parameters (k_e and c_e), and the amplitude a, it is possible to determine $\overline{\Phi}_c$ and $\overline{\Phi}_d$ (see Eq.2.7). As $\overline{\Phi}_d$ characterizes the difference between the equivalent damping and nominal damping (where sample is absent) and $\overline{\Phi}_c$ characterizes the difference between the equivalent resonant frequency and nominal resonant frequency (which relates to the stiffness), we can view $\overline{\Phi}_d$ and $\overline{\Phi}_c$ as characterizing the dissipative and conservative properties of the sample respectively. As $\overline{\Phi}_d$ is the dissipation force per cycle, $\overline{\Phi}_D := a\omega\overline{\Phi}_d$ is the energy dissipation per cycle. Furthermore, it can be shown that within an order ϵ

$$-\frac{1}{T}\int_0^T \phi(p,\dot{p})\dot{p}dt = \frac{1}{T}\int_0^T (c_e - \tilde{c})\dot{p}^2 dt = a\omega\overline{\Phi}_d \tag{2.11}$$

where $-(1/T)\int_0^T \phi(p,\dot{p})\dot{p}dt$ denotes the average power per period dissipated by the sample whereas $(1/T)\int_0^T (c_e - \tilde{c})\dot{p}^2 dt$ denotes the average power lost by a viscous damper in a spring-mass-damper system with damping coefficient $(c_e - \tilde{c})$. Thus the average power lost to the sample is equal to the average power lost by an equivalent viscous damper with coefficient $(c_e - \tilde{c})$ which is also equal to $\overline{\Phi}_D$. This further bolsters the equivalent cantilever description. It immediately follows from this discussion that if the sample is conservative then $\overline{\Phi}_d = 0$. A similar interpretation hold for $\overline{\Phi}_c$ (see [26]) where the notion of reactive power in electrical circuits is generalized to mechanical systems and it can be shown that $\overline{\Phi}_c$ represents the average reactive power.

2.2.3 Formulation of Equivalent Cantilever parameters estimation as system identification

To determine $\overline{\Phi}_c$ and $\overline{\Phi}_d$ from Eq.2.7, it is essential to determine the equivalent resonant frequency ω_e and damping c_e. We see that the equivalent cantilever parameters (Eq.2.7) depend on slowly varying amplitude a. It follows that if the estimation scheme is fast compared to the evolution of the amplitude dynamics, then the dynamics described by Eq.2.9 is a linear and time-invariant system in the estimation time scale. Thus the problem of estimating equivalent cantilever parameters is transformed to identification

of a linear time-invariant system (Eq.2.9) with the caveat that the estimation time scale should be shorter than the time scale of amplitude dynamics. In [10], authors have reported a method (the REEP algorithm) for recursively estimating the parameters of a second order system (Eq.2.9). It was observed experimentally and through simulations[10] that with mono-frequency excitation $\tilde{g}(t) = E\sin\omega t$ it was not possible to estimate the parameters of the second order system (Eq.2.9) within the desired time scale. It was concluded that multi-frequency forcing will make the estimation process more robust and faster and thus the excitation signal was chosen of the form, $\tilde{g}(t) = A\sin\gamma t + B_1\sin(\gamma-\alpha)t + B_2\sin(\gamma+\alpha)t$. The magnitudes B_1 and B_2 and the sideband frequencies $(\gamma \pm \alpha)$ are chosen to ensure that the trajectory of the cantilever is minimally altered when compared to the single frequency excitation while facilitating robustness in parameter estimation. It was shown in [10] that this is indeed possible and thus the entire operation maintains a dynamic mode behavior.

The need for $\tilde{g}$ to be richer than a single sinusoid implies that it is difficult to have $\tilde{g}$ to be periodic and thus *first order periodic averaging* (Theorem 2.2.1) is no longer applicable. Thus, the validity of the equivalent cantilever approximation has to be analyzed under the new excitation that has multitones. We now analyze how much multitone excitation effect the equivalent cantilever model.

2.2.4 Multitone Excitation

By using tools from [24], we derive equivalent cantilever concept for multitone excitation. The result is summarized in the following theorem.

Theorem 2.2.2. *Consider the dynamic system given by Eq.2.2 with forcing* $\tilde{g}(t) = A\sin\gamma t + B_1\sin(\gamma-\alpha)t + B_2\sin(\gamma+\alpha)t$ *where* γ *is such that*

$$\epsilon\Delta = \gamma^2 - \omega^2$$

with $\alpha = \mathcal{O}(\epsilon)$. *Then the system can be approximated by that of a linear system with equivalent damping coefficient* $c_e(a)$ *and equivalent resonant frequency* $\omega_e(a)$ *(as in Eq.2.9) forced by a input of the form* $\tilde{g}(t)$ *with error of* $\mathcal{O}(\epsilon)$ *on the time scale* $1/\epsilon$.

Proof. Equation 2.2 can be written as

$$\ddot{p} + \omega^2 p = \epsilon f(p,\dot{p}) + \epsilon E(t) \tag{2.12}$$

where

$$f(p,\dot{p}) = \frac{-c\dot{p} + \phi(p,\dot{p})}{m}; \quad E(t) = g(t)/m \tag{2.13}$$

Change of coordinates, as in Eq.2.3 gives

$$\begin{aligned} \dot{a} &= -\tfrac{\epsilon}{\gamma}[\Delta a\cos(\gamma t+\theta) + f(p,\dot{p}) + E(t)]\sin(\gamma t+\theta) \\ \dot{\theta} &= -\tfrac{\epsilon}{a\gamma}[\Delta a\cos(\gamma t+\theta) + f(p,\dot{p}) + E(t)]\cos(\gamma t+\theta) \end{aligned} \tag{2.14}$$

Here $f(p,\dot{p}) = f(a\cos(\gamma t+\theta), -a\gamma\sin(\gamma t+\theta))$ is periodic with period $2\pi/\gamma$. Equation 2.14 is exact, that is there are no approximation, and the vector field is sum of finite periodic fields, that is:

$$\begin{pmatrix} \dot{a} \\ \dot{\theta} \end{pmatrix} = -\epsilon F(a,\theta,t) =: \begin{pmatrix} F_1(a,\theta,t) \\ F_2(a,\theta,t) \end{pmatrix} \tag{2.15}$$

where F is sum of finite periodic vector fields. Thus averaging applies. Now,

$$g(t)\sin(\gamma t+\theta) = [A\sin\gamma t + B_1\sin(\gamma-\alpha)t + B_2\sin(\gamma+\alpha)t]\sin(\gamma t+\theta)$$

which gives

$$\begin{aligned} &g(t)\sin(\gamma t+\theta) = \frac{\cos\theta}{2}[A+\cos\alpha t(B_1+B_2)] + \frac{\sin\theta\sin\alpha t}{2}(B_2-B_1) - \\ &\frac{\cos(2\gamma t+\theta)}{2}[A+\cos\alpha t(B_1+B_2)] + \frac{\sin(2\gamma t+\theta)\sin\alpha t}{2}(B_2-B_1) \\ &=: f_1(t,\alpha t,\theta) \end{aligned} \tag{2.16}$$

Similarly,

$$\begin{aligned} &g(t)\cos(\gamma t+\theta) = -\frac{\sin\theta}{2}[A+\cos\alpha t(B_1+B_2)] + \frac{\cos\theta\sin\alpha t}{2}(B_2-B_1) \\ &+\frac{\sin(2\gamma t+\theta)}{2}[A+\cos\alpha t(B_1+B_2)] + \frac{\cos(2\gamma t+\theta)\cos\alpha t}{2}(B_2-B_1) \\ &=: f_2(t,\alpha t,\theta) \end{aligned} \tag{2.17}$$

This gives

$$\begin{aligned} F_1(a,\theta,t) &= \frac{1}{\gamma}[\Delta a\cos(\gamma t+\theta) + f(p,\dot{p})]\sin(\gamma t+\theta) + \frac{1}{\gamma\epsilon}f_1(t,\alpha t,\theta) \\ F_2(a,\theta,t) &= \frac{1}{a\gamma}[\Delta a\cos(\gamma t+\theta) + f(p,\dot{p})]\cos(\gamma t+\theta) + \frac{1}{a\gamma\epsilon}f_2(t,\alpha t,\theta) \end{aligned} \tag{2.18}$$

So equation 2.15 can be written as

$$\begin{pmatrix} \dot{a} \\ \dot{\theta} \end{pmatrix} = -\epsilon F(a, \theta, t, \alpha t) \tag{2.19}$$

Let us introduce the new independent variable $\tau = \alpha t$, then the system can be written as

$$\begin{pmatrix} \dot{a} \\ \dot{\theta} \end{pmatrix} = -\epsilon F(a, \theta, t, \tau) \qquad \dot{\tau} = \alpha \tag{2.20}$$

with appropriate initial conditions. As F is periodic over $2\pi/\gamma$, we can average the system over t keeping τ constant, which gives the averaged equations

$$\begin{pmatrix} \dot{a_{av}} \\ \dot{\theta_{av}} \end{pmatrix} = -\epsilon F^0(a_{av}, \theta_{av}, t, \tau_{av}) \qquad \dot{\tau_{av}} = \alpha \tag{2.21}$$

or

$$\begin{pmatrix} \dot{a_{av}} \\ \dot{\theta_{av}} \end{pmatrix} = -\epsilon F^0(a_{av}, \theta_{av}, t, \alpha t) \tag{2.22}$$

where $F^0() = (\gamma/2\pi) \int_0^{2\pi/\gamma} F()\, dt$

Then from [24], we have $a_{av}(t) - a(t) = \mathcal{O}(\epsilon)$, and $\theta_{av}(t) - \theta(t) = \mathcal{O}(\epsilon)$ on the time scale $1/\epsilon$. After averaging F over the period $2\pi/\gamma$, and making the approximation $2\gamma \approx \gamma + \omega$, we finally get

$$\begin{aligned} \dot{a} &= -\frac{c_e(a)a}{2m} - \frac{1}{\gamma}\left[\frac{\cos\theta}{2}\left(A + (B_1 + B_2)\cos\alpha t\right) + \frac{\sin\theta\sin\alpha t}{2}(B_2 - B_1)\right] \\ \dot{\theta} &= \omega_e(a) - \omega + \frac{1}{a\gamma}\left[\frac{\sin\theta}{2}\left(A + (B_1 + B_2)\cos\alpha t\right) - \frac{\cos\theta\sin\alpha t}{2}(B_2 - B_1)\right] \end{aligned} \tag{2.23}$$

where, the equivalent damping coefficient c_e and resonant frequency ω_e are again given by Equation 2.7. □

Comparing Eq.2.23 to Eq.2.6, effect of multiple sine excitation is clear in terms of extra terms in the (a, θ) dynamics. As in the case of single sinusoid excitation,

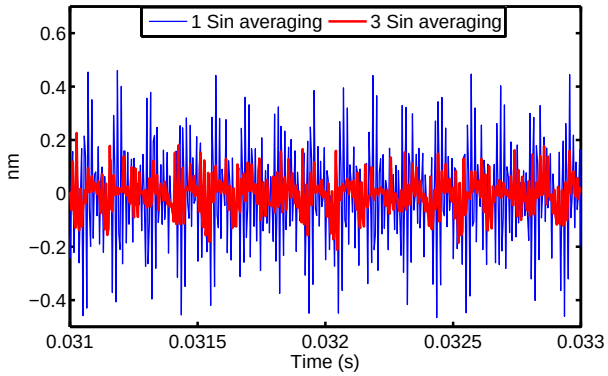

Figure 2.4: Simulation results for difference in steady state trajectories of actual simulation with monotone averaged equations and averaged equations with multitone excitation for a step input of $1nm$. Clearly multitone averaging is able to better approximate the trajectories

by reverting the dynamics of Eq.2.23 in the (a, θ) coordinates to the original $(p, \dot{p})$ coordinates, Eq.2.9 can be recovered. Thus the solution is equivalent to that of a linear system with damping coefficient c_e and resonant frequency ω_e forced by a input of form $g(t)$, thus further bolstering the equivalent cantilever concept for multitone excitation and consequentially the validity of the REEP algorithm. Even with the multitone input, we see that the relationship between the equivalent parameters (ω_e and c_e) and sample properties (through $\overline{\Phi}_d$ and $\overline{\Phi}_c$) remain unchanged.

Further simulations were done to validate these result using the piece-wise linear model of Eq.2.10. Free air amplitude was again chosen to be 24nm, and square pulses of $1nm$ to the tip-sample interaction length was given as sample. Equations 2.6 and 2.23 were solved simultaneously and difference in trajectories determined via averaged equations and the results of a comprehensive non-linear simulation are described in Figure 2.4. It is seen that the steady state rms error of multitone averaging equations is lesser ($\approx$60% less) when compared to the monofrequency averaging equations.

2.3 Multimode Approximations

We saw that under the one-mode approximation, the approach for determining equivalent cantilever parameters necessitates the use of multi-frequency input. It is crucial to determine what is the effect of the input on additional modes and/or means of ascertaining extent of participation of the higher modes. There are attempts in the literature to address these operation modalities (see [27, 28] and the book [29]), however, as asserted in [29], the understanding on local material properties is scant. Also, to the best of the author's knowledge existing research has not leveraged averaging theory for facilitating determination of material properties in real-time particularly when multiple modes are involved. Taking the cue from the one-mode case, we develop an enabling paradigm that can elucidate the physics by evaluating whether an equivalent linear time-invariant system can be reached when multiple modes and multifrequency inputs are involved. We next present the challenges and approach toward this goal.

2.3.1 Challenges and Approach

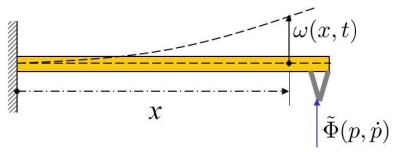

Figure 2.5: An Euler-Bernoulli beam

In the dynamic mode, the cantilever tip interacts with the sample only intermittently. Thus it is intuitive that the mode shapes are mostly dictated by the fixed-free boundary conditions. The unforced Euler-Bernoulli beam (see Fig. 2.5) with one end fixed (at $x = 0$) and another end free (at $x = L$) is described by

$$EI\frac{\partial^4 w(x,t)}{\partial x^4} + \rho A\frac{\partial^2 w(x,t)}{\partial t^2} = 0 \tag{2.24}$$

$$w(0,t) = 0,\ \tfrac{\partial w(0,t)}{\partial x} = 0;$$
$$EI\tfrac{\partial^2 w(L,t)}{\partial^2 x} = 0, EI\tfrac{\partial^3 w(L,t)}{\partial^3 x} = 0$$

where $w(x,t)$ is the deformation at x and time t, with $E,\ I,\ \rho,\ A$ representing appropriate cantilever properties.

We will assume that the natural mode shapes are described by $\psi_j(x)$. We will further assume that the external excitation to the cantilever is provided as a forcing $\tilde{g} = \epsilon g(t)$ at x_{exc} (point where the external forcing is applied on the beam) and the tip sample interaction forcing is given by $\tilde{\Phi}(p, \dot{p})$ at $x = L$ where $p(t) := w(L, t)$. Assuming an N mode approximation, it can be shown using variational principles (see [4]) that $w(x, t) = \sum_{i=1}^{N} \psi_j(x) q_j(t)$ where $q_j(t)$ satisfies

$$m_j \ddot{q_j} + \tilde{c}_j \dot{q_j} + k_j q_j = \tilde{g}_j(t) + \tilde{\Phi}_j(p, \dot{p}) \tag{2.25}$$

with $\tilde{g}_j(t) = \psi_j(x_{exc})\tilde{g}(t)$ and $\tilde{\Phi}_j(t) = \psi_j(L)\tilde{\Phi}(p, \dot{p})$. Let $g_j(t) = \psi_j(x_{exc})g(t)$ and $\Phi_j(t) = \psi_j(L)\Phi(p, \dot{p})$, then

$$\ddot{q_j} + \omega_j^2 q_j = \frac{\epsilon}{m_j}(g_j(t) + \Phi_j(p, \dot{p}) - c_j \dot{q_j}) \tag{2.26}$$

where $\omega_j = \sqrt{k_j/m_j}$. Taking inspiration from the one-mode case we introduce new variables a_j and θ_j via

$$q_j = a_j \cos(\omega_j t + \theta_j), \quad \dot{q_j} = -a_j \omega_j \sin(\omega_j t + \theta_j). \tag{2.27}$$

The (a_j, θ_j) dynamics is given by

$$\begin{array}{rcl} \frac{d}{dt}\begin{pmatrix} a_j \\ \theta_j \end{pmatrix} & = & \epsilon \begin{pmatrix} -\frac{f_j}{m_j \omega_j} \sin(\omega_j t + \theta_j) \\ -\frac{f_j}{m_j a_j \omega_j} \cos(\omega_j t + \theta_j) \end{pmatrix} \\ & =: & \epsilon \begin{pmatrix} h_{ja} \\ h_{j\theta} \end{pmatrix} =: \epsilon \boldsymbol{h}_j(\boldsymbol{a}, \boldsymbol{\theta}, t) \end{array} \tag{2.28}$$

where $f_j = [g_j(t) + c_j a_j \omega_j \sin(\omega_j t + \theta_j) + \Phi_j(\sum_{j=1}^{\infty} a_j \cos(\omega_j t + \theta_j), \sum_{j=1}^{\infty} -a_j \omega_j \sin(\omega_j t + \theta_j))] =: f_j(\boldsymbol{a}, \boldsymbol{\theta}, t)$ with $\boldsymbol{a} := (a_1, \ldots, a_N)$ and $\boldsymbol{\theta} = (\theta_1, \ldots, \theta_N)'$. It is thus evident from (2.28), that the j^{th} amplitude a_j and phase θ_j dynamics are $O(\epsilon)$. However, due to the presence of multiple modal frequencies, even if the excitation $\tilde{g}(t)$ is chosen to be periodic, $\boldsymbol{h} := (\boldsymbol{h}_1, \boldsymbol{h}_2, \ldots, \boldsymbol{h}_N)'$ will not be periodic in time t and thus the averaging theorem (Theorem 2.2.1) cannot be applied. We will employ the notion of *generalized average* h^o of h defined via

$$\begin{array}{rcl} \boldsymbol{h}^o(\boldsymbol{a}, \boldsymbol{\theta}) & = & (\boldsymbol{h}_1^o, \boldsymbol{h}_2^o, \ldots, \boldsymbol{h}_N^o)', \text{ with} \\ \boldsymbol{h}_j^o(\boldsymbol{a}, \boldsymbol{\theta}) & = & \lim_{T \to \infty} \frac{1}{T} \int_0^T \boldsymbol{h}_j(\boldsymbol{a}, \boldsymbol{\theta}, t) dt. \end{array} \tag{2.29}$$

It will also be important to determine how much the generalized average $\boldsymbol{h}^o$ differs from the time dependent $\boldsymbol{h}$ on a time scale $\frac{1}{\epsilon}$. Here, we will use the measure

$$\delta(\epsilon) := \sup_{(\boldsymbol{a},\boldsymbol{\theta})\in D} \sup_{t\in[0,L_t/\epsilon]} \epsilon \int_0^t [\boldsymbol{h}(\boldsymbol{a},\boldsymbol{\theta},\tau) - \boldsymbol{h}^o(\boldsymbol{a},\boldsymbol{\theta})]d\tau \tag{2.30}$$

where D is some domain where we can determine that the amplitudes and phases remain in and L_t can be any strictly positive constant. With these definitions the following theorem holds [24].

Theorem 2.3.1 (General First order averaging). *Consider*

$$\begin{aligned} \tfrac{d}{dt}\begin{pmatrix} a_j \\ \theta_j \end{pmatrix} &= \epsilon \begin{pmatrix} h_{ja}(\boldsymbol{a},\boldsymbol{\theta},t) \\ h_{j\theta}(\boldsymbol{a},\boldsymbol{\theta},t) \end{pmatrix} \text{ and} \\ \tfrac{d}{dt}\begin{pmatrix} a_j \\ \theta_j \end{pmatrix}_{av} &= \epsilon \begin{pmatrix} h^o_{ja}(\boldsymbol{a}_{av},\boldsymbol{\theta}_{av}) \\ h^o_{j\theta}(\boldsymbol{a}_{av},\boldsymbol{\theta}_{av}) \end{pmatrix} \end{aligned}$$

with the same initial conditions. Then on a time scale $\frac{1}{\epsilon}$ *the corresponding solutions differ at most by* $O(\delta(\epsilon))$.

The above result forms the analogue of Theorem 2.2.1 for the time periodic case with the added onus of estimating the order of $\delta(\epsilon)$ (for the periodic case $\delta(\epsilon) = O(\epsilon)$). Averaged equations for a_j and θ_j are obtained by evaluating $\boldsymbol{h}^o$ which results in (we have dropped the av subscript):

$$\begin{aligned} \dot{a_j} &= -\frac{c_{jeq}(\boldsymbol{a},\boldsymbol{\theta})a_j}{2m_j} \\ &\quad -\frac{1}{m_j\omega_j}\lim_{T\to\infty}\frac{\epsilon}{T}\int_0^T g_j(t)\sin(\omega_j t+\theta_j)dt \\ \dot{\theta_j} &= \omega_{jeq}(\boldsymbol{a},\boldsymbol{\theta}) - \omega_j \\ &\quad -\frac{1}{m_j a_j\omega_j}\lim_{T\to\infty}\frac{\epsilon}{T}\int_0^T g_j(t)\cos(\omega_j t+\theta_j)dt \end{aligned} \tag{2.31}$$

where

$$\begin{aligned} \frac{c_{jeq}(\boldsymbol{a},\boldsymbol{\theta})}{2m_j} &= \frac{\tilde{c}_j}{2m_j} + \frac{1}{a_j m_j\omega_j}\tilde{\Phi}_{jd} \text{ and} \\ \omega_{jeq}(\boldsymbol{a},\boldsymbol{\theta})^2 &= \omega_j^2 - \frac{2}{a_j m_j}\tilde{\Phi}_{jc}, \text{ with} \end{aligned} \tag{2.32}$$

$$\begin{aligned}
\tilde{\Phi}_{jd} &:= \lim_{T\to\infty}\frac{1}{T}\int_0^T \tilde{\Phi}_j(\sum_{j=1}^{N} a_j\cos(\omega_j t+\theta_j) \\
&\quad \textstyle\sum_{j=1}^{N} -a_j\omega_j\sin(\omega_j t+\theta_j))\sin(\omega_j t+\theta_j)dt \\
\tilde{\Phi}_{jc} &:= \lim_{T\to\infty}\frac{1}{T}\int_0^T \tilde{\Phi}_j(\sum_{j=1}^{N} a_j\cos(\omega_j t+\theta_j) \\
&\quad \textstyle\sum_{j=1}^{N} -a_j\omega_j\sin(\omega_j t+\theta_j))\cos(\omega_j t+\theta_j)dt
\end{aligned}$$

The multi-mode averaged dynamics thus mirror the dynamics of the one mode case with $\tilde{\Phi}_{jd} = \tilde{\Phi}_{jd}(\boldsymbol{a},\boldsymbol{\theta})$ and $\tilde{\Phi}_{jc} = \tilde{\Phi}_{jc}(\boldsymbol{a},\boldsymbol{\theta})$ dependent on N amplitudes a_j and phase θ_j.

2.3.2 Energy Dissipation in each mode

Similar to the one mode case, it can be shown that the contribution to the sample dissipation power due to the deformation caused by the j^{th} mode of the cantilever, given by $\lim_{T\to\infty} -\frac{1}{T}\int_0^T \tilde{\Phi}\dot{q}_j dt$, is equal to $\lim_{T\to\infty}\frac{1}{T}\int_0^T (c_{jeq}-\tilde{c}_j)\dot{q}_j^2 dt$. Thus as was the case with the one mode approximation under the sample's influence the damping coefficient in the j^{th} mode can be considered as c_{jeq}, with the damping change caused by the sample in the j^{th} mode given by $c_{jeq}-\tilde{c}_j$. Again as in the one mode case if the sample is conservative, it can be shown that the total energy dissipation $\lim_{T\to\infty} -\sum_{j=1}^{N}\frac{1}{T}\int_0^T \tilde{\Phi}\dot{q}_j dt = 0$. In a similar manner the j^{th} resonant frequency due to sample interaction changes to ω_{jeq}. Thus the j^{th} mode dynamics are governed by $m_j\ddot{q}_j + c_{jeq}\dot{q}_j + k_{jeq}q_j = \tilde{g}_j$ and with the transfer function $\frac{1}{m_j s^2+c_{jeq}s+k_{jeq}}$. Noting that $p(t) = \psi(L,t) = \sum_{j=1}^{N}\Psi_j(L)q_j(t)$ it follows that

$$\hat{p}(s) = \sum_{i=1}^{N}\frac{\psi_j(L)\hat{\tilde{g}}_j}{m_j s^2 + c_{jeq}s + k_{jeq}} \tag{2.33}$$

With the above development, assuming that the variables a_j and θ_j evolve on a slow time scale, the task is to identify a linear time invariant system of the form (2.33) from noisy measurement $y = p + v$. If the equivalent parameters k_{jeq} and c_{jeq} are determined, sample properties $\tilde{\Phi}_{jd}$ and $\tilde{\Phi}_{jc}$ can be evaluated. Summarizing the strategy for the multimode case consists of (a) arriving at an equivalent linear system (2.33) (b) estimating the coefficients of the linear system (2.33) via REEP (c) Obtaining the dissipative and the reactive power of the sample in the j^{th} mode (the weighted sum will provide the net dissipative and conservative (reactive) power).

2.3.3 Tool to analyze Resonance Conditions:

Crucial for the validity of the assertions in the above discussion is the order of $\delta(\epsilon)$; this estimate can also serve as a means to analyze resonance conditions. Resonance conditions can easily render $\delta(\epsilon)$ to be, for example, $O(1)$. We illustrate with a simple argument. Consider the case when only one mode is involved, with a forcing $g_1(t) = E\sin(\omega_1 + \alpha)t$ where ω_1 is the first modal frequency. The generalized average r^o of $r(t) := g_1(t)\cos(\omega_1 t + \theta_1)$ which appears in averaged equation (2.31), is given by $\lim_{T\to\infty} \frac{1}{T}\int_0^T g_1(t)\cos(\omega_1 t + \theta_1)dt = \lim_{T\to\infty} \frac{1}{T}\int_0^T [E\sin(-\alpha_1 t + \theta_1) + E\sin(2\omega_1 t + \alpha t + \theta_1)]dt = 0$ (as the generalized average of periodic functions is zero). However, if α is $O(\epsilon)$ then with t being $O(\frac{1}{\epsilon})$, $\int_0^t [E\sin(-\alpha_1 t + \theta_1)dt$ is $O(\frac{1}{\epsilon})$ and thus $\delta(\epsilon)$ is $O(1)$. *Thus a near-resonance condition where the forcing frequency is close to the modal frequency will lead to generalized averaging, not yielding the desired result.* We remark that it is possible to arrive at an averaged dynamics when the forcing is near resonance and the behavior is closer to the resonance condition given by the averaged dynamics (2.6). Furthermore the above discussion also indicates that $\delta(\epsilon)$ forms an effective tool for determining resonances.

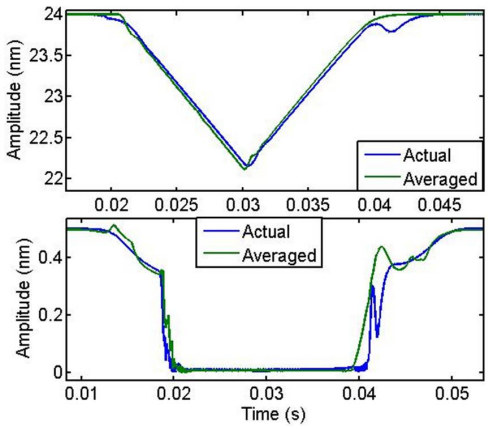

Figure 2.6: Simulation results for the two-mode approximation of the cantilever dynamics compared with the averaged equations. (a) shows the amplitudes of the resonant frequency of the first mode, and (b) shows the amplitudes of the resonant frequency of the second mode.

2.3.4 Simulation results and Conclusion

Simulations were performed in MATLAB on the piece-wise linear model of tip-sample interaction (Equation 2.10) and a two mode model of the AFM cantilever was considered. First mode has a resonant frequency $f_{01} = 70kHz$ with quality factor $Q_1 = 200$ and the second mode has a resonant frequency $f_{02} = 6.3 \times f_{01}$ with quality factor $Q_2 = 1000$ (these are the typical parameters of the Olympus AC240TS cantilever). Cantilever was excited with a sum of two sinusoids (the first and second modal frequencies) such that with no sample interaction, the magnitude of the cantilever deflection at the first modal frequency (termed as the amplitude at the first mode) was $24nm$. Similarly the amplitude at the second mode was $0.5nm$. Amplitudes for both modes were calculated by demodulating the cantilever trajectory of the non-autonomous system of (2.25) at the two resonant frequencies. Averaging equation (2.31) for the two modes was considered and solved in MATLAB. Infinite integral in (2.31) was suitably approximated with a finite T during the simulation. Amplitudes calculated for both modes were compared to the ones calculated via solving the actual dynamical equations. Figure 2.6 shows the simulation results where the sample is slowly raised ($2nm$) towards the cantilever tip (in the approach phase) till 0.03 seconds and then retracted away from the sample (in the retract phase). The amplitudes at the first mode and second mode are then compared with the averaged equations. We see that the averaged dynamics do indeed match the actual amplitudes . This provides evidence that averaging theory based results can be used and thus directs the future research to the determination of equivalent parameters and subsequently the sample dissipation and reactive power at higher modes.

We have extended the equivalent cantilever paradigm to the multi-mode model of the cantilever and showed simulation results supporting the model in the case of two-mode approximation. The paradigm laid out is quite general with a potential for wide applicability. Pertinent questions include, what kind of materials is it beneficial to involve higher modes and multi-frequency excitation; when do the estimates on dissipation and stiffness remain meaningful; are there alternate forms of representing averaged dynamics under which the error from the original remain small. We have provided directions based on averaging theory to address such questions.

2.4 Recursive Estimation of Equivalent Parameters

In the section 2.2.4, the concept of *equivalent cantilever* was corroborated for the multi frequency excitation which is required for estimation of equivalent parameters. Now, we present the details of the REEP algorithm. A general schematic of REEP [10] setup is shown in Figure 2.7. The cantilever is excited with a sum of three sinusoids via dither piezo. Apart from central frequency of excitation (which is at or close to the first modal resonant frequency of the cantilever), two side frequencies are chosen to provide enough frequency content to the deflection signal ascertaining the fast convergence of recursive algorithm. Amplitudes of these side bands are set such that the orbit of the cantilever deflection does not differ much from nominal dynamic mode operation. A general discretized second order dynamics that represents the *equivalent cantilever* can be written as,

$$\begin{aligned} e(n) &= \vartheta(n) + b_1\vartheta(n-1) + b_0\vartheta(n-2) \\ u(n) &= a_2 g(n) + a_1 g(n-1) + a_0 g(n-2) \\ p(n) &+ b_1 p(n-1) + b_0 p(n-2) = u(n) + e(n), \end{aligned} \tag{2.34}$$

where $p(n)$ and $g(n)$ denote the cantilever deflection and dither forcing at sampled time $t = nT_s$ where T_s is the sampling interval, a_i's and b_i's are respectively the numerator and denominator of the second order discrete model of the *equivalent cantilever* and $\vartheta(n)$ is zero mean white measurement noise with variance σ^2_ϑ.

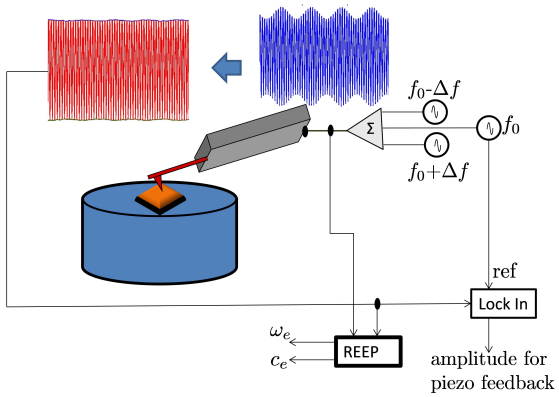

Figure 2.7: Schematic of REEP setup using a sum of three sinusoids as the drive signal to the cantilever. Two side frequencies are chosen such that the orbit of the cantilever deflection does not differ much from the tapping mode operation.

On identification of *equivalent cantilever* (plant) at different levels of tip-sample interaction, via frequency sweep, it was observed that the coefficients a_2, a_1 and a_0, which capture the delays in the system, do not change much and contribute to the response of system at frequencies considerably away from the cantilever resonance. Subsequently the values of a_2, a_1 and a_0 are fixed to the sample-free model values and b_1, b_0 are the remaining parameters to be estimated. Eq.2.34 can be written as

$$z(n) = \underbrace{[b_1 \; b_0]}_{\theta} \underbrace{\begin{bmatrix} -p(n-1) \\ -p(n-2) \end{bmatrix}}_{\phi(n)} + e(n) \tag{2.35}$$

where θ represents the vector of unknown parameters and $z(n) = p(n) - a_2 g(n) - a_1 g(n-1) - a_0 g(n-2)$. At any time instant $t = nT_s$, past data $z(k)$ and $\phi(k)$ for $k = 0, 1, ...n$ are available. In [10], an estimate $\hat{\theta}_{LS}$ of θ was determined recursively by solving an exponentially weighted least square problem,

$$\min_{\hat{\theta}_{LS}(n)} \sum_{k=0}^{n} \lambda^{n-k} (z(k) - \hat{\theta}_{LS}(n)\phi(k))^2. \tag{2.36}$$

Here $e(n)$ is correlated and it depends on $\vartheta(n)$, $\vartheta(n-1)$ and $\vartheta(n-2)$, which results

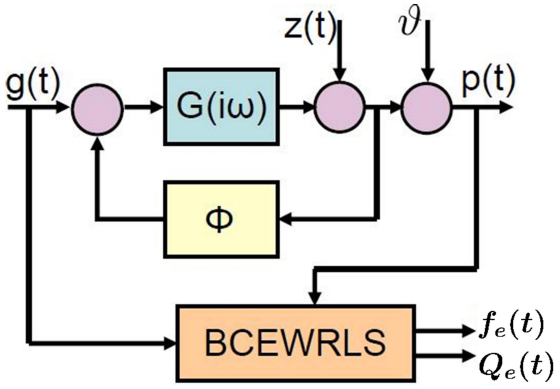

Figure 2.8: Modeling cantilever-sample interaction in tapping mode operation as a $G - \Phi$ interconnection where $G(i\omega)$ is the second order cantilever beam model and Φ is the nonlinear tip-sample force. $g(t)$, $z(t)$, ϑ and $p(t)$ are the dither forcing, the sample height profile, the measurement noise and measured cantilever deflection respectively. BCEWRLS algorithm takes $g(t)$ and $p(t)$ as input and provides the estimates of the equivalent resonant frequency, f_e, and quality factor, Q_e (which can be used to calculate k_e and c_e directly), of the cantilever in real time.

in the estimate $\hat{\theta}_{LS}(n)$ converging to θ within a bias. This generated a need to derive suitable bias correction term for the estimation. A Bias compensated *exponentially weighted* recursive least squares (BCEWRLS) method was developed as a handle on convergence rate of the parameter estimates is also required. Block diagram of the REEP algorithm is presented in Figure 2.8. The entire REEP algorithm can be summarized by following equations:

$$\begin{aligned}
\hat{\theta}_{LS}(n) &= \hat{\theta}_{LS}(n-1) + P(n)\phi(n)l(n) \\
l(n) &= \left[z(n) - \phi'(n)\hat{\theta}_{LS}(n-1)\right] \\
P(n) &= \frac{1}{\lambda}\left[P(n-1) - \frac{P(n-1)\phi(n)\phi'(n)P(n-1)}{\lambda + \phi'(n)P(n-1)\phi(n)}\right] \\
J(n) &= \lambda\left[J(n-1) + \frac{\left(z(n) - \phi'(n)\hat{\theta}_{LS}(n-1)\right)^2}{\lambda + \phi'(n)P(n-1)\phi(n)}\right] \\
\hat{\theta}_C(n) &= \frac{\hat{\sigma}^2(n)}{1-\lambda} nP(n)\hat{\theta}_C(n-1) \\
\hat{\sigma}^2(n) &= \frac{((1-\lambda)/n)J(n)}{1 + \hat{\theta}'_C(n-1)\hat{\theta}_{LS}(n)}
\end{aligned} \tag{2.37}$$

where λ is the exponential forgetting factor, $\hat{\theta}_{LS}(n)$ is the biased parameter estimate of θ at time instant $t = nT_s$ and $\hat{\theta}_C(n)$ is the bias compensated $\hat{\theta}_{LS}(n)$. $P(n)$ represents the variance of the error in the parameter estimates $(\theta - \hat{\theta}_{LS}(n))$ and $J(n)$ represents the least square error in equation 2.36 that is being minimized. $\hat{\sigma}^2(n)$ is an estimate of the variance of noise $e(n)$ at any instance. ω_e and Q_e can be calculated from estimated b_1 and b_0 values in closed form via

$$\begin{aligned}
p &= \frac{-1}{2T_s}\log(b_0) \\
q &= \frac{1}{T_s} acos\left(\frac{b_1}{-2e^{-pT_s}}\right) \\
f_e &= \frac{1}{2\pi}\sqrt{p^2+q^2} \\
Q_e &= \frac{\pi f_e}{p}
\end{aligned} \tag{2.38}$$

2.5 Off-line Experimental Results

Here a silicon cantilever, AC240TS, from Olympus with resonance frequency 78.837 kHz and spring constant 2 N/m (calculated using equi-partition method after taking

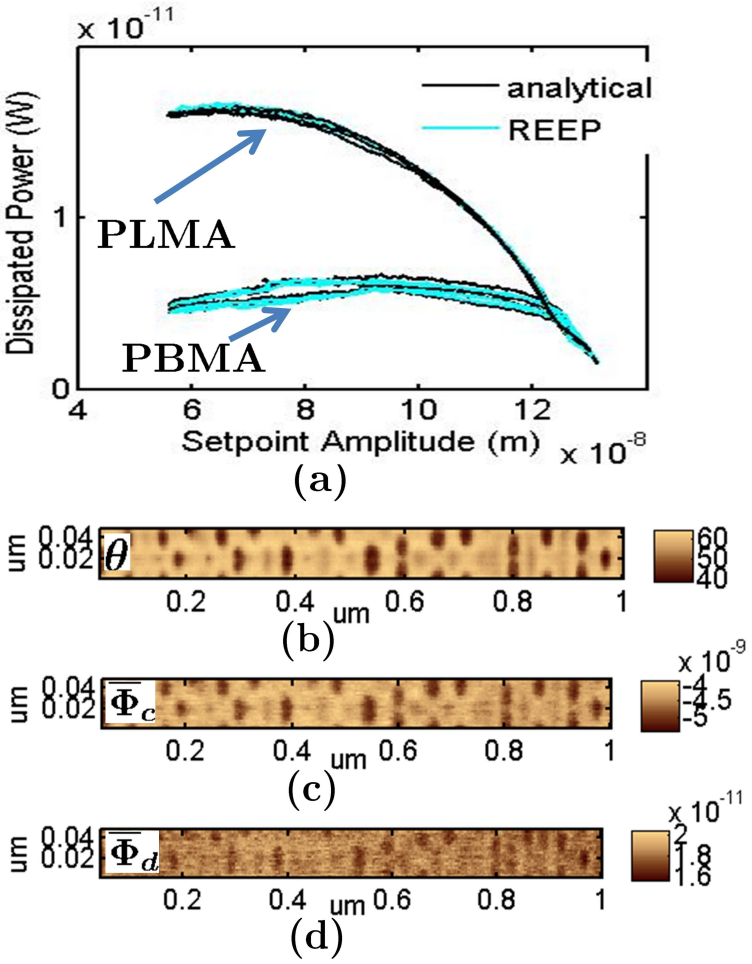

Figure 2.9: (Experimental Data; offline) (a) Comparison of power dissipated as determined by $\overline{\Phi}_D$ from REEP and via an analytical method described in [1] for two polymers PLMA and PBMA at two different locations for each polymer. It is known that PBMA is less dissipative than PLMA as confirmed with results shown. (b) the phase image (c) $\overline{\Phi}_c$ image (d) $\overline{\Phi}_d$ image of a SIBS block copolymer. The image size is $\approx 0.05\mu \times 1\mu$, stretched in y-axis by a factor of 2 to increase clarity. Note that high contrast that differentiates the domains of styrene (about $10nm$ in width) on isobutylene is high in the phase image. The contrast in $\overline{\Phi}_c$ image that characterizes the conservative (reactive) power is high; however, the contrast is minimal in the dissipative power characterized by $\overline{\Phi}_d$. Thus isobutylene and styrene have similar dissipative characteristics but different stiffness.

a thermal response) was used to evaluate the efficacy of the method. Experiments were performed on different polymer samples and the dither and deflection signals were sampled at 500 kHz simultaneously. The sampled data was used to obtain estimates of k_e and c_e off-line on MATLAB. Eq.2.7 was used to calculate $\overline{\Phi}_d$ and $\overline{\Phi}_c$. The sampled deflection signal was demodulated in MATLAB and the instantaneous amplitude was used to determine $\overline{\Phi}_D$. Figure 2.9(a) plots $\overline{\Phi}_D$ vs amplitude during an approach-retract cycle for two different polymers, PBMA and PLMA. It shows the agreement between the power dissipated as estimated by REEP and via analytical means[1] for experimental data obtained for both polymers. The data confirms that the REEP method does indeed provide good estimates of the power dissipated.

The real utility of REEP algorithm is the *simultaneous* determination of the *local stiffness* of the sample and the *local dissipation* which is evident in the $\tilde{\Phi}_c$ and $\tilde{\Phi}_d$ images of a SIBS (see materials section) block copolymer (see Figure 2.9(c) and (d)), where the data was collected off-line and the equivalent parameters estimated off-line. $\tilde{\Phi}_c$ and $\tilde{\Phi}_d$ were determined from the equivalent parameters. The net power dissipated due to interaction with the sample depends on the extent of the sample deformation caused by the intermittent contact with the tip; more compliant samples will lead to large deformation where as stiffer samples will lead to smaller deformation. Thus the contrast in the phase image is a combination of the intensive dissipativity and the compliance of the material. The experimental data in Figure 2.9 indicates that the contrast in the phase image is dominated by the different stiffness of styrene and isobutylene and only weakly affected by changes in intensive dissipative properties. These results indicate that, simultaneous determination of local stiffness and damping, will enable new capabilities toward understanding material properties. This study of a block copolymer also indicates the superior lateral resolution of the imaging method where nanometer sized domains are discernible.

2.5.1 Conclusion

We demonstrate that averaging/perturbation analysis can be fruitfully employed to envision, the possible complex system of probe interacting with the sample as a linear and time-invariant (LTI) system with parameters that are governed by the dissipation and stiffness of the material. Such a model holds in a time scale smaller than that of

the amplitude dynamics. Furthermore we have demonstrated that a real-time adaptive estimation of the parameters of the model can be realized within the time-scale in which the LTI assumption holds. The equivalent LTI model and the time-scale of its validity might also allow for determination of material properties such as electrical and thermal properties.

As mentioned earlier, rate of convergence of estimates of the equivalent parameters is faster than the rate of evolution of amplitude dynamics, this facilitates real-time estimation of these properties. Now when we have establish the validity of averaging theory and also the efficacy of REEP algorithm, a great need arises for the development of relevant hardware which can run the REEP algorithm in real-time. To study the change in mechanical properties due to change in various environmental or biological factors, a real-time implementation is a must. Next chapter will probe various different solutions available for such implementation and then describe the design implementation using the most appropriate one.

Chapter 3

Real-time Hardware Implementation of REEP Module

Over the course of multiple experiments cantilever dynamics change and often the cantilever has to be changed. It is desirable to have the ability of changing the module parameters conveniently to assess the ensuing effect on the performance of a given methodology. Having this ability allows for a realistic comparisons between alternate strategies as the experimental conditions, like the sample condition and cantilever, for the various strategies can be maintained same and associated variability can be factored out when determining which strategy performs better. DSP based solutions offer sleek implementation solutions in sense that all the major analog signals are sampled synchronized to a hardware clock and then the algorithm is essentially a C code which is extremely handy to change and write. Essential parameters of the algorithm can be changed during the test and thus there is considerable flexibility. DSP based solutions are severely crippled because of the limited closed loop bandwidth that they can offer. Best DSP solutions available are limited to MHz closed loop bandwidth not to mention that those boards are extremely expensive.

ASIC (application-specific integrated circuit) design is another alternative. However, exorbitant cost of design and fabrication, limited debugging capabilities and extremely long design cycle are considerable disadvantages of this methodology. FPGA (field-programmable gate array) based solution offers the best alternative. Cost involved is a

one time cost of the FPGA board. Hardware is re-configurable which means that if one needs to change the design or debug the design it can be done without any additional costs. Design reuse can be done. Once the blocks are designed, tested and stabilized, the same Intellectual Properties(IPs) can be used in future designs which reduces the design cycle considerably. The design parameters can be changed during the course of experiment from a PC. All the above reasons motivated the implementation of the REEP module on Xilinx Virtex 2-Pro30 board from Avnet Inc.

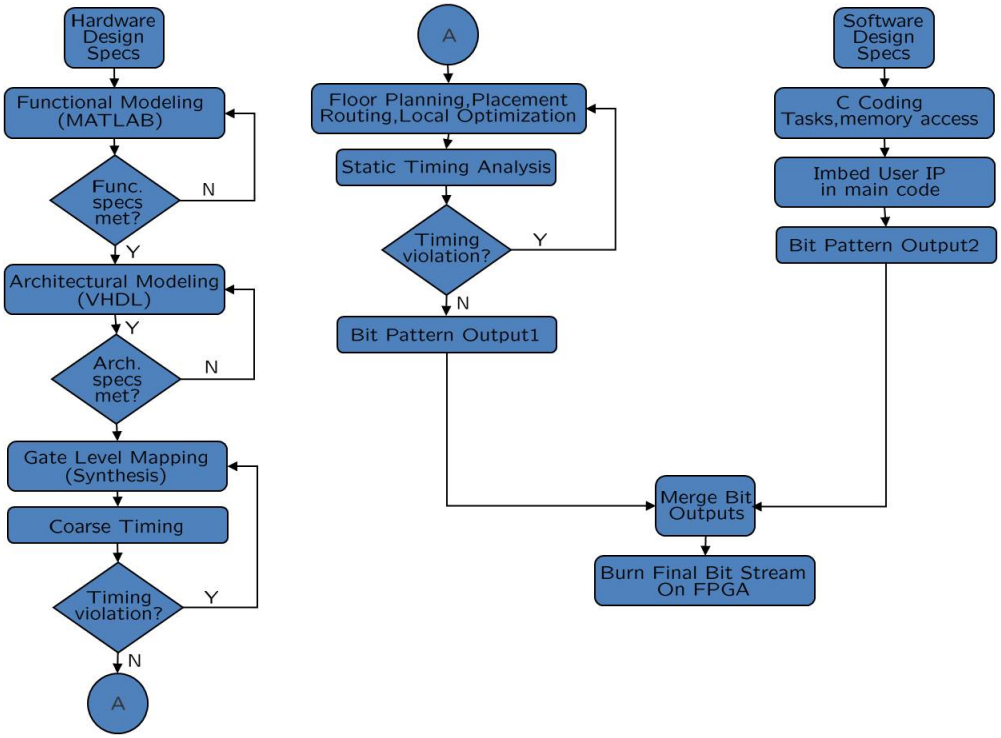

Figure 3.1: Digital Design Cycle

3.1 Digital Design Cycle

Digital Design Cycle for any digital block consists of a number of steps that take the design from specifications to eventual bit steam to be burned on an FPGA. This section will briefly discuss the various stages in digital design cycle and nuances of each stage. Any digital design start with specifications. This includes description of functional

specifications detailing what function this block is supposed to perform. This can be in the form of an equation, a finite state machine or a detailed algorithm. Top level specifications also include limits on required speed, area, power, noise, available clocks and the number of input/output pads. Specifications stage is followed by functional modeling stage. In this stage, tools like MATLAB, C etc are used to model top level functional architecture. This stage has nothing do to with clocks, speed, area etc. Entire algorithm or equation is divided into top level functional blocks and simulated to see if the design performs the task as desired. Once functional designing is done and tested to satisfaction, the design moves into architectural modeling stage. Each top level block is taken up one by one and it's input and output interface signals and formats are derived from top level specifications. Each block's operating clock frequency is decided. This stage deals with defining the architecture of the block and detailing what hardware will be used by the block. Architectural design has to take into care the specifications for area, power, speed, clocks and hardware constraints.

After the architectural code has been tested to satisfy all the functional constraints, this code is fed to digital synthesis tool. This tool has library information for all the basic digital design blocks. It has timing models, behavioral models and other company specific models for all the basic cells. This tool then interprets the RTL code based on standard syntax and maps the code to actual hardware units. This tool takes in clock descriptions and does a static timing analysis, at each optimization step, using the timing models that it has, to report any timing, area or power violations.

Next step is to do a top level floor planing. After that, the placement of cells is done in the remaining area depending on the interacting clock domains and domains interfacing with input and output cells. Completion of placement is followed by routing for all the wires. All these activities are taken care by automation tool with minimal user involvement. After a successful completion of all the steps, the design is ready to be converted into a bit stream. FPGA design cycle involves a second parallel activity. Xilinx FPGAs have an on chip processor (PowerPC) which can be used to communicate with external PC. The idea is to embed the above designed IP as a hard IP onto one of the buses of this processor and assign a unique address space to this IP. The CPU recognizes the memory blocks of this IP as registers on it's bus. These memory units can then be accessed from a C code running on embedded processor. The same code also

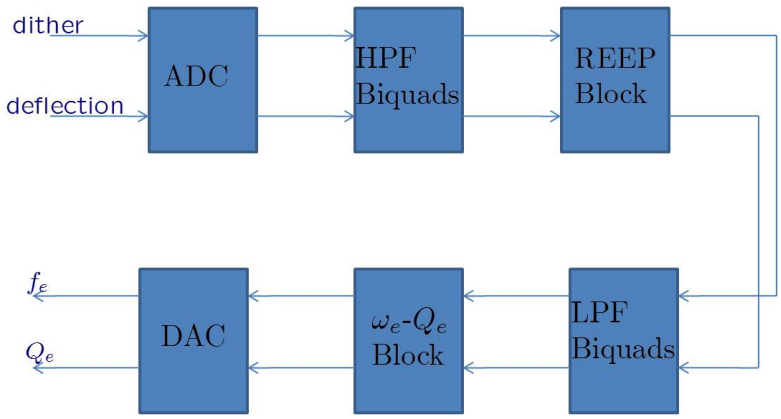

Figure 3.2: Top Level Block Diagram of the architecture

interfaces with PC via RS-232 serial port and thus can read or write on the memory units of the IP. Different parameters to be changed during the course of experiment can be assigned to these memory units so that they are accessible through a PC. The compiled code is output as a bit stream as well. The two bit streams are then merged and a final bit stream is prepared to be burnt onto the FPGA.

3.2 Individual Blocks

- REEP Block This is the main block running the recursive algorithm.
- Biquad Filters For input conditioning (see Figure 3.2), two high pass filters are needed. Mostly to remove Drift term and/or any DC bias in the inputs (deflection and dither). Also, two low pass filters to remove high frequency content of estimated b_0 and b_1. Total of 4 biquad filters (based on Sallen-key architecture) were implemented. Clippers were also needed so that estimated values always lie in the range of arguments of various functions to be used in ω_e and Q_e calculation.
- ω_e-Q_e block: This block implements equation of converting discrete parameters, b_0 and b_1, to continuous time estimates of equivalent resonant frequency ω_e and equivalent quality factor Q_e.
- ADC, DAC blocks: Analog-to-Digital Converters (ADC) and Digital-to-Analog Converters (DAC) were used to interface digital hardware with analog signals of

AFM.

- Configuration Block: As parameters of cantilever or operating conditions can change in real time. Need to configure certain signals in real time. These so called configurable signals include
  - Coefficients of the numerator of the plant transfer function,
  - Coefficients of the Biquads,
  - Various gains, biases and clipping limits,
  - And routing signals for debugging purpose.

A Simulink model of the algorithm, which includes RLS scheme of REEP, biquad structures and ω_e & Q_e calculation from b_0 and b_1 is built to determine the required precision representation of numbers. Due to the need of high precision and large numbers to operate with around the whole design, fixed point representation is ruled out. Next task is to find a suitable precision for floating point representation. First cut precision is chosen depending on the largest number to be used in the arithmetic (for exponent) and the appropriate error bounds (for mantissa). Comparing the simulation of the simulink model with above chosen precision is done with the model running at double precision. This process is reiterated till we get solution within required error bounds. Finally, by trial and error, precision of 8.29 for REEP and ω_e-Q_e block, and 10.34 for Biquads was set. The floating point arithmetic units like *adder, multiplier, divider* and *square-root* blocks as obtained from the open source floating point library FPLib*rary-v0.94*. They were modified to suit our purpose. The transcendental functions arctanh and arctan ae obtained from the Cordic library of the ISE Corgen. Note that, they operate only on fixed points. So the floating-to-fixed and fixed-to-floating point units were taken from the floating point library of the ISE Coregen. All the units were synthesized to have an *area estimate* and *delay estimate* which were then used to have a first-cut area and delay estimate of the individual blocks (like REEP, Biquads etc).

3.2.1 Building the Individual Modules

At this stage, various design steps are taken to implement the individual blocks. They are

- Deciding the Architecture

  At first step, complete algorithm is drawn in terms of the fundamental units.

- Scheduling

  Deciding the usage time period of fundamental units. Suppose we need 3 adders in a module, but none of them is used simultaneously. So we may decide to use just one adder unit and re-use it by deciding a suitable control logic, which will decide that which inputs it will take at a particular clock cycle. The Modules may not be sequential as described above. Then we have to trade-off between area (using more units) and delay (keeping an operation in wait) and do the scheduling accordingly. At any point during scheduling, one should make sure that no wait is introduced in the critical path as it will delay the entire operation. Sometimes we may share resources between modules and then we have to do a global scheduling (One divider is shared among REEP and ω_e-Q_e block). A suitable control logic for each fundamental unit is obtained which decides the inputs he unit will take at a particular clock cycle. Once we have verified the scheduling logic, we implement it using MUXes (i.e., which signals to be chosen for a particular unit at a particular clock cycle).

- Synthesis

  Each module is synthesized to note the difference between the actual area and the estimated one. Generally, the area increases from the estimated one because the MUXes used in control logic takes up considerable amount of area depending upon the bit width. If the difference is too large, we may have to go back and redo all the design steps. Here, we had to go back to make the modules share resources globally to meet the area requirements.

- Testing

  Finally, each individual block was extensively tested to ensure it perform as intended. All the testings were done on different approach-retract curve data.

3.2.2 Top Level Integration

Once all the individual modules are ready and tested, they are integrated to form the complete module. The area estimated from individual blocks may increase further owing to the wiring used in integration. If the increase is unacceptable, we may have to go back to first step and re-do the whole process. Hence, it is better to have safety margins at each previous stages. However, too conservative safety margins will hamper the performance of the module. The entire top level design was then thoroughly tested over experimental data sets to ensure proper functionality. Then as mentioned earlier, back-end activities like floor planing, placement and routing were performed. Finally all the constraints were met and module was ready to test on experiments.

3.2.3 Experiments and Results

Enabled by the new real-time capability of simultaneously imaging stiffness and dissipation in addition to the topography, we provide new insights on properties of a polymer blend. Experiments were performed on PBMA-PLMA polymer blend. An Olympus cantilever (AC160TS) with resonance frequency 334.7 kHz, spring constant 36 N/m (determined using the thermal response of the cantilever) and Quality factor of 491 was used on a MFP-3D, AFM. The FPGA module with a closed-loop bandwidth of 1.5 MHz was able to estimate the parameters of the equivalent cantilever accurately. Figures 3.3(a) and (b) show a comparison of the parameters as estimated offline using MATLAB and as estimated by the FPGA based real-time module. The results show a good match on the estimation of the equivalent resonant frequency $f_e(=\omega_e/2\pi)$ and equivalent quality factor Q_e determined while performing an approach-retract cycle on the PLMA polymer. Here, the dither excitation signal consisting a sum of 3 sinusoids was generated externally and fed to both the AFM and the FPGA. The deflection signal from AFM was buffered and supplied to the FPGA.

For imaging purposes, internal data acquisition channels of MFP-3D were used to save the two estimated parameters along with the height, amplitude and phase image. Figure 3.4 further verifies the real-time module where the equivalent parameters during a line scan are plotted. Figure 3.4 (a) compares the f_e estimated using the real-time FPGA module with the off-line estimates of MATLAB, while Figure 3.4 (b) compares

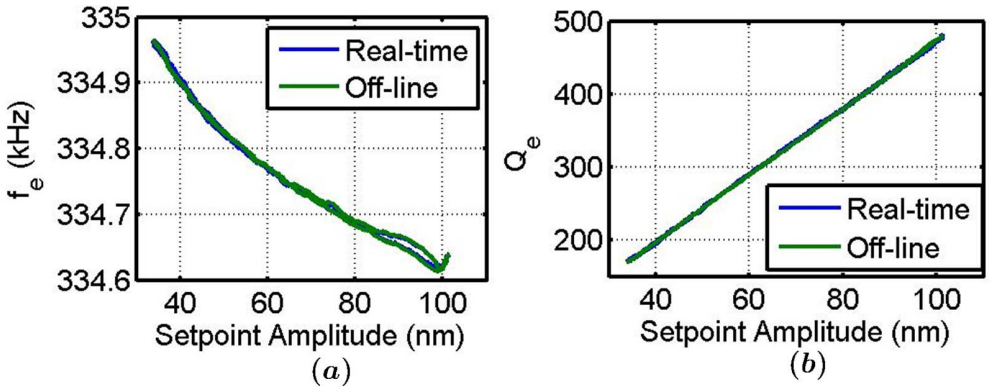

Figure 3.3: Figure shows a) equivalent resonant frequency and b) equivalent Quality factor vs amplitude 'approach-retract' curve on PLMA polymer as calculated from Matlab (Off-line, green curve) and FPGA module (real-time, blue curve). Both curves match each other verifying the estimates determined by real-time module.

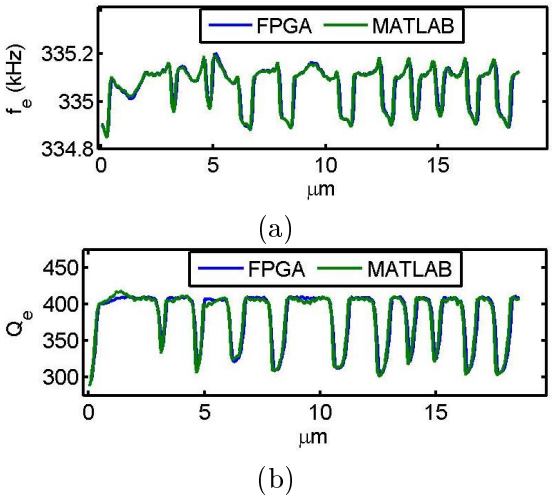

Figure 3.4: Figure compares the estimates of a) equivalent resonant frequency and b) equivalent quality factor obtained via the real-time module with the off-line estimates of MATLAB during a line scan of imaging a $20\mu m \times 20\mu m$ image of a PBMA-PLMA polymer blend. The small difference in the estimates is due to the analog noise present in the analog FPGA signal.

the estimated Q_e. The real-time estimates of FPGA are available as analog signals which are then sampled using data acquisition systems. So they are more prone to analog noise and thus there is around 2% difference in the two estimates. In future, the developed module will be integrated with the MFP-3D such that there is a digital transfer of the estimates thus eliminating the analog noise.

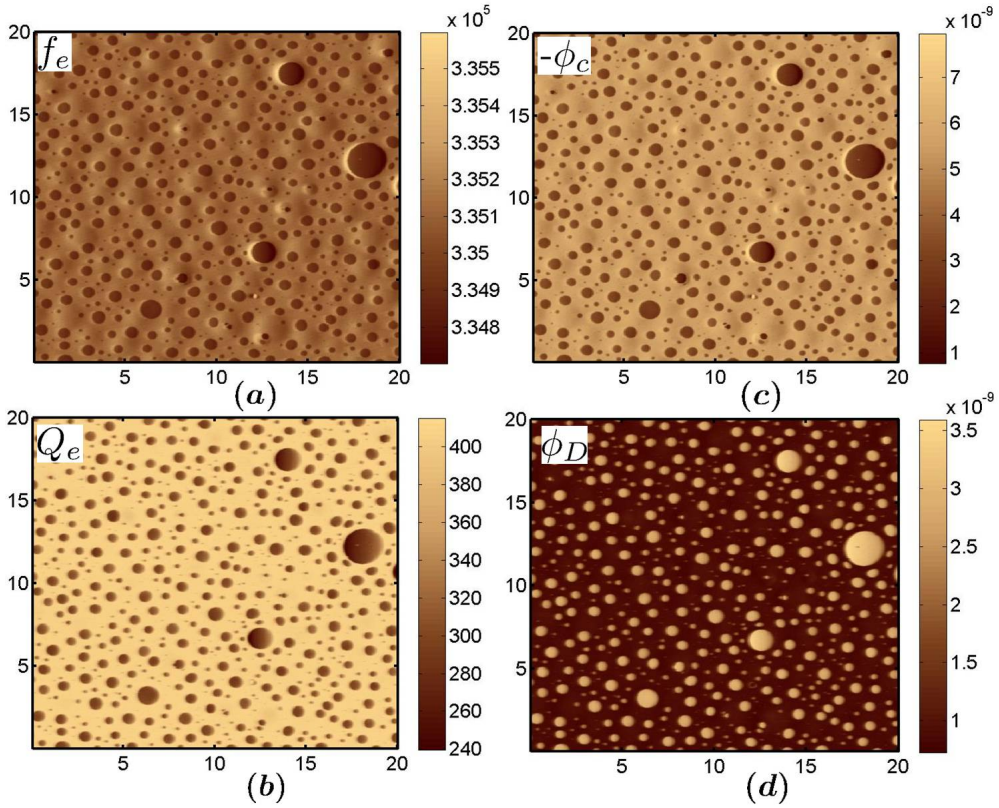

Figure 3.5: Figures (a) and (b) shows $20\mu m \times 20\mu m$ images of equivalent resonant frequency (f_e) and equivalent Quality factor (Q_e) of PBMA/PLMA polymer blend respectively. f_e, Q_e and amplitude image (shown in Figure 3.7 (b)) were used to determine $\overline{\Phi}_c$ (in N) and $\overline{\Phi}_D$ (in Joules). They are depicted in the figure (c) and (d) respectively.

Once the imaging was done, $\overline{\Phi}_c$ and $\overline{\Phi}_D$ images were directly obtained from f_e, Q_e and amplitude images using simple arithmetic of Eq.2.7. Figure 3.5 illustrates the results of a $20\mu m \times 20\mu m$ scan of a PBMA-PLMA polymer blend, where, Figures 3.5 (a), (b), (c) and (d) show images of f_e, Q_e, $\overline{\Phi}_c$ (-$\overline{\Phi}_c$ was plotted as the conservative force is negative) and $\overline{\Phi}_D$ respectively. Similar to the reporting in [30], three different types

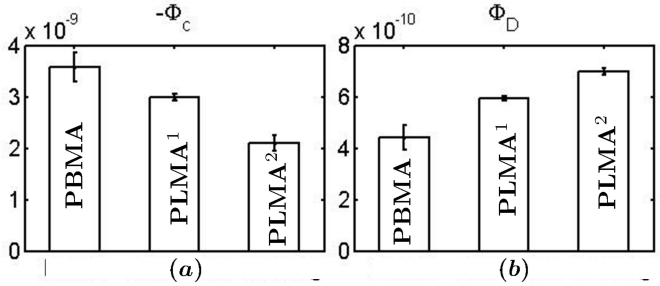

Figure 3.6: Figure shows mean a) $-\overline{\Phi}_c$ and b) $\overline{\Phi}_D$ of PBMA and PLMA polymers. 1st data point is for PBMA domains and 2nd and 3rd data points are for intermediate size and large size PLMA domains respectively. It is clear that both types of PLMA domains have lower stiffness and higher dissipation as compared to the smaller PBMA domains

of domains are observed. The small circular domains approximately $200nm$ in diameter are formed by the polymer PBMA. The intermediate circular domains (with diameter $\approx 500nm$) and the large circular domains (with diameter in the range $1\mu m$ to $4\mu m$) are formed by the polymer PLMA.

For the three polymer domains, an estimate of the average stiffness and dissipation values was determined from the $\overline{\Phi}_c$ and $\overline{\Phi}_d$ values at ten different locations of each domain. Figure 3.6 (a) and (b) plots the mean together with the standard deviation of $\overline{\Phi}_c$ and $\overline{\Phi}_d$ respectively for each of the three domains. Both types of PLMA domains showed higher dissipation than PBMA as seen from Figure 3.6(b), which is consistent with the observation in [30]. As evident from Figure 3.6(a), PLMA domains showed relatively lower contact stiffness compared to PBMA, which is expected as PLMA is rubbery at room temperature whereas PBMA is glassy. Unexpectedly, intermediate size PLMA domains show relatively higher stiffness. We speculate that the higher stiffness of the intermediate sized PLMA domains is due to sub-surface PBMA. We will investigate reasons for the unexpected higher stiffness of intermediate sized PLMA domains by using the real-time module to estimate stiffness for different levels of tip-sample interaction (different depths of tip-sample interaction can be achieved by altering the set-point amplitudes).

From these experiments, it is established that the developed module is able to provide real-time simultaneous estimates of stiffness and dissipation properties of the sample.

We remark that the traditional images of height, phase and amplitude can be simultaneously obtained together (shown in Figure 3.7) with the stiffness and dissipation images. Such a capability provides a rich source for researchers to interpret and discern material properties and to discern sources that lead to these properties.

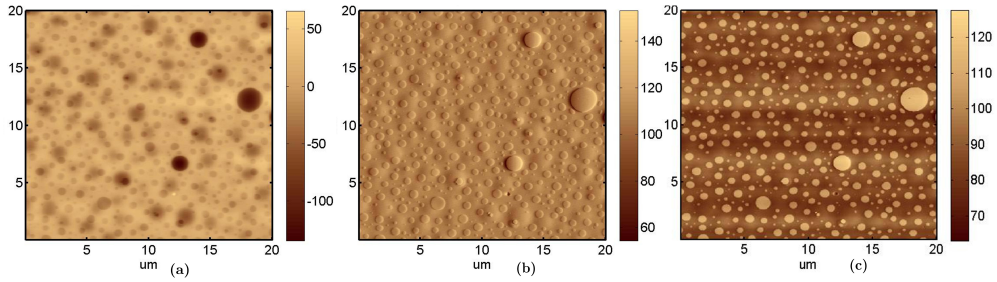

Figure 3.7: Figure shows a) Height (in nm) b) Amplitude (in nm) and c) Phase (in degrees) images of $20\mu m \times 20\mu m$ scan of PBMA/PLMA polymer blend respectively. These images were obtained simultaneously with the equivalent resonant frequency and equivalent quality factor images.

3.3 Conclusion

Recent capabilities of controlling matter at the nanoscale have led to new possibilities of achieving functionality of material with hitherto unparalleled specificity. Such a quest for designing material at nanoscale has provided renewed urgency for real-time methods for determining material properties at the nanoscale. Probe based instruments have the spatial resolution that is well-suited for nanoscale interrogation. However, currently there is a lack of methods for soft-matter investigation with temporal resolution compatible with real-time needs. In this chapter, we have reported a method for simultaneously determining elasticity, lossiness, and topography of material at the nanoscale in real-time in a dynamic mode operation of Atomic Force Microscopy, which renders it suitable for soft matter investigation. We have demonstrated the efficacy of the method which is implemented on a FPGA based hardware module for imaging a polymer blend. The preliminary study of the polymer blend illustrates the new found capabilities for soft-matter research made possible by the methods developed here. Moreover, recently

multiple mode of the cantilever flexure are being employed for nanoscale investigation. In the next chapter, we provide a framework (by determining contribution of different modes of the cantilever) for generalizing the methods developed here for such extension.

Chapter 4

On contribution and detection of higher eigenmodes during dynamic Atomic Force Microscopy

Dynamic mode operation of Atomic Force Microscopes relies on demodulation schemes to get information from different flexure modes of the cantilever while imaging a sample. In this chapter, we demonstrate that the conventional approach of discerning higher mode participation via amplitude and phase demodulation is not suitable for high bandwidth applications. Furthermore, we provide a method where the higher mode participation is reconstructed with high fidelity, and present a scheme for high bandwidth detection of higher modes when their participation becomes significant. These methods are shown to outperform the traditional amplitude-phase demodulation schemes in terms of speed, resolution and fidelity. The framework developed is tested on simulations and the method's utility for first two modes is demonstrated experimentally.

4.1 Introduction

In existing methods for quantifying the contribution of higher modes the cantilever deflection is demodulated at each mode's resonant frequency and the resulting amplitude and phase are used to quantify the contribution of modes. These methods extract the frequency content at or near modal frequency of higher modes and ignore the content of the cantilever deflection at frequencies away from the modal frequencies. Also, as amplitude and phase are slowly varying signals (when compared to the modal resonant frequencies), it can be particularly difficult to capture effect of higher modes in the transient and possibly short lived effects of sample on the cantilever deflection. In this chapter we show that the cantilever deflection can have appreciable content at frequencies away from the immediate vicinity of modal resonant frequencies and build a framework to extract such content in real-time. Apart from estimating the participation of higher modes in the cantilever deflection, we provide a high bandwidth method that detects when the higher mode participation is appreciable. Such a detection method is particularly suited for detecting short-lived and transient effects of higher mode participation. Methods built are shown to detect and quantify the contribution of first two modes experimentally.

In *intermittent-contact mode*, it is reasonable to assume that the mode shapes are dictated by the fixed-free boundary conditions. Here we assume the cantilever to be an unforced Euler-Bernoulli beam with one end fixed (at $x = 0$) and another end free (at $x = L$). We also assume that external excitation to the cantilever is provided as a forcing $g(t)$ and the tip sample interaction forcing is given by $\Phi(p, \dot{p})$ at $x = L$ (tip position) where $p(t) := w(L, t)$. Assuming an N mode approximation, with the j^{th} mode shape being $\psi_j(x)$, it can be shown using variational principles[4] that $w(x, t) = \sum_{j=1}^{N} \psi_j(x) q_j(t)$ with each $q_j(t)$ satisfying

$$\frac{\ddot{q_j}}{\omega_j^2} + \frac{\dot{q_j}}{\omega_j Q_j} + q_j = \frac{g_j(t) + \eta_j(t)}{k_j} + \frac{\Phi_j(p, \dot{p})}{k_j} \tag{4.1}$$

where $g_j(t) = \psi_j(L) g(t)$, $\Phi_j(p, \dot{p}) = \psi_j(L)\Phi(p, \dot{p})$, $\eta_j(t)$ is the forcing on the jth mode due to thermal noise; and ω_j, k_j and Q_j are jth mode's resonant frequency, spring constant and quality factor respectively. Each instance of Eq.4.1 is a second order ordinary differential equation with external forcing, $f_j := \psi_j(L)(g(t) + \Phi(p, \dot{p}))$, and can

be recast as,

$$\begin{aligned}
\begin{bmatrix} \dot{x}_{1j} \\ x_{2j} \end{bmatrix} &= \overbrace{\begin{bmatrix} 0 & 1 \\ -\omega_j^2 & -\frac{\omega_j}{Q_j} \end{bmatrix}}^{A_j} \begin{bmatrix} x_{1j} \\ x_{2j} \end{bmatrix} + \overbrace{\begin{bmatrix} 0 \\ \frac{\omega_j^2}{k_j} \end{bmatrix}}^{B_j} (f_j + \eta_j) \\
y_j &= \overbrace{\psi_j(L) \begin{bmatrix} 1 & 0 \end{bmatrix}}^{C_j} \begin{bmatrix} x_{1j} \\ x_{2j} \end{bmatrix}
\end{aligned} \tag{4.2}$$

where state x_{1j} and state x_{2j} denotes the cantilever's jth-mode position and velocity respectively; and $y_j = \psi_j(L) q_j$ is the contribution of the jth-mode to the cantilever tip deflection p, where $p = \sum_{j=1}^{N} y_j$. Let $B_j^L = B_j \psi_j(L)$, then Eq.4.2 can be written as

$$\begin{aligned}
\dot{x_j} &= A_j x_j + B_j^L \left(g(t) + \Phi(p, \dot{p}) \right) + B_j \eta_j(t) \\
y_j &= C_j x_j
\end{aligned} \tag{4.3}$$

where $x_j = \begin{bmatrix} x_{1j} & x_{2j} \end{bmatrix}'$. The model in Eq.4.3 can be identified via frequency sweep methods or using thermal noise response near each mode's resonance. This model can be discretized and represented as

$$\begin{aligned}
x_j(k+1) &= F_j x_j(k) + G_j^L \left(g(k) + \Phi(p, \dot{p}) \right) + G_j \eta_j(k) \\
y_j(k) &= H_j x_j(k).
\end{aligned} \tag{4.4}$$

With $x(k) := \begin{bmatrix} x_1(k) & x_2(k) & \dots & x_N(k) \end{bmatrix}'$, Eq.4.4 for each value of $j = 1, 2, \dots, N$ can be combined and written as,

$$\begin{aligned}
x(k+1) &= \underbrace{\begin{bmatrix} F_1 & \dots & 0 \\ 0 & \ddots & 0 \\ 0 & 0 & F_N \end{bmatrix}}_{F} x(k) + \underbrace{\begin{bmatrix} G_1^L \\ \vdots \\ G_N^L \end{bmatrix}}_{G^L} (g(k) \\
&\quad + \Phi(p, \dot{p})) + \underbrace{\begin{bmatrix} G_1 & \dots & 0 \\ 0 & \ddots & 0 \\ 0 & 0 & G_N \end{bmatrix}}_{G} \underbrace{\begin{bmatrix} \eta_1(k) \\ \vdots \\ \eta_N(k) \end{bmatrix}}_{\eta(k)} \\
y(k) &= \underbrace{\begin{bmatrix} H_1 & \dots & H_N \end{bmatrix}}_{H} x(k) + \nu(k).
\end{aligned} \tag{4.5}$$

Here, all η_j's are independent and Gaussian. Let the covariance matrix of the thermal noise vector η be given by $E(\eta\eta^*) = S$. Also ν characterizes the measurement (photodiode) noise with covariance $E(\nu\nu^*) = R$.

The multi-mode model of the cantilever described above in Eq.4.5 was used to study the first two flexure modes of an Olympus AC240 (Product Id# OMCL- AC240TS) cantilever. The multi-mode cantilever dynamics was identified experimentally using the frequency sweep method where the first mode resonant frequency was determined to be at 75.8 kHz and second mode resonant frequency at 457.6 kHz. The cantilever and its interaction with sample was simulated, where, a piece-wise linear model [25] of the tip-sample interaction was assumed. Here the cantilever was excited at its first resonance frequency, with a free-air (when there is no sample) amplitude of 200nm. Each mode's contribution (y_j) to the cantilever deflection was analyzed. Figure 4.1 compares the power spectrum of the second mode signal y_2 when the cantilever is interacting with the sample of height 30nm to when it oscillating freely (free-air). It is evident from Figure 4.1 that in the absence of the sample, only the modal frequencies have appreciable impact on the cantilever deflection. Here, the first peak in the spectrum of the deflection measurement is caused primarily by the forcing whereas the second peak is a result of the thermal noise. In the presence of the sample, the nonlinear interaction spreads the energy being injected at the first resonant frequency into many harmonics of the forcing. Moreover, the sixth harmonic resonates with the second modal frequency of the cantilever resulting in an appreciable peak near the second modal frequency. We remark that apart from the sixth harmonic of the forcing frequency, other harmonics also get a boost due to the way the entire frequency response of the two-mode model of the cantilever amplifies the harmonics. In a typical schemed based on demodulation near modal frequencies these other harmonics get ignored where possibly important information is lost. Furthermore, here the role played by the second and the first modes cannot be clearly delineated.

Indeed, it is worth mentioning here that for a higher mode extension of the multi-frequency excitation (like such used by Agarwal et al. [10]), it is essential to obtain the entire trajectory of each mode. As alluded to earlier, all modes contribute to the total gain for each harmonics and thus a simple demodulation scheme at each of the harmonic can not be used to separate the cantilever deflection signal into each mode's contribution.

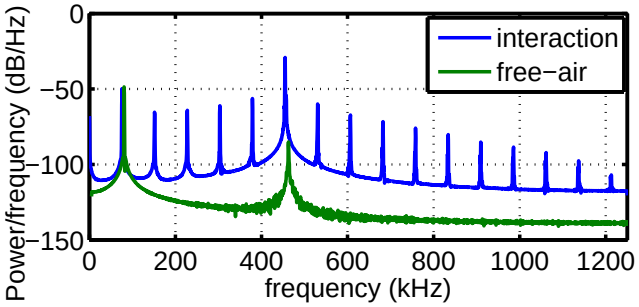

Figure 4.1: Simulation results showing cantilever 2^{nd}-mode power spectrum before and after interaction with a sample of height 30nm. Free-air curve is shifted right by 5kHz to highlight the difference in peaks.

Amplitude-phase demodulation schemes thus fall short for such operations. In the next section, an observer based framework is presented to address these challenges.

4.2 Multimode Observer

In a typical multimode operation of the dynamic mode, lock-in amplifiers are used to extract the amplitude of each mode from the measured tip deflection. We propose observer based state-detection scheme that has the capability of incorporating effects away from the modal frequency. We subsequently develop a fast detection method of higher mode participation in the measured deflection signal. The proposed scheme relies on the construction of a dynamic Kalman observer for linear system of Eq.4.5 that provides an estimate, $\hat{x}(k+1)$ of the state x of the cantilever, depending on all the observations till time step k, and is given by,

$$\begin{aligned} \hat{x}(k+1) = \; & F\hat{x}(k) + \overbrace{FP_kH'(HP_kH'+R)^{-1}}^{L_k} \\ & [y(k) - \hat{y}(k)] + G^L g(k) \\ \hat{y}(k) = \; & H\hat{x}(k) \\ P_{k+1} = \; & F[I - P_kH'\left(HP_kH'+R\right)^{-1}H] \\ & P_kF' + GSG' \end{aligned} \tag{4.6}$$

with $\hat{x}(0) = 0$ and the *error covariance* $P_k := Cov(x(k) - \hat{x}(k))$ initialized by a large number P_0, depending on actual state values. The observer (Eq.4.6) mimics the dynamics of the cantilever (Eq.4.5) and utilizes a correcting term $L_k e$ where L_k is the observer gain and $e := H\tilde{x} := H(x - \hat{x})$ is called the error innovation (difference between estimated and actual output). The error dynamics in absence of tip-sample interaction is given by,

$$\tilde{x}(k+1) = (F - L_k H)\tilde{x}(k) + G\eta(k) - L_k\nu(k). \tag{4.7}$$

Due to low measurement noise, it is possible to choose L_k[31], such that the real part of the eigenvalues of $(F - L_k H)$ can have large negative value and thus $\tilde{x}$ goes to zero fast in absence of noise. Also the estimate of the contribution of the j-th mode , $\hat{y}_j$ can be obtained via

$$\hat{y}_j(k) = \underbrace{\begin{bmatrix} 0 & \dots & H_j & \dots & 0 \end{bmatrix}}_{\text{only } j\text{-th element non-zero}} \hat{x}(k). \tag{4.8}$$

With further analysis of the observer, it was found that the error covariance P_k reaches a constant value fast (depending on the noise covariances). Here the dynamic Kalman observer behaves as a steady-state observer where the cantilever behavior in the past over a long time horizon has undue influence on the estimation of the current state of the cantilever. During dynamic AFM operation, when tip-sample interaction length changes suddenly there is a significant error in estimation if the steady-state Kalman gain is used. This suggests that filter gains should be suitably altered for fast tracking. To address the above issue, we employ a receding horizon Kalman[32] (RHK) observer which provides an estimate $\hat{x}_{rh}(k)$ of the state $x(k)$ based on the past M photodiode measurements and ignoring the rest of the measurement history. The value of M is suitably chosen to balance the effect of noise and the responsiveness of the estimation to fast changes in the state. Dynamics of the RHK observer is given by Eq.4.6, but for each time-instant k, $\hat{x}_{rh}(k)$ is estimated by following the dynamics of Eq.4.6 initialized at $(k-M)^{th}$ instance as $\hat{x}_{rh}(k-M) = 0$ and $P_{k-M} = P_0$. The designed RHK observer results in observer gains that adapt to sudden tip-sample interactions and is thus able to track changes in the state of the cantilever faster than the steady-state observer.

To demonstrate the utility of the observer, simulations were performed using the setup given in the previous section. Cantilever model was excited at its first resonance

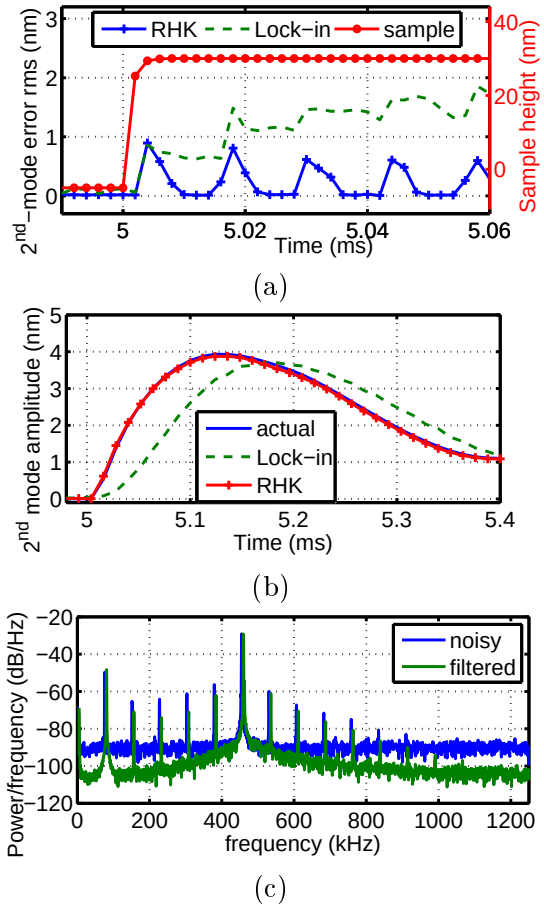

Figure 4.2: Simulation results showing cantilever 2^{nd}-mode response for a step change in sample height. (a) Rms of error between Actual and estimated 2^{nd}-mode trajectories, by both amplitude-phase demodulation using lock-in amp (green) and RHK observer (blue). Sample height is changed from no-interaction (shown with negative value) to an interaction of 30nm at the time instant of 5s. The RHK observer is able to track the 2^{nd}-mode trajectory in less than 0.01ms after every tip-sample interaction, and thus has a tracking bandwidth of more than 100kHz. (b) 2^{nd}-mode amplitude demodulated from y_2 (without any measurement noise, blue), RHK observer estimate $\hat{y}_2$ (red) and y (combined cantilever deflection, green). Amplitude demodulated from RHK observer overlaps with the actual contribution. Rise time of actual amplitude is ≈ 0.12ms whereas the rise time of lock-in amplitude is $\approx$ 0.18ms. (c) Power spectrum for the noisy measurement of the 2^{nd}-mode contribution and its estimate.

frequency, with a free-air amplitude of 200nm and a step of 30nm was given to the sample height. Trajectories of the second mode were reconstructed using both amplitude-phase demodulation of the cantilever deflection (using lock-in amplifier) and via two types of observers; steady-state and the RHK observer. M was chosen to be 10 for this simulation. The RHK observer performed better than the steady-state observer and thus only results obtained using the RHK observer are presented here. Figure 4.2(a) plots the root-mean-square (rms) error between actual trajectory y_2 of the cantilever and with those reconstructed via RHK observer (RHK) and via amplitude-phase demodulation (Lock-In). It is evident that after each tip-sample interaction (one cycle of excitation frequency), error in trajectory estimated via observer reduces to zero fast (within a couple of cycles of second mode resonant frequency) whereas the trajectory constructed using Lock-in is not able to capture the transients and results in an increasing error till transients die out. We remark that often[12], the effect on the second mode can be limited to the transient part of the response and thus it is possible in such cases that the entire signature of the sample's influence on the second mode cannot be accurately tracked using demodulation based schemes. It is also evident that the demodulation scheme is not able to capture the actual $2^{nd}-$mode trajectory with high fidelity as there is no tracking for the time the appreciable second mode contribution is present. Figure 4.2(c) shows the power spectrum of $(y_2 + \nu)$ and the estimate $\hat{y}_2$. The observer is able to filter the noise with more than 20 dB per decade attenuation before 600 kHz, while keeping the peaks at the 1^{st} and 2^{nd} modal frequencies intact. Peaks at the harmonics of the excitation frequency are also present but slightly attenuated. These peaks are ignored and lost when using demodulation. As the noise in the estimated $\hat{y}_2$ is significantly reduced, demodulation of $\hat{y}_2$ at the second modal frequency can have much higher bandwidth which is not possible for direct demodulation of the measured noisy cantilever deflection. Figure 4.2(b) shows the 2^{nd}-mode demodulated amplitudes where the one estimated from RHK observer (termed as RHK amplitude) is overlapping the actual 2^{nd}-mode amplitude. It is clear from these simulations that the RHK observer is able to track the $2^{nd}-$mode contribution within 2-3 cycles of second mode resonant frequency, which can be translated into a tracking bandwidth of more than 100 kHz. This is an *order of magnitude improvement* compared to amplitude-phase demodulation based methods (typical bandwidth of no more than 10kHz).

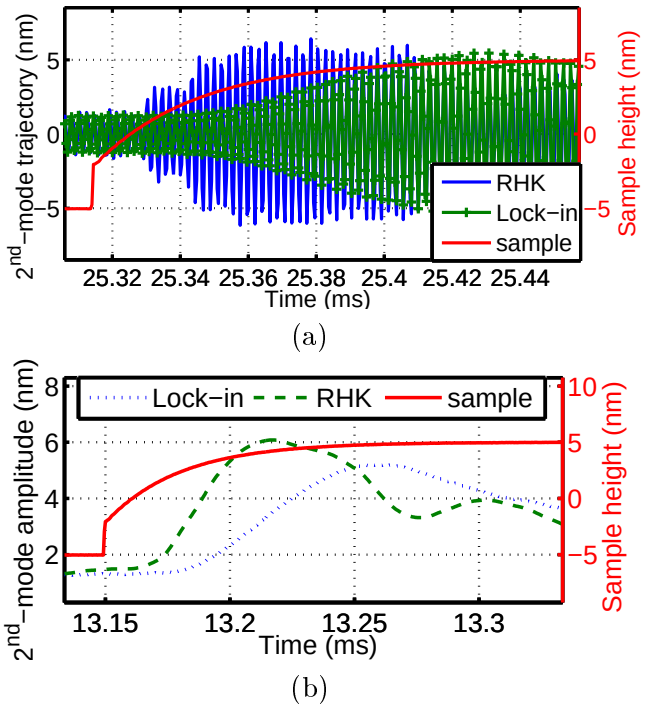

Figure 4.3: Experimental result for a 10 nm step change in sample height. (a) 2^{nd} mode trajectory estimated via Kalman observer compared with that evaluated by Lock-In amplifiers. (b) 2^{nd} mode amplitudes demodulated from trajectory estimated via Kalman observer (RHK) compared with that evaluated by demodulation of the cantilever deflection (Lock-in). Rise time of RHK amplitude is $\approx$ 0.05ms whereas the rise time of lock-in amplitude is $\approx$ 0.1ms which is of similar order to as observe in simulation.

The advantages of observer based reconstruction of second mode trajectories are further demonstrated by experiments using an Olympus AC240 cantilever for the dynamic mode imaging on Mica. Here the setpoint amplitude was 203nm with free-air amplitude being 240nm. Parameters of the cantilever, characterized for the first two modes are:

- k_1 =1.72 N/m, ω_1 =151.6π rad/s, Q_1 =168, ω_2 =915.2π rad/s and Q_2 =478.

Freshly cleaved Mica sample was attached to a small piezoscanner and square pulses of various amplitude and frequencies were applied to the piezoscanner. Each pulse applied to the piezo moved the mica sample up and down and generated a square sample profile of height 10nm. A feedback loop on z-axis with very low controller gains was used to cancel any drift. Deflection and dither forcing signals were captured and sampled at 2.5

MHz and were analyzed offline. Trajectory of $2^{nd}-$ mode was estimated using the RHK observer (shown in Fig 4.3(a)) and the demodulated amplitude is plotted in Figure 4.3 (b) along with the direct demodulation of the measured deflection signal. Here the actual $2^{nd}-$mode trajectory is not known and thus rms error plot of Figure 4.2(a) can not be plotted. However similar to the simulation result from Figure 4.2(b), the amplitude demodulated from the estimated $\hat{y}_2$ has a faster response, with a rise time approximately half of the Lock-in based amplitude.

4.3 Faster Detection of higher modes

In the previous section we have provided a method that reconstructs the relative modal participation of an AFM cantilever using observers and have demonstrated that significant gains can be accrued in the fidelity and bandwidth of higher model participation. Further gains can result if the purpose is to simply *detect* if higher mode participation is significant or not without emphasizing its magnitude. To enable faster detection of higher modes, we model the tip-sample interaction as a force that possibly appears every cycle of the cantilever oscillation. The interaction is short-lived, and is appreciable only when the cantilever is near the sample-surface. Assuming an impulsive force as a model for the short-lived force (which is valid when compared to the entire trajectory of the cantilevers orbit), we can model the dynamics as given by[33, 34],

$$x(k+1) = Fx(k) + G_1 g(k) + G\eta(k) + \delta_{\theta,k+1}\upsilon \tag{4.9}$$

where $\delta_{l,k}$ denotes the dirac delta function, θ is the time-instance of the impact (a *hit*) and $\upsilon = [\upsilon_1 \dots \upsilon_N]'$ is the magnitude of impact, measured in the amount of change in the state of each respective mode. In this case, error e for steady state observer with gain $L = [L_1 \dots L_N]'$ is given by,

$$e(k) = \sum_{j=1}^{N} \Gamma_j(\theta, k)\upsilon_j + e_0(k) \tag{4.10}$$

where

$$\Gamma_j(\theta, k) = [H_j(F_j - L_j H_j) \dots H_j(F_j - L_j H_j)^{k-\theta}]'. \tag{4.11}$$

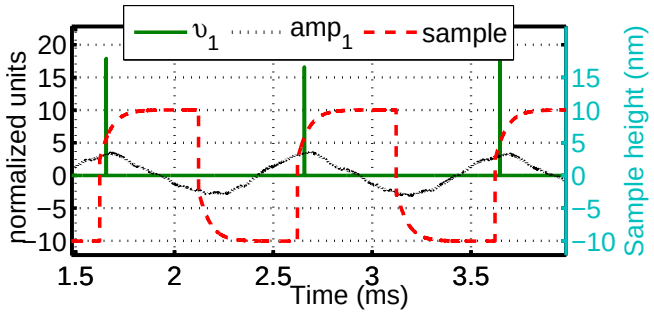

(a)

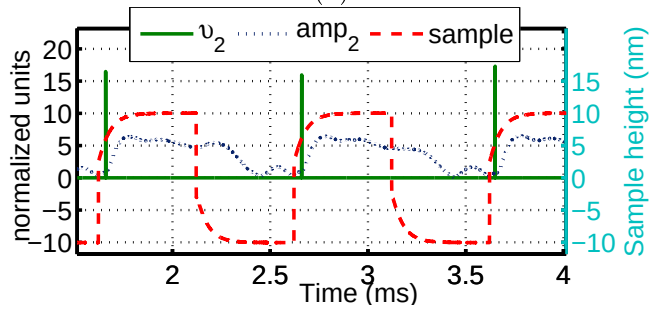

(b)

Figure 4.4: Experimental result for higher mode detection. A square pulse of 20nm and 1kHz frequency was given to the sample height. (a) shows sample height overlaid on the 1st mode amplitude (blue) and the detected 'hits'. Green curve peaks are the local maxima of υ_1 identifying the time of impact and also quantifying the effect of impact on the 1^{st}-mode. (b) shows the local maxima of υ_2 with second mode amplitude overlaid.

Assuming each dynamic profile Γ_j can be approximated by M_1 samples with $\overline{\Gamma}_j = \Gamma_j(k - M_1, k)$, $\overline{e}(k) = [e(k); \ldots; e(k - M_1 - 1)]$, and $\overline{e}_0(k) = [e_0(k); \ldots; e_0(k - M_1 - 1)]$, Eq.4.10 can be written as

$$\overline{e}(k) = \underbrace{[\overline{\Gamma}_1 \ldots \overline{\Gamma}_N]}_{\Gamma_{eq}} \begin{bmatrix} \upsilon_1 \\ \vdots \\ \upsilon_N \end{bmatrix} + \overline{e}_0(k). \tag{4.12}$$

For Kalman observer, as $\overline{e}_0(k)$ is *white noise* [35], the impact of tip-sample interaction

v can be estimated by a *linear unbiased estimator*[36] given by,

$$\begin{bmatrix} v_1 \\ \vdots \\ v_N \end{bmatrix} = \left(\Gamma'_{eq}\Gamma_{eq}\right)^{-1}\Gamma'_{eq}\overline{e}(k). \tag{4.13}$$

Experiments were performed on the experimental setup of previous section where a sample with a square profile of 20nm was imaged. The Kalman observer was used to obtain the *innovation* signal and the v_1 and v_2 were found using Eq.4.13. Figure 4.4 (a) and (b) plots the time of impact for 1st two modes and there normalized value along with the respective amplitudes and the sample height. Both modes are detected within two to three cycles of exciting frequency. As excitation is near the first mode, the detection bandwidth of detector is from half to third of the first modal frequency translating into a detection bandwidth of $\approx$ 20kHz. The natural bandwidth of $j-$th mode of the cantilever is bounded by $\beta_j := (\omega_j/Q_j)$ which is considerably small for first few modes ($\beta_1 \approx 350$Hz and $\beta_2 \approx 955$Hz for the used cantilever). Thus the detection method developed here is able to improve speed of detection of first two modes by ≈ 20 times.

Chapter 5

Real-time study of mechanical/physical properties of soft-matter in liquid environment under dynamic mode AFM

5.1 Introduction

REEP algorithm has the potential to quantify the mechanical properties of the soft-samples in liquid operation. In order to study different material properties like elasticity and dissipation using dynamic AFM, it is important to obtain a well characterized ac response of the cantilever. In air, acoustic excitation of cantilever using a piezoelectric transducer and then doing frequency sweep of the input is able to provide accurate measurement of the ac response of the cantilever. But in the under liquid operation of the dynamic AFM, acoustic excitation results in unnecessary excitation of the surrounding liquid layers. This results in a 'forest of peak' phenomenon where the mechanical response of the fluid structure superimpose the actual ac response of the cantilever. To overcome this limitation, various methods have been proposed and adopted. Most widely used method involve coating the cantilever with a magnetic material and then using time varying magnetic field to apply force directly to the cantilever thus not

disturbing the surrounding liquid. Another method which was reported recently, photothermal excitation, uses an intensity-modulated laser for exciting the cantilever. This method is also able to eliminate the undue disturbances of the surrounding liquid but it is difficult to characterize the frequency response as the thermal expansion and heating can have complex frequency dependence. Thus for application of REEP algorithm, we chose magnetic excitation as our source of cantilever forcing.

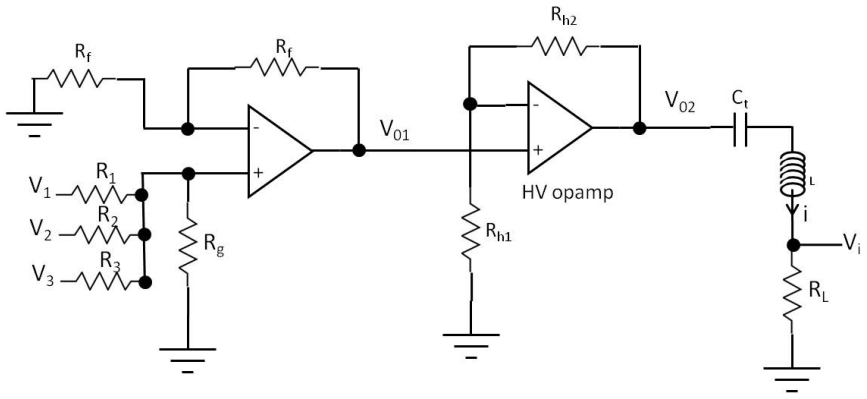

Figure 5.1: Schematic showing the solenoid and the operational amplifiers. HV opamp amplifier has a gain of 10, where as the first amplifier is a summer circuit with appropriate gains.

5.2 Methods

The force F and torque τ exerted on a magnetic dipole m in presence of a magnetic field of strength B is given by $F = \nabla(B.m)$ and $\tau = B \times m$ respectively. Deflection of the cantilever is caused by a combined effect of both the force and the torque. We use a solenoid with a Ferrite core to create the modulating magnetic field required. The diameter of the core is chosen to be small (1.5mm) to reduce the inductive load, as inductance is proportional to the area of the core. Length of the core is 15mm. A copper wire of diameter 0.51mm is wound around the core with 40 turns. The inductance of the solenoid is $20\mu H$. For excitation frequency range of 20 KHz to 100 kHz, the impedance of the solenoid varies from 2.5Ω to 12.5Ω. A high voltage/high current operation amplifier (OPA 547 from Texas Instrument) is used to drive the electromagnet as large current is required for substantial deflection of the cantilever (tens of nm). Figure 5.1 shows

the block diagram of the configuration and we can see that the excitation is a weighted sum of three sinusoids which is required for the application of the REEP algorithm. A capacitor is included in series with the solenoid for the ac coupling. Second amplifier in the circuit has a gain of 10, such that the output voltage swing is around ± 10 V.

Force on the cantilever is directly proportional to the strength of the magnetic field and magnetic field generated by solenoid is directly proportional to the current flowing through the coil. From Figure 5.1, we can see that the current through the solenoid is given by, $i = V_i/R_L$. So to characterize the cantilever frequency response, it suffices to estimate the transfer function from V_i to the deflection of the cantilever. We use a 18Ω resistor for R_L. Thus the total load impedance varies from 20.5Ω to 30.5Ω. This relates to the maximum current amplitude to be 500 mA which is well below the current rating of the wire used for the solenoid.

As the strength of magnetic field of a solenoid decreases drastically with the distance from the core, solenoid is placed right below the sample so that cantilever can be as close to the solenoid as possible (Figure 5.2 (a)). A laminate plate is used as a sample holder with solenoid glued at the center. For portability, plate is held tight to the x-y piezoscanner by using magnets and can be removed or attached conveniently. Further, plate is laterally moved in x-y direction to find the position of the maximum magnetic force, that is where maximum amplitude of the cantilever deflection is. Once the spot is found, magnets keep the plate in position. Figure 5.2 (b) depicts the entire setup where the developed hardware is integrated with a commercial AFM (Asylum Research MFP-3D). Magnetic cantilevers from Agilent are used for all the experiments. These are silicon cantilevers having silicon tips with a thin magnetic coating on the back side.

5.3 Frequency Response

To demonstrate the efficacy of the developed hardware, it was used to obtain the frequency response of the magnetic cantilevers. First experiment was performed in air where the cantilever was excited with both magnetic and acoustic excitation. Agilent MAClever of Type I is used for this experiment. There are three different rectangular AFM cantilevers on each TYPE I chip with nominal resonant frequency (in air) of 105, 155 and 75 kHz and the nominal spring constants of 0.95, 1.75 and 0.6 N/m respectively.

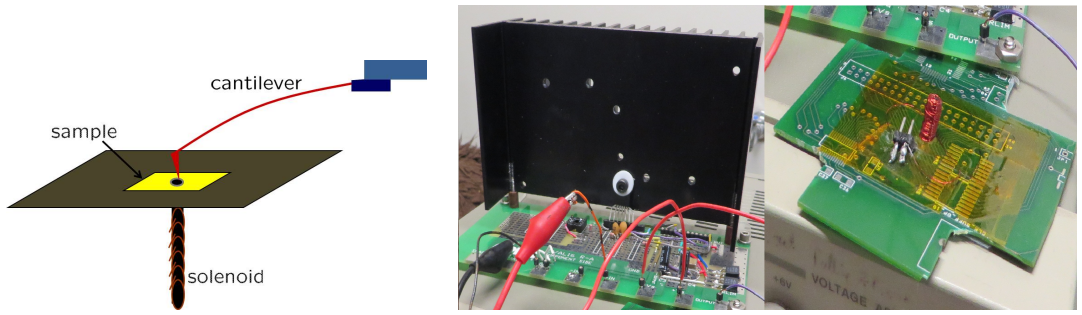

(a) (b)

Figure 5.2: (a) shows a diagram of solenoid plate with the sample and cantilever on top of it. As magnetic field is inversely proportional to the square of the distance between cantilever and solenoid, solenoid is placed directly below to maximize the magnetic force. (b) is an actual image of the developed hardware. Left is the power opamp with proper heat sinking and left is the upside down sample plate with the solenoid in the middle.

Magnetic cantilever used has a resonant frequency of 82.3 kHz, quality factor of 100 and spring constant of 1.14 N/m when measured in air. Figure 5.3 (a) shows the normalized amplitude of the magnetic and acoustic excitation compared with a simple harmonic oscillator (SHO) fit to the thermal response of the cantilever. It is clear that the three match well for this case. Figure 5.3 (b) plots the phase of the acoustic and magnetic excitation. Here, the phase of acoustic excitation varies from -22° to 183°, whereas the phase of the magnetic excitation varies from 11° to 168° which is closer to the SHO fit (0° to 180°). Thus even in air, magnetic excitation is closer to the actual AC response of the cantilever.

Second set of experiment is done in distilled water. A catenoid like surface of water is formed between the cantilever holder and a mica disk, using the surface tension of the water, completely submerging the cantilever. Again cantilever is excited with both magnetic and acoustic excitation. Figure 5.3 (c) shows the normalized amplitude of the magnetic and acoustic excitation compared with a simple harmonic oscillator (SHO) fit to the thermal response of the cantilever in distilled water. In this case, acoustic excitation is completely erratic and consists of various different components and not at all reflects the actual ac response of the cantilever (which follows the thermal response of the cantilever). Magnetic excitation is able to much better approximate the ac response and thus provides a tool to correctly characterize the ac response of the cantilever in liquid. Figure 5.3 (d) plots the phase of the acoustic and magnetic excitation. Here also

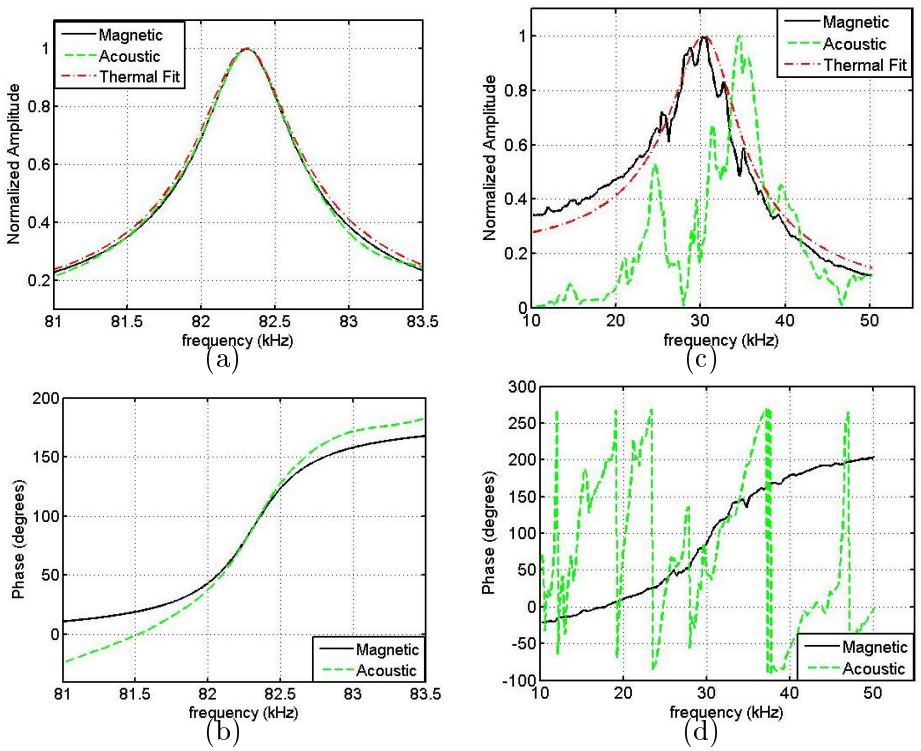

Figure 5.3: (a) plots the normalized amplitude for both magnetic and acoustic excitation compared with the normalized SHO fit to the thermal response of the cantilever in air. (c) plots the same for the case of in water operation. These are all off-sample. (b) and (d) plots the phase for two excitations (acoustic and magnetic) in both cases, in air and in water operations.

the phase is close to the phase of the SHO fit (0° to 180°).

5.4 Parameter Estimation

Once we have established accurate ac excitation of cantilever, we implement the REEP algorithm. Cantilever is excited with a sum of three sinusoids. Magnetic excitation is first used for REEP imaging in air. Magnetic cantilever is characterized off-sample and approach-retract curves are performed on a Mica sample. The observed deflection is sampled along with the voltage V_i across the resistor R_L (as discussed earlier, this is the forcing). REEP algorithm is run off-line over the data and the estimated equivalent resonant frequency and equivalent quality factor (f_e and Q_e) versus the instantaneous

amplitude is plotted in Figure 5.4 (a) and (b) respectively. It can be seen that the off-sample equivalent resonant frequency and equivalent quality factor estimated by REEP algorithm (values at the maximum amplitude in the Figure 5.4 (a) and (b)) matches well with the values obtained from ac characterization. Deflection signal was demodulated to obtain instantaneous amplitude and phase at the central frequency of excitation, which were used, along with the estimated parameters, to calculate the energy dissipated using REEP as well as via analytical means([1]) which matches well as seen from the Figure 5.4 (c).

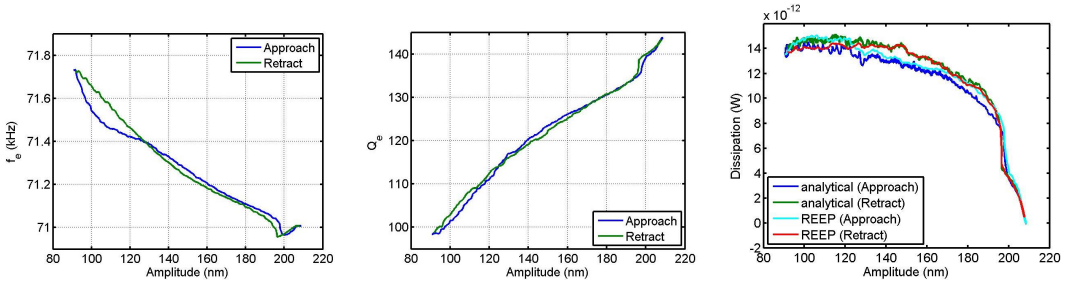

(a) (b) (c)

Figure 5.4: Figure shows the (a) equivalent resonant frequency and (b) equivalent quality factor during an approach retract cycle of dynamic AFM on a Mica sample in air. (c) plots the energy dissipated calculated using both REEP and the analytical means. For both approach and retract, REEP estimates are able to accurately measure the energy dissipated.

The real utility of REEP in the under liquid operation is the ability to actually quantify the physical properties of biological sample in there native environment. To demonstrate this, we study the physical properties of a Microtubule sample in a buffer solution. Microtubules (MT) are formed by polymerization of tubulin dimers and are directed linear lattices responsible for intracellular transport. A stable MT sample was prepped and 10ml of the sample was put on a freshly cleaved Mica and left for 5 mins. Next, REEP experiments are performed on this sample. Here, as mentioned earlier, a catenoid surface is formed and cantilever is slowly brought closer to the Mica surface for imaging. Again, magnetic cantilever is characterized off-sample and approach-retract curves are performed with the deflection and forcing sampled. The cantilever parameters obtained from ac characterization are resonant frequency of 27.32 kHz, quality factor of 3.1. In liquid, as the quality factor of a cantilever is significantly reduced, the amplitude of the side band sinusoids is chosen to be very low so to keep the amplitude

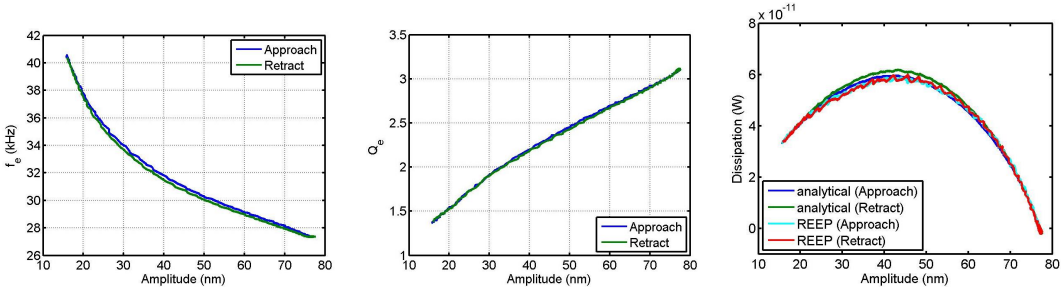

Figure 5.5: Figure shows the (a) equivalent resonant frequency and (b) equivalent quality factor during an approach retract cycle on a MT sample in buffer solution. (c) plots the energy dissipated calculated using both REEP and the analytical means. Even under liquid operation, REEP estimates are able to accurately measure the energy dissipated.

modulation to a minimum along with the robust estimation. The estimated equivalent resonant frequency and equivalent quality factor are plotted in Figure 5.5 (a) and (b) respectively. Again, the off-sample equivalent resonant frequency and equivalent quality factor estimated by REEP algorithm matches well with the values obtained from ac characterization. The estimated power dissipated obtained using REEP as well as analytical means([1]) is plotted in Figure 5.5 (c). It is clearly visible that parameters estimated using REEP in liquid are able to accurately quantify the dissipated power even under liquid operation.

5.5 REEP Imaging

Experiments were performed on the MT sample with MFP-3D. The FPGA module developed for the REEP algorithm to estimate the equivalent parameters in real-time was used to provide the images of local stiffness and local dissipation of the sample. The data acquisition channels of MFP-3D were used to save the two real-time estimated parameters along with instantaneous height, amplitude and phase. The stiffness and dissipation images were obtained from the estimated equivalent resonant frequency, quality factor and the amplitude of the central harmonic. Figure 5.6 plots the result of a $3\mu m \times 3\mu m$ scan of the MT sample. Microtubules were seen to be as long as 10 microns in length. Figure 5.6 (a) and (b) plots the estimated equivalent parameters, while (c) and (d) plot $-\phi_c$ and ϕ_D to characterize the stiffness and dissipation properties

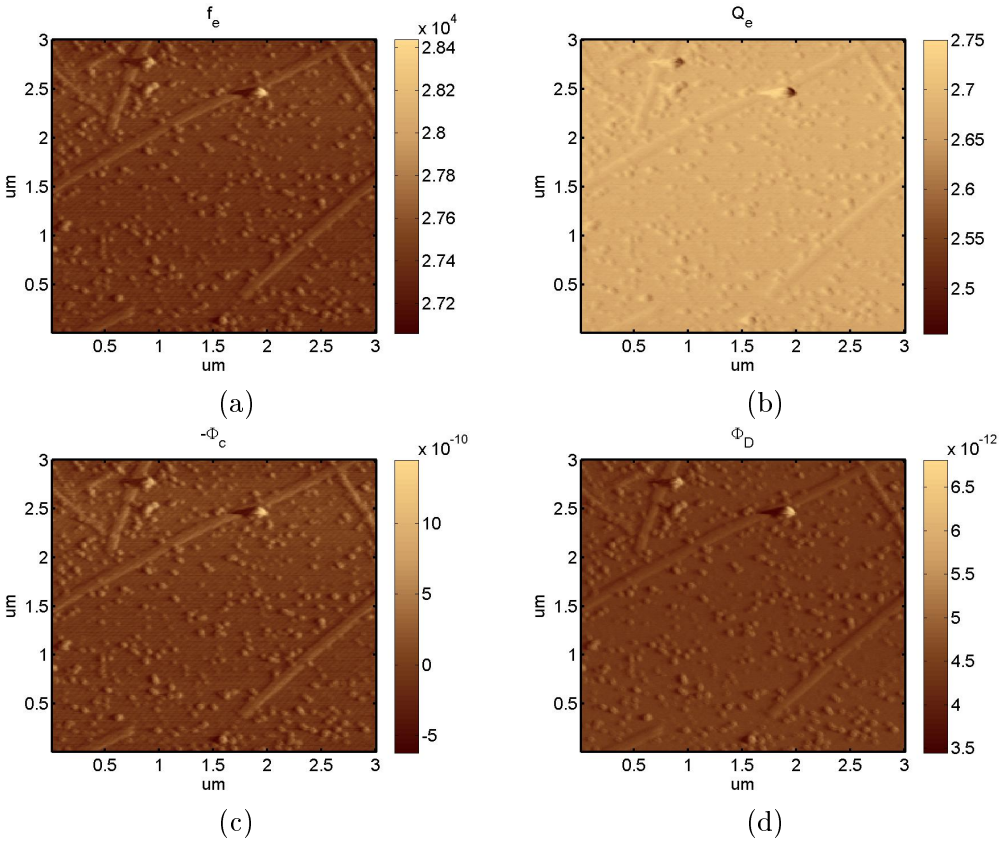

Figure 5.6: Results of a $3\mu m \times 3\mu m$ scan of the MT sample (a) plots the equivalent resonant frequency in Hz and (b) plots the equivalent quality factor. (c) plots the stiffness (-ϕ_c) estimate of the sample while (d) plots the energy dissipated by the tip-sample interaction.

of the MTs. The small particles visible on the images are depolymerized MTs. MTs have a diameter of about $25nm$ but the width of the MTs is seen here to be $50 - 60nm$ and a very low height of around $5nm$. This is because of the forces exerted by the cantilever. As the cantilever presses on the MTs, they are flattened out. It is clear from Figure 5.6 (c) and (d) that MTs have higher stiffness and lower dissipation compared to the Mica. The stiffness of the MTs have been shown to be dependent on different conditions that affect the stability of MTs against depolymerization[37]. Further study of different mutants of MTs with changing condition will give insights into the variability of stiffness caused by these conditions.

From these experiments, it is demonstrated that the developed hardware is able to accurately resonate the cantilever under liquid. These experiments also verify the

applicability of REEP algorithm under liquid operation.

5.6 Conclusion and Discussion

There is a scarcity of real-time methods to quantify the mechanical properties of soft-sample (like bio molecules) in there native environment. In this chapter, we have reported a method to simultaneously characterize the stiffness and dissipation properties of samples under liquid environment during dynamic mode AFM. A solenoid based hardware module is developed to magnetically excite the cantilever without exciting the surrounding liquid layers. This is also required to accurately measure the ac response of the cantilever. Then the REEP algorithm is applied during the dynamic mode AFM to estimate the equivalent parameters which relate to the mechanical properties of the sample. The efficacy of the developed method is shown by imaging a microtubule sample in *brb80* buffer solution. The preliminary study is able to measure the quantitative stiffness and dissipative properties of the MT sample. Further studies are planned to study how the different factors which affect the stability of the microtubules correlate to the stiffness of MTs.

Chapter 6

Topography Imaging Based on Equivalent Frequency Regulation

In this chapter, it is shown that equivalent resonant frequency of the cantilever provides higher imaging sensitivity to sample height as compared to cantilever amplitude or phase during dynamic mode operation. This sensitivity improves with reduction in quality factor of the cantilever which is in contrast to the sensitivity trends in amplitude and phase of the cantilever. Such an approach can be useful for imaging non-compliant surfaces, under fluid operations or integrated sensing-actuation applications.

6.1 Introduction

In intermittent contact mode operation, the amplitude or phase of the oscillating tip, which interacts with the sample intermittently, are used to maintain a constant tip-sample interaction amplitude and image the sample topography. One can increase the amplitude based sensitivity and decrease the forces on the sample by increasing the quality factor of the cantilever [38, 39]. There is an upper bound of unity on amplitude sensitivity [39] with respect to sample topography. This sensitivity drops below unity for non compliant surfaces and low quality factor cantilevers [40, 41]. Similar trends in imaging sensitivity with respect to the quality factor of the cantilever is seen in phase signal as well [40].

Several biological samples need to be imaged in buffers which are their native environment. Under fluid, tapping mode results in low quality factor operation [38] caused by the additional viscous damping of the surrounding fluid. Furthermore, in applications where the actuator and the sensor are integrated on same cantilever, the quality factor [42] is typically low. Reduced quality factor is due to additional viscous damping of the surrounding fluid. In all such operations, conventional tapping mode imaging suffers from reduced sensitivity.

In this chapter, the use of cantilever's equivalent resonant frequency (ω_e) to image sample topography during tapping mode operation is proposed. It is shown that ω_e sensitivity with respect to the topography increases with reducing quality factor which is an opposite trend as compared to the amplitude sensitivity. Experimental results are shown to demonstrate the predictions of the work.

6.2 Amplitude and f_e Sensitivities

Van der Waal's interaction forces are modeled in a variety of ways. The piece-wise linear model (Equation 2.10) of previous section is shown to accurately predict the bistable behavior in amplitude during tapping mode operation. Using this tip-sample interaction force model, the integrals of $\overline{\Phi}_c$ and $\overline{\Phi}_d$ from the Equations 2.8 can be evaluated analytically as

$$\overline{\Phi}_c = \begin{cases} 0 & \text{if } a < (l-d) \\ \frac{-1}{2\pi}\left[-\omega_a^2 a(\pi - S_1 - \sin(2S_1)/2) + 2\omega_a^2(l-d)\sin(S_1)\right] & \text{if } l-d \le a < l \\ \frac{-1}{2\pi}\left[-\omega_a^2 a(\pi - S_1 - \sin(2S_1)/2) + 2\omega_a^2(l-d)\sin(S_1)\right. & \\ \left.+\omega_b^2 a(\pi - S_2 - \sin(2S_2)/2) - 2\omega_b^2 l\sin(S_2)\right] & \text{if } a \ge l \end{cases}$$

$$\overline{\Phi}_d = \begin{cases} 0 & \text{if } a < (l-d) \\ \frac{-1}{2\pi} c_a a\omega(\pi - S_1 + \sin(2S_1)/2) & \text{if } l-d \le a < l \\ \frac{-1}{2\pi}\left[c_a a\omega(\pi - S_1 + \sin(2S_1)/2) + \right. & \\ \left. c_b a\omega(\pi - S_2 + \sin(2S_2)/2)\right] & \text{if } a \ge l \end{cases} \tag{6.1}$$

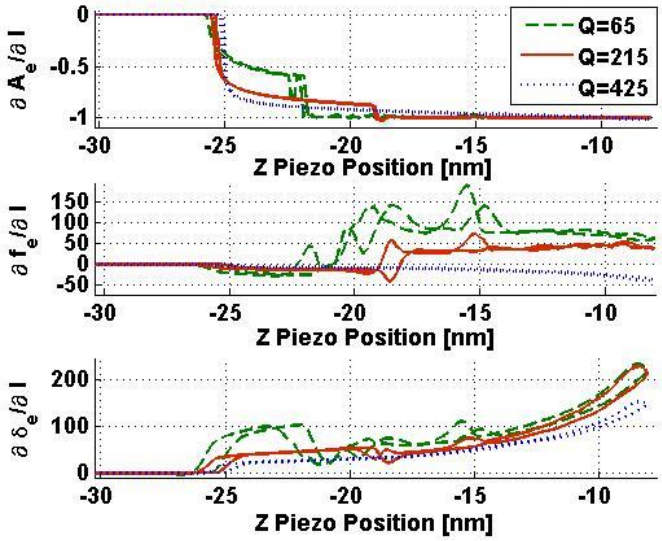

Figure 6.1: Sensitivity of steady state amplitude, equivalent resonant frequency and equivalent damping with respect to Z-Piezo position (sample height) during simulated approach-retract curves. Amplitude sensitivity is one irrespective of the cantilever's quality factor. Sensitivity of equivalent resonant frequency and damping increases with reducing quality factor.

where $S_1 = \cos^{-1}\left(\frac{-l+d}{a}\right)$ and $S_2 = \cos^{-1}\left(\frac{-l}{a}\right)$. ℓ and a can be obtained by performing an approach-retract cycle and assuming the snap-in point at $\ell = 0$. Equations 6.1 and 2.7 give analytical solutions for equivalent resonant frequency and equivalent quality factor. Thus variations of f_e and $\delta_e (= \frac{c_e}{2m})$ with ℓ is evaluated and plotted in Figure 6.1.

The equivalent cantilever model in steady state at any instance can be represented by $G(j\omega) = \frac{\omega_0^2}{\omega_e^2 + j2\delta_e\omega - \omega^2}$ (see 2.9). If the cantilever excitation is $g(t) = A_0 \cos(\omega t)$ then the cantilever amplitude in steady state is given by $a = \frac{\omega_0^2 A_0}{\sqrt{(\omega_e^2 - \omega^2)^2 + 4\delta_e^2\omega^2}}$. The sensitivity of amplitude with the tip-sample interaction is also plotted in Figure 6.1. Approach-retract curves of equivalent resonant frequency and equivalent damping sensitivity curves show increasing sensitivity with respect to sample height, with reducing quality factor of the cantilever whereas the amplitude sensitivity is always below one.

The theory developed is validated through experiments. The force curves were done on a mica sheet. The quality factor of the off-sample cantilever is varied by active Q-control circuit from 900 to 38. Amplitude and phase force curves were obtained by

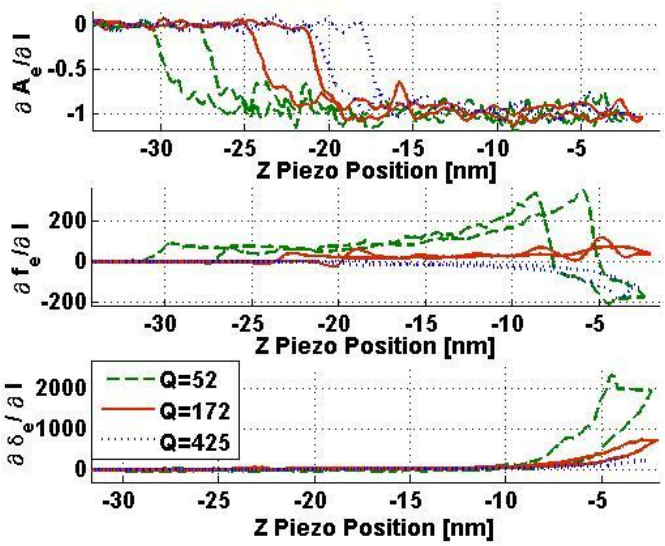

Figure 6.2: Sensitivity of steady state amplitude, equivalent resonant frequency and equivalent damping with respect to Z-Piezo position (sample height) during experimental force curves. Amplitude sensitivity is one irrespective of the cantilever's quality factor. Sensitivity of equivalent resonant frequency and damping increases with reducing quality factor similar to simulated trends.

demodulating the cantilever deflection signal. Corresponding amplitude and phase sensitivities were obtained by applying the difference method on the amplitude and phase approach-retract curve. Equivalent resonant frequency and quality factor approach-retract curves were obtained by providing the cantilever excitation and cantilever deflection to the REEP algorithm. Corresponding sensitivities were obtained by applying difference method on these estimated curves.

Experimental results for different off-sample quality factor of the cantilever are shown in Figure 6.2. As expected, the amplitude sensitivity remains constant at 1 with changes in the off-sample quality factor of the cantilever since these force curves are done on a mica sheet. It can be seen that the net change in f_e and δ_e during force curves increases with decrease in off-sample cantilever quality factor. Moreover, its sensitivity also increases with decrease in the quality factor as expected from the analytical plots.

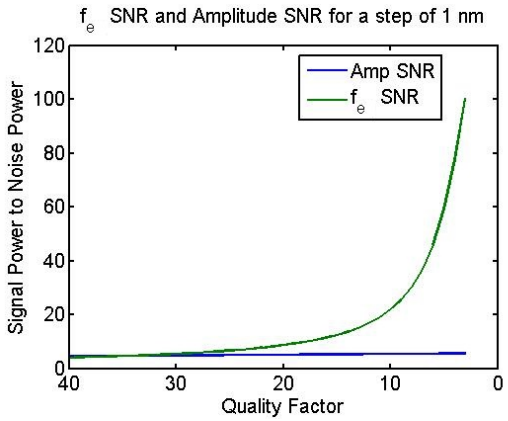

Figure 6.3: Figure shows simulations results of amplitude and equivalent resonant frequency SNR when cantilever encounters a step size of $1nm$ while free air amplitude is $50nm$

6.3 Topography Imaging

Tapping mode is the most stable mode of operation for under-fluid imaging. FM-AFM mode, though capable of true atomic resolution is not easily stabilizable for under-fluid operations. Here, FM-AFM is mostly limited to force-spectroscopy apart from recent imaging results by Sader and Jarvis. Sader-Jarvis main contribution is to map the measured frequency shift to the tip-sample force where they derived an analytical equation relating them. As shown here, the sensitivity of the equivalent resonant frequency increases with decrease in the quality factor. This is in contrast with the FM-AFM imaging where the minimum shift detectable in the resonant frequency increases as the quality factor of the cantilever decreases.

We now present simulation which use realistic noise values to evaluate SNR of the amplitude and f_e sensitivities. For these simulations noise values used are calculated from actual experimental data. Cantilever model is chosen to be with resonant Frequency 300kHz and the quality factor is varied from 30 to 3. Free air amplitude is $50nm$. REEP algorithm is used simultaneously to give estimates of equivalent resonant frequency. A step of $1nm$ is given to the sample, and signal power of amplitude and f_e is defined as the square of the difference between mean values at two levels. Noise is define as variance of steady state values when cantilever is interacting with the sample. Results are plotted in Figure 6.3.

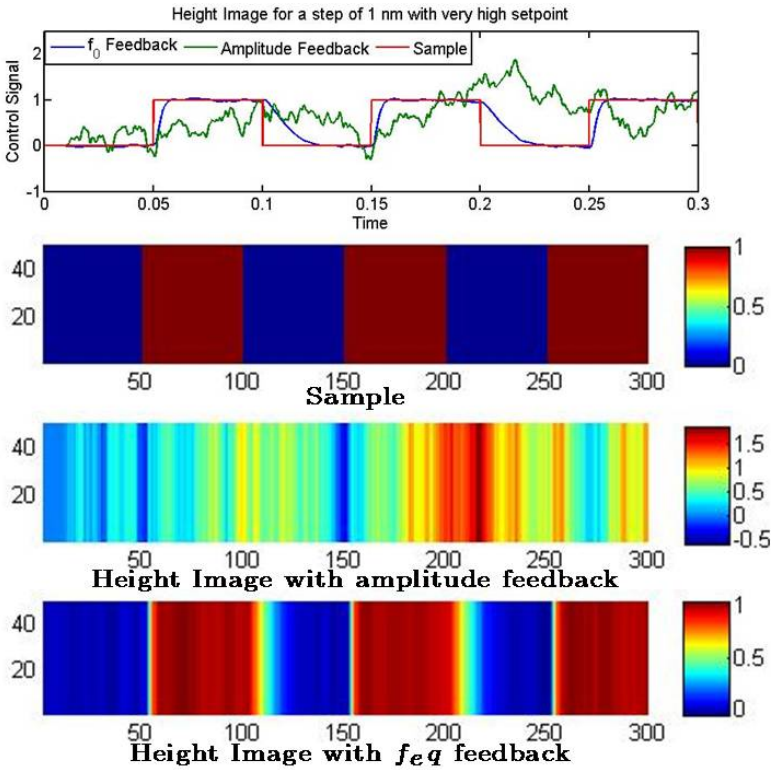

Figure 6.4: (simulation results) Shows that equivalent frequency (as estimated by the REEP algorithm) regulated based image a 1 nm variations in topography under high damping conditions is considerably better than the one obtained by regulating amplitude.

Developed REEP module that determines the equivalent parameters such as equivalent resonant frequency ω_e in real-time provides an interesting alternative to determination of topography. We propose a new dynamic mode of topography imaging where the cantilever is forced at or near the first resonant frequency together with other frequencies that facilitate estimation of the equivalent resonant frequency via the real-time REEP module. We can see in the Figure 6.3 that as Q decreases, f_e SNR increases very fast. So for low Quality factor applications, there is a potential to obtain higher resolution using the equivalent resonant frequency for regulation instead of using amplitude as the feedback signal to the z-positioning system.

Simulations are performed using a piece-wise linear model of tip-sample interaction and experiment based model of z-piezo. Model of the cantilever is same as used in plotting Figure 6.3. Here free air amplitude is kept as $200nm$ and set-point amplitude

is $199nm$. This case of very high set-point is sometimes referred as 'tickling mode' as tip-sample interaction is minimal and cantilever behaves like just tickling the sample. Here cantilever faces a step change of $1nm$.

Figure 6.4 shows the possible advantages of regulating a desired set-point frequency ω_1 where the amplitude regulation based dynamic mode method provides unacceptable results whereas the frequency regulated based imaging scheme provides a faithful estimate of the topography. Experimental verification of these results is left for future work.

Chapter 7

Directed Transport of Motor Proteins over Random Networks of Microtubules

7.1 Introduction

Intracellular transport is fundamental to cell functionality, shape and survival. A considerable fraction of the intracellular transport occurs over a network formed by microtubules that constitute the road and the rail ways of transport of cargo within the cell. The two major classes of vehicles that transport cargo over microtubules are two motor proteins; kinesins and dyneins. These motor proteins are crucial for the regulation of physiological processes such as higher brain functions, developmental patterning and suppression of tumorogenesis [43]. Malfunctions in motor function influence global aspects of cell biology including establishment of cell polarity, maintenance of genomic stability and underlie a growing list of medical maladies including cancer and neurodegenerative diseases [44, 45].

Recently, tools for investigating these systems at the molecular scale have evolved and have lead to significant insights into how these motors execute motion [46, 47, 48, 49]. For example, with optical traps [50, 51] it is possible to probe forces with resolution in the femto Newton scale which enables the study of forces exerted by single

motor proteins. Studies of detailed mechanisms at the molecular scale are carried out in-vitro, where better control of factors affecting transport is possible. In-vivo studies arrive at conclusions observing macro-scale effects of transport that are influenced by a confluence of factors [52, 53, 44, 54, 45]. In contrast to in-vitro studies, in-vivo it is difficult to control the factors. Thus, it is difficult to pinpoint causes for the observed transport behavior in-vivo. While in-vitro studies facilitate finer probing, these are currently limited to transport of a few cargo over a microtubule (MT) [48, 55]. There is thus a relative void of in-vitro studies of global-scale transport mechanisms, that could discern causes of observed global transport modalities.

This chapter identifies one important specific biological objectives related to pathways of directed transport that determine the shape of the fruit fly.

7.2 Understanding the intracellular transport over biased random networks

We now present some basic background. Microtubules (MT) are formed by polymerization of tubulin dimers and are directed linear lattices with a plus and a minus end (see Figure 7.1). The formation of a microtubule begins with the minus end and stops with the plus end. The motor protein kinesin transports cargo to the plus end whereas dynein carries the cargo to the minus end. In many scenarios, multiple motors carry the same cargo. These motors may occasionally detach and re-attach to the same or other microtubule (MT) as the cargo is carried on. It is also possible to have multiple dynein and multiple kinesin on the same cargo; the relative number that attach to a

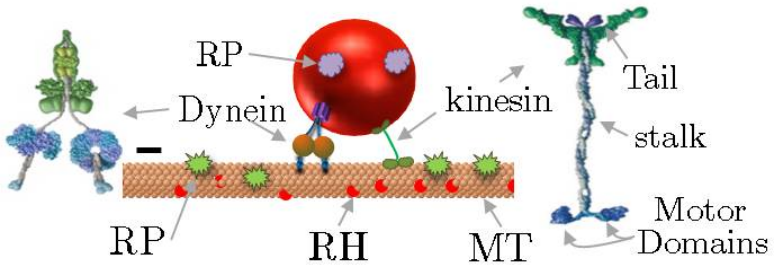

Figure 7.1: Schematic showing dynein and kinesin motor proteins attached to a cargo walking on microtubule.

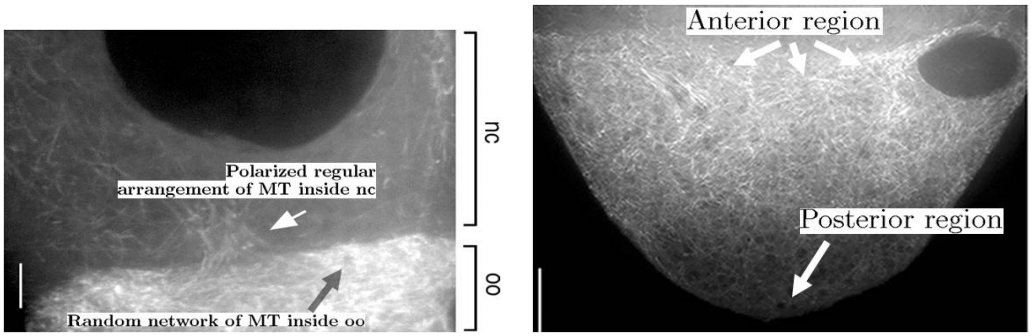

(A))B)

Figure 7.2: (A) Microtubule distribution at the ring canals leading into the oocyte. Near the ring canals (arrow), the number and organization of microtubules increases. Bar, 5 μm. (B) Microtubule distribution within the oocyte as revealed with UAS-α-tubulin-GFP. Note the meshwork appearance of the microtubule array indicating a random nature. A higher concentration of microtubules is present at the anterior cortex, compared with the posterior cortex. Bar, 10 μ m.

microtubule (MT) then determines which direction the cargo is transported [56]. The kinesin and dynein molecules both have two motor domains that form the legs for the motion on MTs. These motor domains are connected to the domain that carries the cargo (see Figure 7.1). Kinesin and dynein both convert chemical energy (provided by ATP) into mechanical motion and force production. The walking mechanism of kinesin is much better understood than dynein and a widely agreed upon model is summarized in [57]. Kinesin takes steps in a hand-over-hand motion (in contrast to the inchworm motion) and consumes one ATP molecule for every 8nm step. Each of these molecules have dimensions in the hundreds of nanometers. The cargo have dimensions in the micron range and are much larger than the motors (see Figure 7.1). Dynein too walks typically with 8 nm steps but variable step sizes are also possible.

The fruit fly, drosophila, is a good model system for obtaining insights into human pathologies [45]. The drosophila embryo has an axis that connects the front (anterior region where the head is) to the rear (the posterior region). The development of the anterior and the posterior region of the embryo begins at an early stage of the life of the fly; during the development of the oocyte. In [58], Hays et al. it was shown that bcd mRNA are transferred to oocyte from the surrounding nurse cells through nurse canals (see Figure 7.2 (A)). It was also shown in this work that the transfer of bcd

mRNA was achieved by minus ended transport by dynein on a MT network. This network of MTs in the nurse canal, was seen to be regular (see Figure 7.2(A)) with minus ends of the MTs pointing toward the transport direction (i.e into the oocyte). Once inside the oocyte, bcd mRNA almost exclusively got transported to the anterior region. It was postulated that a regular network of MTs with minus end toward the target end, the anterior region, is formed in the oocyte and dynein carry bcd mRNA on this regular network; very much like the transport inside nurse canals. However, it was conclusively shown in [54] that there is a fraction of the MTs whose minus ends are not directed at the anterior region (also see Figure 7.2 (A) and (B) that show a meshwork nature of MT inside oocyte) . Thus the observed exclusive transport of bcd mRNA to the anterior region was surprising. In [54] it was also seen that bcd mRNA recruited another factor, exuperantia from the nurse cells and without this factor bcd mRNA *does get* transported to non-anterior regions. It was postulated in [54], without any confirmation, that exuperantia equips dynein with the capability to discern which tracks lead to the anterior region. This postulate requires that the MTs that have their minus ends at the anterior region acquire special factors that differentiate them from other MTs that do not have minus ends at the anterior region.

7.3 Directed transport over a random network with bias achieved by regulation of switching tracks: an alternative hypothesis

In this section, we explore another possible means of achieving high percentage of transport toward the anterior region without invoking the capability of extra factors that differentiate MT tracks, (those which have their minus ends toward the anterior from MTs that have minus ends toward non-anterior regions). We hypothesize that exuperantia-like molecules simply increase the capability of the dynein motor to switch tracks. As the number of MT oriented toward the target end is higher, there is a greater chance of a cargo to switch from a non target oriented MT to a target ended MT than otherwise. Note that the switching is non-specific. Exuperantia-like factors simply increase the probability of switching tracks at intersections of MTs. Possibility of exclusive anterior based transport is increased (even though there are possible routes to non-anterior

regions) if phase transition types of scenario exist.

Next, we develop a mathematical model to describe such transport in a simple case of one dimension by modeling the transport as a biased random walk.

7.4 Mathematical Formulation

We study a simple model of the cargo transport in one dimension. Lets assume that once the motor starts the motion from the 'origin', it encounters intersection after traveling a distance λ. A Poisson distribution for λ with mean λ_0 is a good approximation for the physical network. Moreover let the motor has a fixed velocity v and let α be the probability of switching at each intersection. Let L' and R' be the two ends such that ($L' < 0 < R'$), and WLOG let R' is the target end. We also consider a bias in the directionality of the tracks, that is ratio of tracks going towards the target end is p($> 1/2$). In this scenario, motor travels with a constant velocity between two switching. The time taken to switch is assumed to be negligible. In future, by modeling the waiting time for each switching as a random variable, traffic jams and reversal of transport will be studied. So intersections encountered per second are v/λ, and switching rate f_{Sw}=$v\alpha/\lambda$. Also switching time T_{Sw}=$\lambda/v\alpha$. Now as v and α are constant, T_{Sw} is Poisson distributed with mean $\lambda_0/v\alpha$. Then the probability per unit time that the motor switches to right, towards the target end, is g ($=pf_{Sw}$) and the probability per unit time that the motor switches to left, towards the non-target end, is r ($=(1-p)f_{Sw}$). We further assume that the ends are absorbing, that is once the motor reaches either end it stays there. Here, we are interested in the probability of motor reaching the target end as well as the average time it takes to reach. This average time can play an important role for studying the jams.

Distance traveled between two switchings, λ_{Sw}, is vT_{Sw} which is given by λ/α. We can clearly see that the switching time T_{Sw} and the step size λ_{Sw} are not independent, in fact both of them depend on just one variable λ. The quantities of interest in this framework are the probability of motor reaching R' before it reaches L' and the conditional expected time to reach R' given it reaches R'. We approximate this framework with a random walk of a fixed step size $\beta(= \mathbb{E}(\lambda_{Sw}) = \lambda_0/\alpha)$ and the switching rates g and r where the position of motor at any time instant is same as the value of random

walk at that instant. Then the problem of finding the probability of motor reaching R' before L' (lets call it π_R) and the expected time to reach R' (lets call it τ_R) is the first-passage probability and mean first-passage time of the underlying random walk. We further simplify the problem by defining L,R as $L = L'/\beta$ and $R = R'/\beta$ and consider a random walk of unit step size. Clearly problem then translate to that of finding the first-passage probability and mean first-passage time with the boundaries L and R of a random walk with unit step size. Here by changing α, we can control the frequency of switching. Increasing α means λ_{Sw} is getting smaller (on an average) which in turn means motor is spending lesser time on each track. We are thus controlling the capability of motor to switch tracks by controlling α.

We next solve for first-passage probability and mean first-passage time of a general biased random walk with unit step size.

7.4.1 Biased Random Walk

Consider a general one step process,

$$\dot{p_n} = r_{n+1}p_{n+1} + g_{n-1}p_{n-1} - (r_n + g_n)p_n$$

where $p_n(t)$ is the conditional probability of the particle being at step n at time t given it was at some step m at time 0 with $p_n(0) = \delta_{n,m}$. The coefficient r_n is the probability per unit time that, being at n, a jump occurs to $n-1$, while g_n is the probability per unit time for a jump to $n+1$. Let L,R (such that L $<$ m $<$ R) be the left and right boundaries and we want to find the first passage time for both L and R. Let $\pi_{R,m}$ be the probability that R is reached before L, after starting from m. Whenever L+2 $\leq$ m $\leq$ R-2 the particle first has to jump to $m+1$ or to $m-1$ with probabilities $g_m/(g_m + r_m)$ and $r_m/(g_m + r_m)$ respectively. This gives the relation

$$\pi_{R,m} = \frac{g_m}{g_m + r_m}\pi_{R,m+1} + \frac{r_m}{g_m + r_m}\pi_{R,m-1}. \tag{7.1}$$

Thus we have the difference equation,

$$g_m(\pi_{R,m+1} - \pi_{R,m}) + r_m(\pi_{R,m} - \pi_{R,m-1}) = 0. \tag{7.2}$$

It can be easily seen that $\pi_{R,R}$=1 and and $\pi_{R,L}$=0. With these two boundary conditions, we solve the equation 7.2. Let $\Delta_m = \pi_{R,m+1} - \pi_{R,m}$, then equation 7.2 becomes

$$g_m\Delta_m = r_m\Delta_{m-1}.$$

This gives

$$\Delta_m = \tilde{p}_m\Delta_L$$

where

$$\tilde{p}_m = \frac{r_m r_{m-1}\ldots r_{L+1}}{g_m g_{m-1}\ldots r_{L+1}}$$

with $\tilde{p}_L$=1.

From the boundary condition $\pi_{R,L}$=0, we have $\Delta_L = \pi_{R,L+1}$. Subsequently

$$\pi_{R,m} = \sum_{\mu=L}^{m-1}\Delta_\mu = \sum_{\mu=L}^{m-1}\tilde{p}_\mu\pi_{R,L+1}.$$

From the second boundary condition $\pi_{R,R}$=1, we determine $\pi_{R,L+1}$ and finally get

$$\pi_{R,m} = \frac{\sum_{\mu=L}^{m-1}\tilde{p}_\mu}{\sum_{\mu=L}^{R-1}\tilde{p}_\mu}. \tag{7.3}$$

We now consider the *conditional* mean first-passage time $\tau_{R,m}$ for the subemsemble of points which reach R. Let at t=0, the particle is at m. Then the probability for a forward jump in the time Δt is $g_m\Delta t$; for the backward jump is $r_m\Delta t$; and remaining at m is $(1 - g_m\Delta t - r_m\Delta t)$. Thus by conservation of probability, we have:

$$\begin{aligned}(\tau_{R,m} - \Delta t)\pi_{R,m} = {} & g_m\Delta t\tau_{R,m+1}\pi_{R,m+1} + r_m\Delta t\tau_{R,m-1}\pi_{R,m-1} + \\ & (1 - g_m\Delta t - r_m\Delta t)\tau_{R,m}\pi_{R,m}.\end{aligned}$$

We define $\nu_{R,m} := \tau_{R,m}\pi_{R,m}$, which gives us a difference equation for L+1 $\leq$ m $\leq$ R-1:

$$g_m(\nu_{R,m+1} - \nu_{R,m}) + r_m(\nu_{R,m-1} - \nu_{R,m}) = -\pi_{R,m}. \tag{7.4}$$

The boundary conditions are: $\nu_{R,R}$=0 (as $\tau_{R,R}$=0) and $\nu_{R,L}$=0 (as $\pi_{R,L}$=0). Similar to the solution for $\pi_{R,m}$, we define $\Delta_m = \nu_{R,m+1} - \nu_{R,m}$ giving:

$$g_m\Delta_m - r_m\Delta_{m-1} = -\pi_{R,m}.$$

We solve this to get,

$$\Delta_m = \tilde{p}_m\Delta_L - \sum_{\mu=L+1}^{m}\frac{\tilde{p}_m}{\tilde{p}_\mu}\frac{\pi_{R,\mu}}{g_\mu}$$

where $\tilde{p}_m$ is as defined earlier.

From the boundary condition $\nu_{R,L}$=0, we have $\Delta_L = \nu_{R,L+1}$. This leads to:

$$\nu_{R,m} = \sum_{\lambda=L}^{m-1}\Delta_\lambda = \sum_{\lambda=L}^{m-1}\left(\tilde{p}_\lambda\nu_{R,L+1} - \sum_{\mu=L+1}^{\lambda}\frac{\tilde{p}_\lambda}{\tilde{p}_\mu}\frac{\pi_{R,\mu}}{g_\mu}\right).$$

By using the boundary condition $\nu_{R,R}$=0, we find $\nu_{R,L+1}$ and finally get:

$$\nu_{R,m} = \left(\sum_{x=L}^{R-1}\tilde{p}_x\right)^{-1}\sum_{\lambda=L}^{m-1}\tilde{p}_\lambda\left(\sum_{\nu=L}^{R-1}\tilde{p}_\nu\sum_{\mu=L+1}^{\nu}\frac{1}{\tilde{p}_\mu g_\mu}\pi_{R,\mu} - \sum_{\nu=L}^{R-1}\tilde{p}_\nu\sum_{\mu=L+1}^{\lambda}\frac{1}{\tilde{p}_\mu g_\mu}\pi_{R,\mu}\right). \tag{7.5}$$

Once we calculate $\nu_{R,m}$ and $\pi_{R,m}$ from equation 7.3 and equation 7.5, we can directly get $\tau_{R,m}$ (as $\tau_{R,m} = \nu_{R,m}/\pi_{R,m}$).

For the random walk approximation of our mathematical model, we have g_n and r_n constant as g and r. We can find the first-passage probability and conditional mean first-passage time of this random walk by replacing m by 0 in equations 7.3 and 7.5 respectively, i.e. $\pi_R = \pi_{R,0}$ and $\tau_R = \tau_{R,0}$. Thus we have,

$$\tilde{p}_m = \left(\frac{r}{g}\right)^{m-L}$$

$$\pi_R = \frac{\sum_{\mu=L}^{-1}\left(\frac{r}{g}\right)^{\mu-L}}{\sum_{\mu=L}^{R-1}\left(\frac{r}{g}\right)^{\mu-L}}$$

which can be simplified to,

$$\pi_R = \frac{1-(r/g)^{-L}}{1-(r/g)^{R-L}}. \tag{7.6}$$

Final expression for mean passage time (τ_R) is rather lengthy and we have omitted it here. Next we compare this analytical solution with the Monte Carlo simulations.

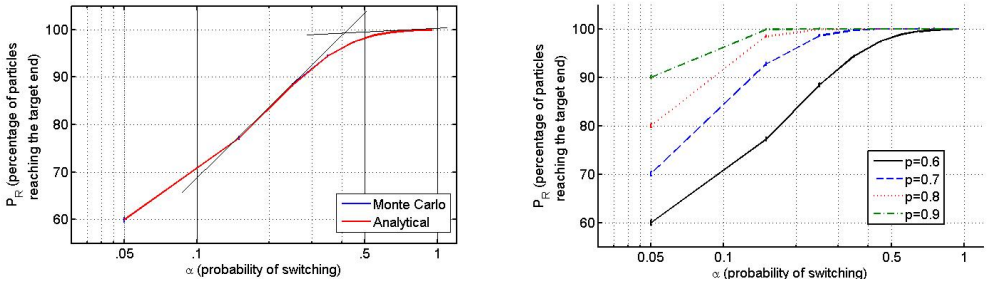

(a) (b)

Figure 7.3: (a) Statistic of motors reaching target end is plotted with the switching probability on a semilog scale for both Monte Carlo simulations and analytical expression. Standard deviation is shown as the bars in the Monte Carlo curve, both curves overlap. Here bias in the MT network is 0.6 towards the target end. Clearly phase change like behavior is visible at around $\alpha = 0.4$ with the change in slope. (b) Statistic for different values of bias is plotted. Higher bias leads to directed transport even for low values of α.

7.4.2 Simulation and Results

To simulate this model, a continuous time random walk is simulated. A motor's position is initialized at origin. As discussed earlier, switching time T_{Sw} is taken to be Poisson distributed with with mean $\lambda_0/v\alpha$ where the motor travels with constant velocity v between switchings. Probability of switching to a target ended track is p, where p is varied from 0.6 to 0.9. Also α is varied to incorporate the effect of Exu, by changing the ability of motor to switch tracks more or less often. The absorbing boundaries of the walk are given by L' and R' for non-target and target end respectively. The Monte Carlo simulation is run 100 times with 100 thousand motors each time for all values of p and α. Mean and standard deviation is calculated for the number of particles reaching the target end.

The results are compared with the analytical expression (Equation 7.6) and plotted in the Figure 7.3. We can see from the Figure 7.3 (a) that probability of reaching the target end (π_R) calculated using both Monte Carlo simulation and analytical expression match extremely well with curves overlapping. Also it is clear as the switching probability increases, almost absolute directed transport is achieved. Tangents on two different part of the curve are sketched to highlight the change in slope. A phase transition in

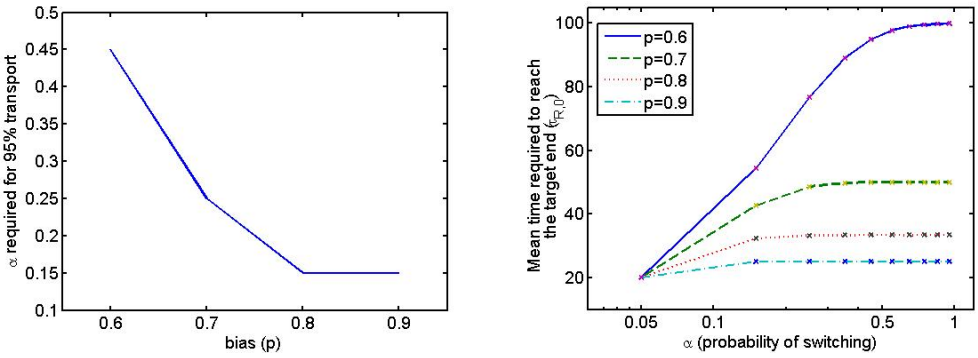

(a) (b)

Figure 7.4: (a) Probability of switching (α) required to achieve at least 95% transport is plotted with the bias in the MT network. As bias increases, α required decreases drastically. (b) Average time required to reach the target end is plotted with the probability of switching for different values of the bias (p). Curves are from Monte Carlo simulation and the x marks are from the analytical expression. Clearly as α increases, mean time increases thus a trade-off exist between fast transport and directed transport.

the probability of reaching the target is observed as we increase the α, as the slope of the curve on the semilog plot is changed. π_R vs α for different values of bias p is plotted in Figure 7.3 (b). As bias is increased, motor exclusively reaches the target end with very low switching probability. We also plot α required for achieving more than 95% transport with the bias p in Figure 7.4 (a). For systems with small bias, frequency of switching required for directed transport is very high. This necessitates the presence of Exu like compounds for directed transport. Figure 7.4 (b) plots the average time required to reach the target end (τ_R) with the probability of switching for different values of the bias (p). Again, the time calculated from the Monte Carlo simulation matches extremely well with that calculated from the analytical expression obtained in the previous section. Here, it is clear that as the probability of switching increases, average time also increases which may lead to jams. Thus even though switching ability is leading to directed transport, it is slowing the transport leading to a trade-off between faster transport and directed transport. This trade-off needs to be further explored when doing modeling for jams. These simulations strengthen the hypothesis that the random network of MTs itself is responsible for polarized transport where Exu is only increasing the affinity of motor proteins to switch tracks. Parameters chosen for the

simulation are: $\lambda_0 = 1$, $L' = -20$, $R' = 20$ and $v = 1$.

7.5 Transport in two dimension

Even though one dimensional simulation gives important insights into intracellular transport, it is desirable to obtain and simulate a two dimension model which is more closer to the actual scenario. In two dimension, complexity of the model increases considerably as a 2D biased random walk model is not directly applicable. To visualize this scenario, we can think of microtubules (MTs) as lines or curves on a Cartesian plane where the target and non-target ends can be just $x = R$ and $x = -L$ lines. Then a motor can walk on a MT and will switch with some probability while facing an intersection. The motor will keep walking in this fashion till it reaches one of the ends or detaches from the MT (not considered here). Then according to the hypothesis, if motor faces enough intersection and has high rate of switching, we will see directed transport. We next present a simulation model for this scenario.

7.5.1 Simulation Model

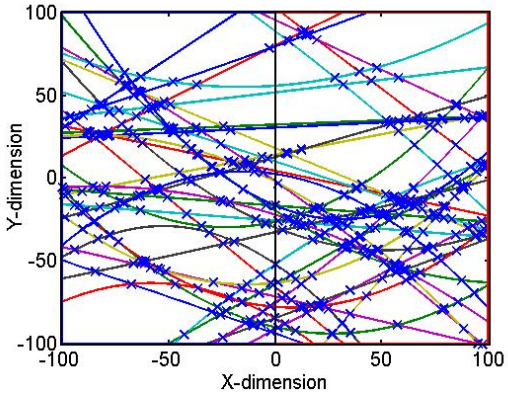

Figure 7.5: One instance of network with 40 microtubules, 20 linear and 20 quadratic with $L = R = 100$. Here the blue and red thick outline on the left and right half plane donates the boundaries of the non-target and target end respectively. Intersections are marked with $\times$.

As mentioned earlier, for creating the MT network, we will assume MTs to be just

lines or quadratic curves on a Cartesian plane. We set boundaries of the plane of interest (POI) at $x = R$, $x = -L$, $y = -L$ and $y = R$. We further assume the target end to be the perimeter of the right half of the plane and non-target end to be the perimeter of the left half (as shown in Figure 7.5). For creating a network of N MTs, we randomly chose $N/2$ linear and $N/2$ quadratic curves, such that they are inside the POI. We then randomly assign an orientation of $+1$ or -1 to the MTs with a specified bias. In this framework, orientation of MT is define as $+1$ if a motor attached to the MT moves toward the right half plane and -1 if the motor moves toward the left half plane. That is there is a local bias towards one end of the POI. Once the MTS are chosen, all the intersections are found and stored. Figure 7.5 shows one such instance of random network created with total 40 MTs.

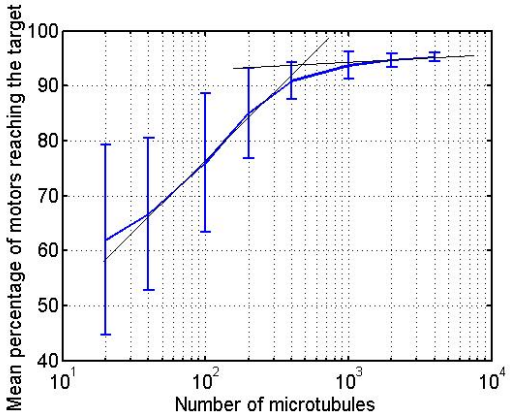

Figure 7.6: Results of Monte Carlo simulation for two-dimensional transport over microtubules are plotted here. Number of MTs is on the x-axis, and mean percentage of the motors reaching the target end is on the y-axis. Bars are standard deviation across different instance of network for same no. of MTs. Its a semilog plot and the change of slope clearly shows phase-change kind of behavior (at around 500 MTs). Also as the no. of MTs in increasing, standard deviation is decreasing drastically.

For finding the statistics of the transport, Monte Carlo simulations are run on the created MT network. Here, we can see as we increase the no. of MTs, density of the network increases and so the number of intersections per unit time faced by a motor also increases. If the probability of switching over an intersection is constant, probability of switching per unit time also increases. That means, N parameter will play a similar role as α played in the case of 1D simulation. While doing Monte Carlo, N was varied from

20 to 4000 and for each N, 30 different instances of network were created with 60% bias towards the target end. For each instance of network, motor was started randomly from the line $x = 0$ and statistics of motor reaching the target end was obtained. Enough runs were simulated so that the standard deviation was less than 1%. It was observed that for low values of N, the mean no. of motors reaching the target varied significantly across different instances of the network for the same N, but the mean over different instance was more than 60% (see Figure 7.6). As N was increased the transport was highly directed (mean more than 95%) with variance across different instance of network for same N significantly reduced. Results of one simulation run, where the probability of switching over an intersection was 0.5, are plotted in Figure 7.6. Here also, as seen in the case of one-dimension, a phase change behavior is clearly visible from the semilog plot thus further strengthening our hypothesis.

Chapter 8

Summary and Discussion

Here, we have provide a methodology and paradigm to aid emerging research studying and manipulating different mechanical properties of material. There is a scarcity of real-time techniques to quantify the stiffness and dissipation properties of soft-matter. Here we have first reported a method (REEP algorithm) which is able to provide estimates of sample stiffness and dissipation during intermittent contact mode operation of AFM, most suitable for imaging soft samples. The method is verified using the averaging theory and shown to accurately provide the dissipation estimates when applied on different polymer samples. A FPGA based hardware implementing the algorithm is developed to make use of the real-time capability of the algorithm. The REEP module is then used to study stiffness and dissipation properties of PBMA-PLMA polymer blend.

Number of biological samples need to be imaged in there native conditions. In liquid, acoustic excitation of cantilever suffers from 'forest of peak' phenomenon where cantilever resonance is shadowed by liquid layer response. A magnetic excitation hardware is developed to accurately resonate the cantilever in liquid achieving a clean ac response of the cantilever. A microtubule sample is imaged in a buffer solution to show the applicability of REEP module in liquid. Results verify that the module is able to accurately characterize the stiffness and dissipation properties of the sample. Under liquid operation, as the quality factor of the cantilever is significantly reduced, higher eigenmodes of the cantilever also come into play. For that part, we have used averaging theory to develop the equivalent cantilever model for a multimode model of the cantilever. Simulation results for a two-mode model are promising. We have also

reported a tool to detect resonance condition in which this equivalent model becomes invalid. The contribution of different eigenmodes in forming the cantilever deflection is studied next. A receding horizon Kalman filter is reported which is able to estimate the contribution of different modes of the cantilever, an order of magnitude faster than the current amplitude demodulation based methods. An impulse-response based detection architecture is also developed for the case when only the presence of the higher modes need to be detected.

It was shown in Chapter 6 that f_e feedback gives better sensitivity. A new form of imaging was developed and explored using REEP based f_e estimates as a feedback to z-positioning system. It was shown that for low Q operation, this method has much higher resolution compared to amplitude based feedback. In future, relevant hardware will be developed to implement this. This will push the resolution of current AFM techniques even further without the need of ultra high vacuums.

A new hypothesis for explaining directed intracellular transport was reported in Chapter 7. It was shown by the help of simulation and analytical model that the directed intracellular transport on microtubules can be achieved by motors having the ability to switch on intersections. Simulations were done for both one and two dimensions.

References

[1] JP Cleveland, B. Anczykowski, AE Schmid, and VB Elings. Energy dissipation in tapping-mode atomic force microscopy. *Applied Physics Letters*, 72:2613, 1998.

[2] G. Binnig, C. F. Quate, and C. Gerber. Atomic force microscope. *Phys. Rev. Lett.*, 56:930, 1986.

[3] Y Martin, CC Williams, and H Kumar Wickramasinghe. Atomic force microscope–force mapping and profiling on a sub 100-å scale. *Journal of Applied Physics*, 61(10):4723–4729, 1987.

[4] M. V. Salapaka, H. S. Bergh, J. Lai, A. Majumdar, and E. McFarland. Multi-mode noise analysis of cantilevers for scanning probe microscopy. *Journal of Applied Physics*, vol. 81(6):2480–2487, March 1997.

[5] SP Jarvis, T Ishida, T Uchihashi, Y Nakayama, and H Tokumoto. Frequency modulation detection atomic force microscopy in the liquid environment. *Applied Physics A*, 72(1):S129–S132, 2001.

[6] Greg Haugstad. *Atomic Force Microscopy: Understanding Basic Modes and Advanced Applications*. Wiley, 2012.

[7] N.F. Martínez and R. García. Measuring phase shifts and energy dissipation with amplitude modulation atomic force microscopy. *Nanotechnology*, 17(7):S167, 2006.

[8] J. Melcher, C. Carrasco, X. Xu, J.L. Carrascosa, J. Gómez-Herrero, P. José de Pablo, and A. Raman. Origins of phase contrast in the atomic force microscope in liquids. *Proceedings of the National Academy of Sciences*, 106(33):13655, 2009.

[9] NF Martinez, S. Patil, J.R. Lozano, and R. Garcia. Enhanced compositional sensitivity in atomic force microscopy by the excitation of the first two flexural modes. *Applied physics letters*, 89(15):153115–153115, 2006.

[10] P. Agarwal and M.V. Salapaka. Real time estimation of equivalent cantilever parameters in tapping mode atomic force microscopy. *Applied Physics Letters*, 95(8):083113, 2009.

[11] Ricardo Garcia and Elena T Herruzo. The emergence of multifrequency force microscopy. *Nature nanotechnology*, 7(4):217–226, 2012.

[12] Xin Xu, John Melcher, Sudipta Basak, Ron Reifenberger, and Arvind Raman. Compositional contrast of biological materials in liquids using the momentary excitation of higher eigenmodes in dynamic atomic force microscopy. *Phys. Rev. Lett.*, 102:060801, Feb 2009.

[13] S. Jesse, S. V. Kalinin, R. Proksch, A. P. Baddorf, and B. J. Rodriguez. The band excitation method in scanning probe microscopy for rapid mapping of energy dissipation on the nanoscale. *IOP-Nanotechnology*, vol. 18:435503, July 2007.

[14] A. Gannepalli, DG Yablon, AH Tsou, and R. Proksch. Mapping nanoscale elasticity and dissipation using dual frequency contact resonance afm. *Nanotechnology*, 22:355705, 2011.

[15] MP Nikiforov, S. Jesse, AN Morozovska, EA Eliseev, LT Germinario, and SV Kalinin. Probing the temperature dependence of the mechanical properties of polymers at the nanoscale with band excitation thermal scanning probe microscopy. *Nanotechnology*, 20:395709, 2009.

[16] N Balke, S Jesse, AN Morozovska, E Eliseev, DW Chung, Y Kim, L Adamczyk, RE Garcia, N Dudney, and SV Kalinin. Nanoscale mapping of ion diffusion in a lithium-ion battery cathode. *Nature nanotechnology*, 5(10):749–754, 2010.

[17] S.V. Kalinin, B.J. Rodriguez, S. Jesse, P. Maksymovych, K. Seal, M. Nikiforov, A.P. Baddorf, A.L. Kholkin, and R. Proksch. Local bias-induced phase transitions. *Materials Today*, 11(11):16–27, 2008.

[18] Anil Gannepalli, Abu Sebastian, Jason Cleveland, and Murti Salapaka. Thermally driven non-contact atomic force microscopy. *Applied Physics Letters*, 87(11):111901, 2005.

[19] Abu Sebastian and Srinivasa Salapaka. Design methodologies for robust nanopositioning. *IEEE Transactions on Control Systems Technology*, 13(6):868–876, 2005.

[20] Srinivasa Salapaka, Tathagata De, and Abu Sebastian. Sample-profile estimate for fast atomic force microscopy. *Applied Physics Letters*, 87(5):053112–053112, 2005.

[21] A. Sebastian, A. Gannepalli, and M.V. Salapaka. A review of the systems approach to the analysis of dynamic-mode atomic force microscopy. *Control Systems Technology, IEEE Transactions on*, 15(5):952–959, 2007.

[22] A. S. Paulo and R. Garcia. Unifying theory of tapping-mode atomic-force microscopy. *Physical Review B*, vol. 66:041406(R), 2002.

[23] A. Sebastian, M. V. Salapaka, D. J. Chen, and J. P. Cleveland. Harmonic analysis based modeling of tapping-mode afm. *Proceedings of the American Control Conference*, pages 232–236, June 1999.

[24] J.A. Sanders, F. Verhulst, and J.A. Murdock. *Averaging methods in nonlinear dynamical systems*. Springer Verlag, 2007.

[25] A. Sebastian, M. V. Salapaka, D. Chen, and J. P. Cleveland. Harmonic and power balance tools for tapping-mode atomic force microscope. *Journal of Applied Physics*, 89 (11):6473–6480, June 2001.

[26] N. N. Bogoliubov and Y. A. Mitropolskii. *Asymptotic methods in the theory of non-linear oscillations*. Hindustan publishing corporation, New Delhi, India, 1961.

[27] Robert W. Stark. Dynamics of repulsive dual-frequency atomic force microscopy. *Applied Physics Letters*, 94(6):063109 –063109–3, feb 2009.

[28] Jose R. Lozano and Ricardo Garcia. Theory of multifrequency atomic force microscopy. *Phys. Rev. Lett.*, 100:076102, Feb 2008.

[29] R. García. *Amplitude Modulation Atomic Force Microscopy.* Wiley-VCH, 2010.

[30] G. Haugstad and K. Wormuth. Digital pulsed force mode afm and confocal raman microscopy in drug-eluting coatings research. In *MRS Proceedings*. Cambridge Univ Press, 2011.

[31] BDO Anderson and JB Moore. *Optimal Filtering.* Prentice-Hall, Englewood Cliffs, NJ, 1979.

[32] W.H. Kwon, P.S. Kim, and P.G. Park. A receding horizon kalman fir filter for linear continuous-time systems. *Automatic Control, IEEE Transactions on*, 44(11):2115–2120, 1999.

[33] D. R. Sahoo, A. Sebastian, and M. V. Salapaka. Transient-signal-based sample-detection in atomic force microscopy. *App. Phys. Lett.*, 83(26):5521, December 2003.

[34] D. Sahoo and M. V. Salapaka. Observer based imaging metods for atomic force microscopy. *Decision and Control, 44th IEEE Conference on*, pages 1185–1190, 2005.

[35] Alan Willsky and H Jones. A generalized likelihood ratio approach to the detection and estimation of jumps in linear systems. *Automatic Control, IEEE Transactions on*, 21(1):108–112, 1976.

[36] T. Kailath, A. H. Sayed, and B. Hassibi. *Linear Estimation.* Prentice Hall New Jersey, 2000.

[37] Brian Mickey and Jonathon Howard. Rigidity of microtubules is increased by stabilizing agents. *The Journal of cell biology*, 130(4):909–917, 1995.

[38] H. Holscher and U. D. Schwarz. Q-controlled amplitude modulation atomic force microscopy in liquids: An analysis. *Applied Physics Letters*, vol. 89:073117, 2006.

[39] L. Nony, R. Boisgard, and J. P. Aime. Nonlinear dynamical properties of an oscillating tip-cantilever system in the tapping mode. *Journal of Chemical Physics*, vol. 11, No. 4:1615–1627, July 1999.

[40] J. Kokavecz, Z. L. Horvath, and A. Mechler. Dynamical properties of the q-controlled atomic force microscope. *Applied Physics Letters*, vol. 85, No. 15:3232–3234, 2004.

[41] F. Dubourg, J. P. Aime, G. Couturier, and J. Salardenne. Apparent hardening of soft samples through q factor change in afm. *Europhysics Letters*, vol. 65, No. 5:671–676, 2003.

[42] P., D.R.Sahoo, A. Sebastian, H. Pozidis, and M.Salapaka. Modeling and identification of the dynamics of electrostatically actuated microcantilever with integrated thermal sensor. *Proceedings of the Conference on Decision and Control*, Dec 2008.

[43] N. Hirokawa, Y. Noda, Y. Tanaka, and S. Niwa. Kinesin superfamily motor proteins and intracellular transport. *Nature Reviews Molecular Cell Biology*, 10(10):682–696, 2009.

[44] Y. Ikeda, K.A. Dick, M.R. Weatherspoon, D. Gincel, K.R. Armbrust, J.C. Dalton, G. Stevanin, A. Dürr, C. Zühlke, K. Bürk, et al. Spectrin mutations cause spinocerebellar ataxia type 5. *Nature genetics*, 38(2):184–190, 2006.

[45] D.N. Lorenzo, M. Li, S.E. Mische, K.R. Armbrust, L.P.W. Ranum, and T.S. Hays. Spectrin mutations that cause spinocerebellar ataxia type 5 impair axonal transport and induce neurodegeneration in Drosophila. *The Journal of cell biology*, 189(1):143, 2010.

[46] Steven M. Block, Lawrence S. B. Goldstein, and Bruce J. Schnapp. Bead movement by single kinesin molecules studied with optical tweezers. *Nature*, 348:348–352, 1990.

[47] S M Block. Nanometres and piconewtons: the macromolecular mechanics of kinesin. *Trends in Cell Biology*, 5(4):169–175, 1995.

[48] M. Vershinin, B.C. Carter, D.S. Razafsky, S.J. King, and S.P. Gross. Multiple-motor based transport and its regulation by Tau. *Proceedings of the National Academy of Sciences*, 104(1):87, 2007.

[49] M. Vershinin, J. Xu, D.S. Razafsky, S.J. King, and S.P. Gross. Tuning microtubule-based transport through filamentous MAPs: the problem of dynein. *Traffic*, 9(6):882–892, 2008.

[50] A. Ashkin. Acceleration and trapping of particles by radiation pressure. *Phys. Rev. Lett.*, 24(4):156–159, Jan 1970.

[51] A. Ashkin. Forces of a single-beam gradient laser trap on a dielectric sphere in the ray optics regime. *Biophys. J.*, 61(2):569–582, 1992.

[52] V. Muresan, M.C. Stankewich, W. Steffen, J.S. Morrow, E.L.F. Holzbaur, and B.J. Schnapp. Dynactin-Dependent, Dynein-Driven Vesicle Transport in the Absence of Membrane Proteins:: A Role for Spectrin and Acidic Phospholipids. *Molecular Cell*, 7(1):173–183, 2001.

[53] N. MacDougall, A. Clark, E. MacDougall, and I. Davis. Drosophila gurken (TGF [alpha]) mRNA Localizes as Particles that Move within the Oocyte in Two Dynein-Dependent Steps. *Developmental cell*, 4(3):307–319, 2003.

[54] B.J. Cha, B.S. Koppetsch, and W.E. Theurkauf. In vivo analysis of Drosophila bicoid mRNA localization reveals a novel microtubule-dependent axis specification pathway. *Cell*, 106(1):35–46, 2001.

[55] Melanie JI Müller, Stefan Klumpp, and Reinhard Lipowsky. Tug-of-war as a cooperative mechanism for bidirectional cargo transport by molecular motors. *Proceedings of the National Academy of Sciences*, 105(12):4609–4614, 2008.

[56] S.E. Encalada, L. Szpankowski, C. Xia, and L.S.B. Goldstein. Stable Kinesin and Dynein Assemblies Drive the Axonal Transport of Mammalian Prion Protein Vesicles. *Cell*, 144(4):551–565, 2011.

[57] Steven M. Block. Kinesin motor mechanics: Binding, stepping, tracking, gating, and limping. *Biophysical Journal*, 92(9):2986 – 2995, 2007.

[58] S. Mische, M. Li, M. Serr, and T.S. Hays. Direct observation of regulated ribonucleoprotein transport across the nurse cell/oocyte boundary. *Molecular biology of the cell*, 18(6):2254, 2007.